Development of Planar Langmuir Probes For Supersonic Plasma Flow

A thesis for the degree of

PHILOSOPHIAE DOCTOR

Presented to

DUBLIN CITY UNIVERSITY

By

Peter Edward Sheerin B.Sc.
School of Physical Sciences
Dublin City University

Research Supervisor:
Prof. M. M. Turner

External Examiner: Dr L. Pitchford

Internal Examiner: Dr. E. McGlynn

January 2009

Declaration

I hereby certify that this material, which I now submit for assessment on the programme of study leading to the award of Philosophiae Doctor is entirely my own work, that I have exercised reasonable care to ensure that the work is original, and does not to the best of my knowledge breach any law of copyright, and has not been taken from the work of others save and to the extent that such work has been cited and acknowledged within the text of my work.

Signed: .....

Peter Edward Sheerin

ID No.: 95677615

Date: 23^{rd} January 2009

Acknowledgements

Firstly I would like to thank my supervisor, Miles Turner, for giving me the opportunity to carry out this research and trusting me to crew on Rogue Toad. Your advice and support over the course of this work has always been a welcome addition and greatly appreciated. I wish the very best to you and Samantha for the future.

I would also like to acknowledge and thank all the academics who have generously shared their time, knowledge and expertise with me in particular Dr. Brendan Doggett, Prof. James Lunney, Dr. Paddy McCarthy for their contribution of experimental results and Dr. Derek Monahan, Dr Paul Boyle, Dr Bernard Keville, Dr Bert Ellingboe and Dr. Adam Kelly for their comments and feed back.

Thanks also to the friends who have made sure the last few years were never dull. Artwolf, Angus, Derek, Dshagins, Dot, Elin, Fiachra, Chanel, Chelliechel, Claire, Grimnar, Iomhar, Mark, Natsuki, Seibh, Shane, Siren, Stuart, Tom, Twiggy, Xaiver Gonne, Yuezhong, the list goes on and on so I hope you will forgive me for not thanking you all by name.

Lastly but most importantly I'd like to thank my family. Pat and Gráinne you have been the best siblings I could have ever asked for. Finally thank you Mum your boundless support and encouragement has made all this possible.

This research was funded by a grant from the Irish Research Council for Science, Engineering and Technology (IRCSET).

ABSTRACT

Langmuir probes are a long established tool for the investigation and characterization of plasmas. Diagnostic use of planar Langmuir probes in stationary low temperature plasmas is a well understood and long established technique. When the plasma possesses a drift velocity greater than the ion sound speed the flow is considered to be supersonic. Under such conditions the theory for Langmuir probes is less than satisfactory. Where the flow is supersonic the Mach probe theory of Hudis and Lidsky [1] can be applied for a magnetized plasma. However in the case of an unmagnetized plasma there is no satisfactory theory. It has been observed that in orientating a planar Langmuir probe parallel to the direction of flow, the ion current due to the flow is eliminated. Under such conditions the behaviour of the plasma's interaction with the probe bears close resemblance to the conditions seen in plasma immersion ion implantation (PIII).

This thesis describes the adaptation's made to PIII analytical model's to take advantage of these similarities and its use to then describe the ion current of planar Langmuir probes in unmagnetized plasmas possessing a supersonic flow. In adapting a suitable analytical model for planar Langmuir probes under such conditions, extensive use of both 1D and 2D hybrid particle in cell (PIC) simulations have been made. Additionally the work required the development of a 2D hybrid PIC code where the probe is embedded within the grid. This allowed the investigation of the impact of edge effects on the analytical model's performance. The theory for and structure of the 2D code is also presented as part of this work.

Three different probe orientations are considered, firstly the parallel case, the other two concerns the near parallel cases of the probe surface orientated both into and away from the direction of flow. The model's performance

under these conditions is evaluated and discussed. Finally the use of this model in allowing a planar Langmuir probe to act as a Mach probe is also considered.

In testing the success of the analytical model against experimental data, comparisons are made between the models results and those of the 2D hybrid PIC. The experimental results used for this work were for xenon plasma with a range of moderately supersonic velocities and a highly supersonic silver laser ablated plasma plume.

Contents

List of Figures

LIST OF FIGURES

LIST OF FIGURES

CHAPTER 1

Introduction

1.1 Basic Plasma Theory

Since the study of plasma began in the 19^{th} century with simple electrical discharges, there has been no clean cut definition of what precisely constitutes the threshold between a weakly ionized gas and plasma. This is no doubt in part due to the range of several orders of magnitude of temperature and density over which plasmas form. The general definition of a plasma is a quasi-neutral ionized gas consisting of roughly equal numbers of positive and negative charges' exhibiting collective behaviour [2, 3].

The quasi-neutrality results from the balance of positive and negative charges constant motion as they move together to screen out any applied or self generated electric fields. The distance over which these fields fall off is

one of the key plasma parameters defined as the Debye length λ_D

$$\lambda_D = \sqrt{\frac{\epsilon_0 T_e}{e n_0}}, \tag{1.1}$$

where ϵ_0 is the vacuum permittivity, T_e the electron temperature in electron volts (eV), e is the absolute electron charge and n_0 the undisturbed plasma density.

For the screening to be effective the dimensions of the plasma L need to much greater than $\lambda_D \leq L$ and there must be a large enough number of particles for its assumptions (e.g. electrons in thermal equilibrum)to be statistically valid [2, 4]. Any disturbance in the quasi-neutrality of the plasma will cause an electric field which the electrons will move to screen out. In moving into position they tend to over shoot the mark and oscillate around the new zero field position as they slow down. This oscillation occurs at a frequency defined as the plasma frequency ω_{pe}

$$\omega_{p(i,e)} = \sqrt{\frac{n_{i,e} e^2}{\epsilon_0 m_{e,i}}}, \tag{1.2}$$

where m is the particle mass and i and e indicate the ions' and electrons' properties, respectively. For the electrons to behave in this manner requires that they are free to move within the plasma. As such the average number of collisions with neutral atoms or molecules per second ϑ_m (electron neutral collision frequency) must be less than the plasma frequency ω_p. Otherwise these oscillations are damped to the point where the plasma behaves as though it were an ordinary ionized gas with the motion dominated by local effects.

The heating required to get the material into this highly ionized state can be achieved through a variety of different methods. Typical methods for the generation of plasma start with the material to be ionized contained within

an evacuated chamber. It is then heated though an appropriate method depending on its planned application. In the case of gas two main method is electric discharge common examples being the DC discharge and the RF discharge. In the DC case a large bias is applied between an anode and cathode. With a large enough current the gas breaks down to form either an Arc or Glow discharge. For RF discharges there are several different methods used. In inductive RF discharges a high frequency AC current is driven in a coil surrounding the plasma chamber. The surface currents induced in the plasma act to heat and maintain it, while in the capacitive RF discharge the AC voltage is applied across an anode and cathode. The electrons oscillate at the applied frequency ionizing the stock gas and heating the plasma though collisions. In the case of a solid material other methods must be used such as laser ablation (see section 1.1.1).

The result of the heating method used is a cloud of ions, electrons and un-ionized material. The percentage of ionization will depend on the material and the amount of energy used. The boundary between a hot gas state and the plasma state is not clear cut. There is no set percentage of ionization, temperature or pressure at which this is deemed to occur. Instead a material is held to be in a plasma state when it exhibits the two key characteristics of electrical conductivity and collective behaviour to applied electric and magnetic fields.

In most heating methods electrons are the principle means of coupling energy into the plasma. Therefore electrons tend to be hotter than the ions and travelling at greater speeds. Even when the different particle species are in thermal equilibrium the electrons will still be travelling at a greater velocity due to their lower mass [5]. The very large difference in mass also explains why the ions and electrons do not thermalise, as the impulse imparted by

any collisions transfers little kinetic energy between the two. Where the plasma is in contact with a surface the higher electron flux very quickly leads to a positive charge imbalance. This region of positive charge which acts to contain the electrons is termed a sheath. Sheaths naturally form wherever the plasma is in contact with a surface. The above example would arise when a plasma is in contact with a grounded wall. The imbalance in flux will also trigger the formation of a sheath around a floating object as charge accumulates on the surface. In applications such as Langmuir probe diagnostics or pulsed ion implantation the surfaces often have large negative biases applied to them.

When a large negative bias is applied to the surface the electrons in the vicinity of the surface are expelled rapidly due to their low mass leaving a large density of ions behind. Such sheaths are referred to as *matrix sheaths*[1]. The width of this sheath s_0 [4]. Assuming the applied bias is constant then as the matrix sheath relaxes the ions are accelerated across the sheath on to the surface. This loss of positive charge to the surface will cause the sheath to expand outwards into the plasma to compensate. In time the sheath expands to the point where a flux balance is achieved and it enters a steady state. This state is referred to as a Child-Law Sheath[4].

In order to describe the behaviour of plasma perfectly the tracking of the position and velocity of every constituent particle at every time along with the electric and magnetic fields acting on them would be required. Considering that the typical processing plasma of industrial interest has densities of $10^{18}m^{-3}$ [3] it is probably an understatement to say such an approach is impractical.

[1] An ion rich sheath created by the apparently instantaneous expulsion of electrons on the time scale of the ion motion,($\omega_{pe} >> \omega_{pi}$). [4]

Instead by taking advantage of the similarity between the behaviour of plasma and that of a gas a similar statistical treatment is often used. Temperatures are described by thermal distributions. Collisions and chemical reaction rates are described by probabilities. Velocity distributions are averaged to describe the overall motion of the plasma, etc. These broad generalisations allow the reduction of the complex systems at play within the plasma to the point where they can be modelled, while hopefully preserving enough of the real physical nature of the system that intelligent and meaningful data can be extracted from experimental results.

1.1.1 Laser Ablated Plasma

Plasmas are not static, the component particles are in constant motion. Such motion is mainly thermal in nature and is not normally biased in any particular direction. Several types of generation lead to the introduction of a directed flow or beam to the plasma. Such flows are considered supersonic when they exceed the ion sound speed. These include flames, DC arcs and laser ablated plumes. It is the latter with its supersonic flow that is of particular interest to this work.

The experimental setup for the formation of the plasma through the ablation of a solid metal target by a laser pulse is extensively detailed in the literature [6–18]. The basic elements common to all setups involve a laser pulse being focused onto the target to be ablated. The target is typically housed within a vacuum chamber along with the diagnostic apparatus to be used. Many different refinements are implemented such as rotating the target to ensure repeatability[2] or filling the chamber with a background gas depending on the requirements of the work being done. The choice of inci-

[2]As the target is rotating each laser shot should strike a fresh section of its surface.

dence angle for the laser striking the surface is not critical to the formation of a plasma. At angles other than normal incidence there are additional effects to be considered for example the effect of the beam spot on the geometry of the expanding plume [13–15]. The lasers used typically have a pulse length in the range of some tens of ns with values of 6-50ns being common and wavelengths in the UV range (150-400nm) [7, 10, 11]. Plasma temperatures up to 1KeV are achievable depending on intensity and duration of the pulse.

The beam spot is focused though various means onto the target so that the intensity of the pulse will cause the maximum ionization of the target. When the laser pulse strikes the target, heating first occurs through mechanisms such as absorption by electrons in the conduction band and thermal conduction through collisions between excited electrons. This leads to the ablation of the target through evaporation and the ionization of the material ablated. Additional heating of this vapor through processes such as Inverse Bremsstrahlung [3] [10, 16, 19] and photo ionization excite the evaporated material into a highly ionized state. As the laser pulse continues to ablate the surface of the material increasing the plasma density, there is a corresponding increase in opacity of the plasma. This in turn leads to more of the energy of the pulse being absorbed into the evaporated material causing a further heating of the ablated material.

The pressure exerted by the plasma expansion over such a short time scale has also been noted to cause a compression shockwave to propagate into the target and given sufficient irradiance can in itself lead to further ionization of the target material [19]. Towards the end of the pulse, ablation of the target material and absorption by the resultant vapor leads to the formation of hot

[3] Inverse Bremsstrahlung: The process where an electron in a free state absorbs a photon and moves to a more energetic free state

high-density plasma on the surface of the target.

The pressure gradient experienced by this plasma is greatest in the direction normal to the surface which causes the characteristic rapid expansion of the plume outwards from the surface [6–8, 10, 11, 13]. Several sources point to additional contributions to the velocity of the plume due to electrostatic effects [8, 11]. The plasma expands away from the target near the ion sound speed in a narrow cone normal to the surface [9, 18]. As the plasma is accelerated away from the surface it also cools causing the flow velocity to become supersonic with respect to the now decreased ion sound speed.

As the plume continues to expand experimental results indicate that both the ion density and average ion energy remain strongly peaked around the central axis of expansion normal to the surface [8, 20–23]. The electron density has also been reported to have the same angular dependence with a strong correlation to the ion density over the full range of angles (see fig. 1.1)

While the actual structure of the plume does appear to harbour greater complexity [24], the strong correlation of electron and ion densities supports the assumption that the plasma of the laser ablated plume will be sufficiently quasi-neutral for the purpose of our modeling efforts (chapter 3).

The bulk of directly relevant experimental work utilizing Langmuir probes in characterizing laser ablated plumes has been carried out by the groups in Trinity College Dublin and Rinø National Laboratory in Denmark [8, 11, 12]. Their results are in agreement with the findings of other groups [7, 13, 14, 17] and present a comparable picture of the ablated plume structure as those measured using other methods, such as resonant holographic interferometry [9], CCD imaging [25], time and spatial resolved spectra [25–27] laser-induced fluorescence (LIF)[28] and time of flight mass spectrometry [29].

1.2 Langmuir Probes

In essence a Langmuir probe is a conductor which can be biased with respect to the plasma potential. When placed within a plasma the resultant current can be measured. Invariably, it is more complex than simply sticking a piece of wire into the plasma. From reviewing the literature there appears to be almost as many different probe configurations as there are groups using them. They can however be broken down into three broad groups defined by the shape of the probe tip. These are cylindrical [8, 12, 14, 30–34], spherical [30, 35] and planar [18, 30, 34, 36–41] with cylindrical by far the most popular. The cylindrical probe is a straight piece of wire typically made from tantalum or similar materials such as molybdenum, chosen for their high melting points and mechanical strength, tungsten and graphite are also popular choices. The planar probe by contrast is a flat conductor

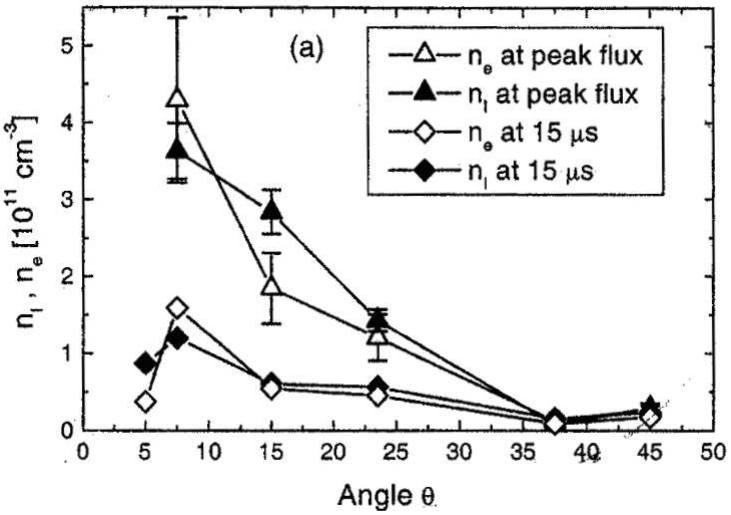

Figure 1.1: *Graph of the angular variation of electron and ion densities recorded 8cm from the target at peak ion flux and at 15 μs for a silver laser ablation plume produced by a 6 ns laser pulse at a fluence of 0.8 Jcm^{-2}. [8]*

typically single sided with the rest of the probe being insulated. The methods used as an insulator include a simple glass sleeve or coaxial cables built into the sleeve when sensitivity to noise is a major concern or a combination of the two for extra stability.

The choice of probe will depend largely on what characteristics of the plasma are of principal interest. For example planar probes while sensitive to plasma flow are not of use in measuring the electron saturation current as the current recorded depends on the probe geometry (fig. 1.2). The regimes in which the probe will operate and the properties of the plasma that are of interest will decide the choice of probe shape selected and by considering the bias to be applied the sheath size can be estimated and an appropriate probe size chosen so as not to perturb the plasma more than necessary [41]. The physical nature of the plasma (i.e. if its collisional or not) along with the type of probe chosen then dictates the probe theory used to interpret the results.

Depending on the design of probe chosen, it can be used to investigate many different characteristics of the plasma such as the electron density, electron temperature, ion density, ion temperature, floating potential, plasma potential and flow velocities [5, 18, 30–32, 35, 39, 40, 42]. These properties are derived from the analysis of the I-V trace (see figure 1.2). The I-V trace is generated by varying the bias applied to the probe and recording the total current (i.e. the combined electron and ion currents) to the probe. Care must be exercised in selecting the probe geometry and theory most appropriate for the physical parameters of the plasma being investigated.

The details of the various options available have filled entire books [43] and review articles [30] by themselves and are not dealt with here. Instead the different portions of the probe's I-V trace (fig. 1.2) along with what

information about the plasma can be extracted are outlined below.

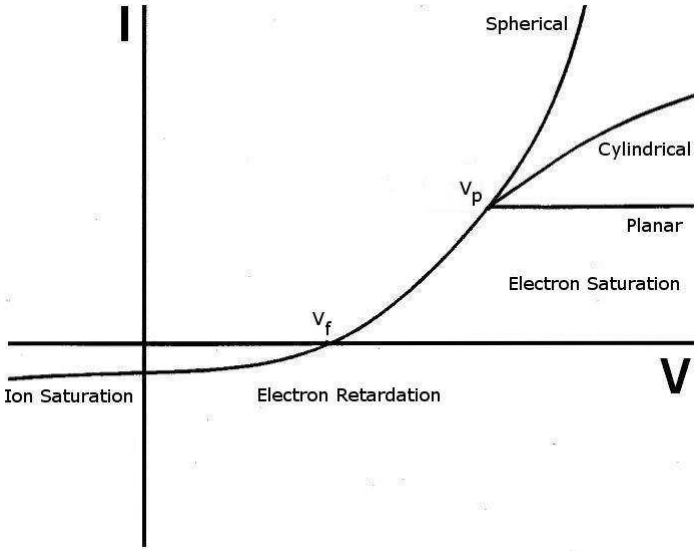

Figure 1.2: *Illustration of an idealised I-V result from Langmuir probes of different tip geometry [5].*

Starting at the application of a sufficiently negative potential (typically -10V or less) all the electrons are expelled from the immediate vicinity of the probe and only the ions attracted. This leads to the formation of a sheath which acts to shield the probe's potential from the rest of the plasma. With all of the electrons repelled the positive ions are the only particles collected hence this part of the I-V trace is the *ion saturation region.* The current measured by the probe in this region along with an appropriate probe theory allows the estimation of plasma ion density.

As the applied bias is raised the sheath decreases in size and electrons of sufficient energy start to reach the probe. With increasingly negative bias the *floating potential* (V_f) is reached at the point where the current measured is zero. Its occurrence indicates that the current due to ion and electron fluxes to the probe balance, as opposed to there being a true absence of current.

Below the floating potential we enter the *electron retardation region*. Here, as the bias applied to the probe becomes positive, the quantity of lower electron energies reaching the probe increases, so that the recorded current is some combination of the ion and electron currents. From this region the electron distribution function can be calculated and from it the electron temperature estimated.

The *plasma potential* (V_p) is the apparent potential of the bulk region of the plasma and the potential against which the bias to the probe is applied. The geometry of the probe being used and nature of the plasma will determine how it is calculated. For example, in the simplest case of a cylindrical probe in a collisionless plasma, the plasma potential can be found by taking the first derivative of the electron current and calculating where the maximum occurs.

Finally the *electron saturation region* lies beyond the plasma potential and while its value can be calculated from the curve the literature expresses concerns over the questionable accuracy [5, 30] due to the sensitivity of the resulting value to the geometry of the probe tip. In short the probe geometry affects the size and shape of the sheath which in turn affects the current collected.

An in depth description of the mathematical considerations for different probe geometries in various Maxwellian plasma can be found in the article by V.I. Demidov [30] and the topic of non-Maxwellian distributions is tackled by Godyak in [44].

1.2.1 Planar Langmuir Probes

Langmuir probes have long been used in the investigation of low temperature plasmas. Considerable development has been conducted on the theory for

stationary plasmas under these conditions [4, 45, 46] and more recently the diagnosis of plasmas produced through laser ablation [8, 11, 12]. Through the use of Langmuir probes, parameters such as plasma density, temperature, flow velocity and form of the plume expansion have been characterised [18]. To do this, the planar probe is typically oriented normal to the direction of flow in the path of the expanding plume. Under these conditions the probe can be negatively biased with respect to the plasma and the ion current measured. The measured current is independent of the bias on the probe as the ion flux to the surface of the probe is conserved. Assuming the ions to be singly charged it has been shown that the ion saturation current is dominated by the ion flux due to the probe and can be expressed as [47]

$$I_{ion} = Aen_i v_f, \tag{1.3}$$

where A is the probe area, n_i the ion density, v_f the ion flow velocity and e absolute electron charge. However, for the case where the planar probe is oriented parallel to the direction of flow the conservation of flux in the direction of flow no longer applies. Ions are now lost to the planar probe along the direction of flow when a negative bias is applied to the probe. Therefore the flux to the probe and by extension the current collected by the probe is dependent on the bias applied to the probe. The so far incomplete theory for probes operating under such condition in unmagnetized plasmas is addressed in this thesis.

1.2.2 Mach Probes

An extension to the Langmuir probe concept is the family of Mach probes. These probes are used in the measurements of the velocity of a flowing plasma. They are constructed from multiple DC biased probes shielded from

each other [43]. This allows them to separately measure the ion current from the upstream and downstream directions. There are two common configurations in the literature. The first (fig.1.3(a)(b)) consists of an array of two or more Langmuir type probes shielded from each other, which is sometimes mounted on a rotating mount [43, 48–50]. The other is the Gundestrup type probe developed by MacLatchy [51] which consists of two separate arrays of probes [35, 51, 52]. The first array functions as a standard Langmuir probe, while the second array consists of a circular array of probes again shielded from each other (fig.1.3(c)). This configuration has the advantage of allowing the measuring of density and temperature in addition to the velocity of the flowing plasma.

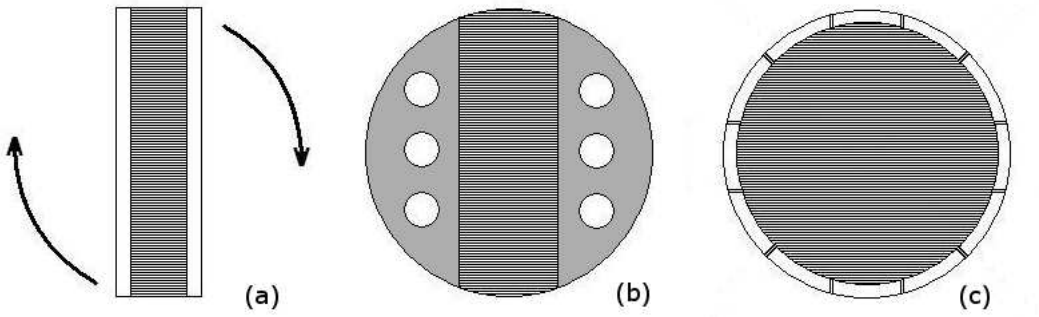

Figure 1.3: *Illustration of common configurations of Mach Probes documented in the literature. Note: hatched shaded areas insulated.*

As with the standard Langmuir probe these Mach probes require an appropriate theory to interpret the results. The theory is based on the difference in the ion saturation current measured by the different parts of the probe. For a plasma possessing a significant flow velocity along magnetic field lines the flux to the multiple probe surfaces will be different. It turns out that this ratio between the current measured on the upstream and downstream side of the probe is a function of the ratio between the ion sound speed and

the flow velocity. From this relationship it is possible to estimate the plasma flow velocity.

For Mach probes operating in the magnetized plasmas the theory has been well developed [48, 49, 51, 52]. For the case of a non-magnetized plasma there have been attempts to adapt the Mach probe theory of Hudis and Lindsky [1] such as those by Oksuz and Hershkowitz [53]. However inherent flaws in the original theory, namely its lack of a physical justification for key assumptions, lead to the invalidity of the resulting work. This has been highlighted in the paper by Hutchinson [54] and experimentally demonstrated by Ko and Hershkowitz [50], including the failure to predict the rather counter intuitive "asymmetry reversal" phenomena where a larger ion current is collected on the downstream side of the probe in the shadow of the flow.

1.3 Modeling of Plasmas

By its very nature experimental investigations will perturb the plasma under study. For example the physical modification of the chamber to include diagnostic equipment will have effects on the plasma generated. Plasma chemistry can be contaminated by techniques such as emissive probes or chamber deposition. Electrostatic probes can produce erroneous results due to unexpected differences between the physical geometry and the effective collecting area of the probe [41].

Modelling on the other hand allows the exploration of the underlying principles and behaviour of an idealised version of the plasma unperturbed by experimental intrusion. It allows for the examination of phenomena that do not readily lend themselves to experimental scrutiny. The parameters can be changed far more quickly and cheaply than a physical experimental setup.

Limits imposed by equipment quality other than computational resources can be bypassed. However physical experimental results should always remain the bench mark for determining the success and accuracy of a model.

There are five broad groupings of models used in plasma physics:

- *Analytical models* use mathematical equations to describe the behaviour and properties of particular region or phenomenon of the plasma. They are constructed using an understanding of the physical mechanisms involved to formulate the appropriate equations. These are then typically used to further investigate the process or allow the extraction of meaningful information from experimental results.

- *Equivalent Circuit models* use electrical components (resistors, capacitors, etc) arranged into circuits to replicate the electrical properties of the plasma. Different degrees of complexity from whole systems to just sheath behaviour can be simulated without a fundamental understanding of the mechanisms at work. This is also their key disadvantage as this simplistic approach means that they cannot provide any insight into those mechanisms.

- *Fluid models* treat the plasma as a fluid. The plasma is described by the transport equations which govern continuity, momentum and energy conservation. These are derived from the full Boltzmann equation and then closure is made by assuming a parametrization of the distribution function. Their biggest drawback however is the need for the particle distribution functions to be either assumed or supplied.

- *Kinetic models* simulate the behaviour of a plasma with individual particles rather than the assumed distributions of fluid models. The most well know example of a kinetic model is the Particle in Cell (PIC)

code (sec. 1.3.1). These track the motion of both particle ions and electrons from which the particle motion, potential and electric fields are calculated self-consistently. While almost ideal it comes at a far greater computational expense than other methods.

- Finally there are the *hybrid models* which represent a mix of two or more of the above methods. For example the hybrid PIC model substitutes the particle electrons of the full PIC model with a fluid model. As only the ion motion needs to be tracked, far larger time steps can be taken offering a considerable computational saving.

1.3.1 Particle in Cell Codes

One of the most powerful methods for plasma simulation is the family of Particle in Cell (PIC) models [55]. The plasma is simulated by a kinetic model composed of particle ions and electrons. The particles move under the influence of the electric fields within the plasma. These fields are calculated self consistently from the charge densities of the particles using a grid and Poissons' equation. The force exerted on the particles by the electric fields is calculated and applied to the particles which are then moved according to Newton's Laws.

Starting in the late fifties to the mid-sixties most computer models of plasmas tended to have been restricted to one dimensional simulations ([56] p.362). Here the particles were treated as planar sheets moving only in one axis. To allow for more complex effects to be considered various straight forward approximations were use to extend their capabilities, for example by treating the sheets as one dimensional cylindrical sheaths or the introduction of additional velocity components [57].

Then in the mid-sixties the idea of using spatial grids was introduced by Buneman, Hockney and others. This new method involved the dividing up of the region of interest into a grid of equal sized cells. The charge densities are then assigned to the grid points. The electric fields are then calculated across the grid. The force from these fields are then applied back onto the particles.

The use of the grid in this manner represents a huge saving in computational resources as the alternative would be the calculation of the coulomb interactions among all the particles. For a particle-particle scheme without a grid the calculations required scale as a factor of n^2 where n is the number of particles, while with the grid it scales in proportion to the number of particles [22, 57, 58].

This technique is easily scaled up to two dimensions where the area is now divided into cells of equally sized sides to form a mesh[4] [55, 57]. The size and resolution of the mesh depends on the scale of the phenomenon the code is aiming to simulate. Structures on a scale smaller than that of the mesh cannot be resolved.

As the field equations and the equations of motion are typically solved in explicit finite difference form, there are numerical stability conditions. These conditions are required to ensure the accuracy of the result and stability of the numerical method. In short a particle should not cross more than one cell in a time step and the time step must be small enough to resolve the particle motion. This is achieved by limiting the choice of cell size and time step. A full description of these conditions are detailed in Chapter 3, section 3.4.5.

The equation sets can also be solved using an implicit method which

[4]Here mesh is used to refer specifically to a 2D grid

does not require the use of stability conditions. The disadvantage though is that unlike the explicit method there is no certainly that physical results are accurate.

Operational flow of a PIC Code

The standard PIC model follows the set cycle of operations shown in fig. 1.4. First the region is divided up into a suitably sized grid.

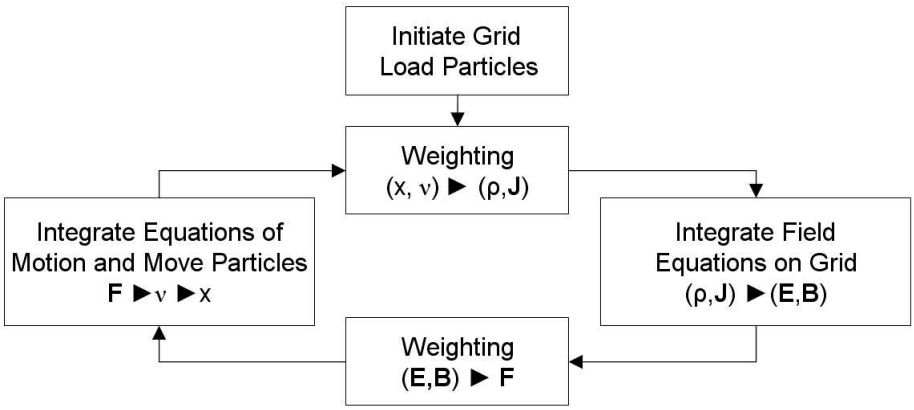

Figure 1.4: *The typical operation cycle of a Particle in Cell code covered over one time step. Weight particles to the grid, solve for fields, weight fields back to particles, move the particles and repeat [57].*

The grid is then loaded according to the physical parameters of the plasma with a appropriately distribution of *super particles*, each of which represents a set number of real particles. This is a necessary compromise as tracking 10^{14} to 10^{24} real particles is impossible. So through the use of a lesser number of super particles the computational cost is minimized while preserving the complex behaviour, allowing the meaningful physics of the system to be observed.

The next step involves the assignment of the charge densities to the grid. To do this a weighting is used in dividing the contribution of each parti-

cles' charge to the surrounding grid points. The interpolation used to do this depends on the systems' tolerance to numerical noise and the accuracy required versus considerations for the time and computational resources available [55, 56, 58]. Methods available range from the cheap and noisy nearest grid point assignment (NGP) to progressively more expensive but quiet higher order methods across multiple grid points.

Next the field equations are integrated across the grid, again using an appropriate method. For example in the case of a one dimensional electrostatic model without magnetic fields the Poisson equation solved in finite-difference form is sufficient. For higher dimensions and electromagnetic fields the full Maxwell's equations would be used.

These fields are then interpolated back onto each particle using the same weighting scheme as before and the equations of motion integrated to work out the force on each particle. The particle is then moved accordingly. The new position and velocity of each particle are updated and the whole process repeated for another time step.

Additional operations can be added to this cycle as required. For example Monte Carlo collision treatments, particle interaction with surfaces and particle sources within the plasma are all frequent extensions.

Due to the numerical nature of these models care must be taken in the selection of grid size and time step in order to ensure the efficiency and stability of the code. Additionally the initial and boundary conditions of the physical system must be rigorously tested as a poor choice can lead to non-physical results, some of which may not be immediately apparent. For more in depth discussion three excellent review articles are found in the literature [57–59].

1.3.2 Hybrid Particle in Cell Codes

Hybrid Boltzmann-PIC codes are as the name suggests a combination of two modelling techniques. The ions are modelled using the standard particle in cell method while the electrons are described by a fluid model. This simplification requires that the electron's can be assumed to have a Maxwell-Boltzmann distribution.

Under these two condition the relationship between the electron density and the plasma potential closely follows the simplified Boltzmann relation

$$n_e = n_0 exp \frac{e\Phi}{k_B T_e}, \tag{1.4}$$

where n_0 is the undisturbed plasma density, n_e is the electron density, Φ is the plasma potential, k_B is the Boltzmann constant and T_e the electron temperature.

Removing the requirement for the code to resolve the kinetic motion of the electrons lifts the limitation on the time step size imposed by the electron plasma frequency. The smaller ion frequency allows for time steps several orders of magnitude larger to be taken. This reduces the total number of steps needed and greatly speeds up the time taken for the simulation to run.

CHAPTER 2

Analytical Model

In order to interpret the experimental results from electrostatic probes, a firm understanding of the physical processes involved is required. Typically, this understanding is used to construct an analytical model of the probe's interaction with the plasma. The model is then used to determine quantitative values for the physical characteristics of the plasma such as the temperature and density of difference species from experimental results. Armed with such a model, probe diagnostics can be used to gain insight into the behaviour of plasma or control an industrial process.

The theory for such probes operating in plasma with a significant directed flow velocity is incomplete. Theories describing the interaction of probes with both magnetized and un-magnetized plasma in the subsonic regime (i.e. flow velocities less than the ion sound speed) have been developed [43]. The theory for magnetized plasma with a supersonic flow has also been developed

[48, 49, 51, 52]. It is for probes interacting with an un-magnetized plasma possessing a supersonic flow that a satisfactory theory is still required [54].

Most standard probe models are one dimensional in nature and are based on simple and solid relationships which use energy conservation to derive the potential [5, 43]. However, in the case of a supersonic plasma flow there is often no simple relationship on which to build a theory [54], for example in the case of a double sided planar Langmuir probe oriented normal to the direction of flow. The current to the upstream side of the probe is largely independent of applied potential except at very high values as the flux is conserved in the direction of flow. On the downstream side of the probe the case is very different as the current is dependent on the potential's ability to decelerate and capture ions initially moving away from the probe. This flux will be drawn in sideways from the flow so the conservation of flux can no longer be applied. Hutchinson points out that this sideways motion of particles across the flow invalidates any attempt to use a one dimensional model [54]. The development of a satisfactory theory is further hampered by the difficulty in defining the potential drop on the downstream side of the probe.

The analytical model presented in this chapter aims to go some way towards filling this gap. It aims to describe the interaction between a plasma with supersonic flow and a planar Langmuir probe. For the general case of arbitrary probe size and orientation to the flow the problem is clearly three dimensional. Under certain condition it can be shown that there is a quasi-one dimensional solution, which is limited in scope, as its validity rapidly becomes questionable beyond the ion saturation region of the I-V trace (fig. 1.2). Key assumptions of the model limit it to probes of planar geometry with their surface oriented parallel or near parallel to the direction of flow.

This solution is based in part on a slightly modified version of a model by Riemann and Daube [45] which has been re-derived without their unit normalisation or the assumption of an initial flow toward the probe at the ion sound speed. This allow for its application to a flowing plasma under the condition outlined in section 2.2. It has also been further extended to allow the calculation of the total ion current collected by the probe under these conditions. In addition a method for measuring the flow velocity of an unmagnetized plasma is presented.

2.1 The Riemann and Daube Model

Riemann and Daube developed the analytical model [45] to describe the ion current to an electrode in a stationary plasma from the relaxation of a collisionless ion matrix sheath, during the industrial process of plasma immersion ion implantation (PIII). Their model is itself a refinement of an earlier work by Lieberman [60] which avoids that model's various artificial requirements. They model the system as a one dimensional plasma in contact with the planar substrate. The evolution in time of the plasma sheath and current density at the substrate is then predicted by their model (fig. 2.1a).

PIII is a widely used industrial technique which involves the immersion of a substrate in plasma for the purpose of controlled implantation of material into its surface. To achieve this implantation a very large negative bias pulse is suddenly applied to the substrate (up to $50kV$). This repels the electrons from the substrates surface leaving a high population of the slower moving ions behind, forming a matrix sheath. The width of this sheath s_0 is described by the equation

$$s_0 = \sqrt{\frac{2\epsilon_0 V_0}{e n_0}}, \tag{2.1}$$

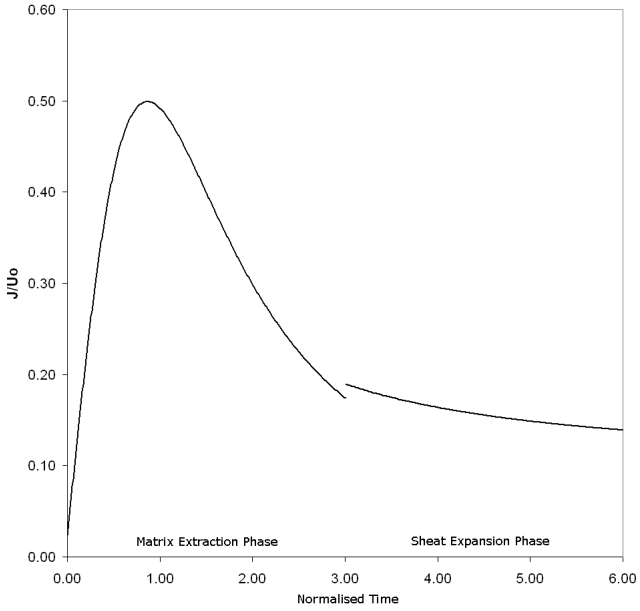

(a) Normalised Current Density

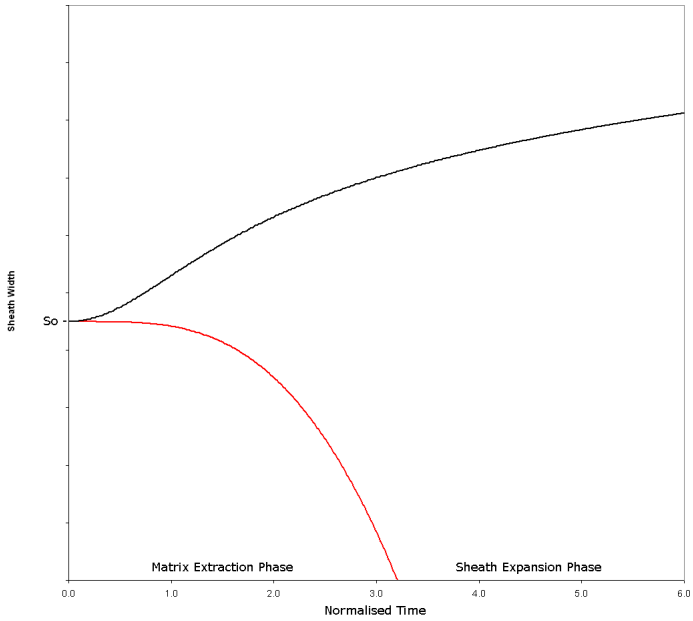

(b) Sheath Evolution

Figure 2.1: *Diagrams of the Riemann and Daube PIII model's predicted (a) current density and (b) sheath expansion for the two phases of the sheath evolution over a normalised time ($\omega_i t$). In (b) the black line denotes the sheath width and the red line traces the path of an ion entering the sheath at s_0 at $t = 0$.*

where V_0 is the probe bias and n_0 the bulk plasma density. The exposed ions are then rapidly accelerated across the sheath by the potential imbedding them in the surface. This phase is referred to as the "matrix extraction phase" in their model [45].

As ions are lost to the surface, the sheath expands outwards. In time, all of the ions initially uncovered by formation of the matrix sheath have reached the surface (fig. 2.1b). From this time on, it is only ions uncovered by the expansion of the sheath that are incident on the substrate. This second stage is approximated by an adaptation of the quasi-static Child Langmuir law [60] and is referred to as the "sheath expansion phase".

2.2 Model and Assumptions

The model that follows aims to describe the interactions between the plasma and the planar Langmuir probe oriented parallel or nearly parallel to a flowing plasma (fig. 2.2a). The purpose is to calculate the total current collected by a probe of length L and width W.

To do this we use a modified version of the Riemann and Daube model [45] which is re-derived in non-normalised units to describe sheath structure (sec. 2.3). Their model describes the evolution of the sheath in time. In our model we use this evolution in time to represent the evolution of a slice of the plasma as it travels along the probe's length (fig. 2.2b) by

$$\tau = \frac{y}{u_f}, \tag{2.2}$$

where τ is the time, y the position and u_f the plasma flow velocity.

As we assume that the flow is homogenous upstream of the probe and that any velocity u_y is negligible compared to the flow velocity u_f, this enables

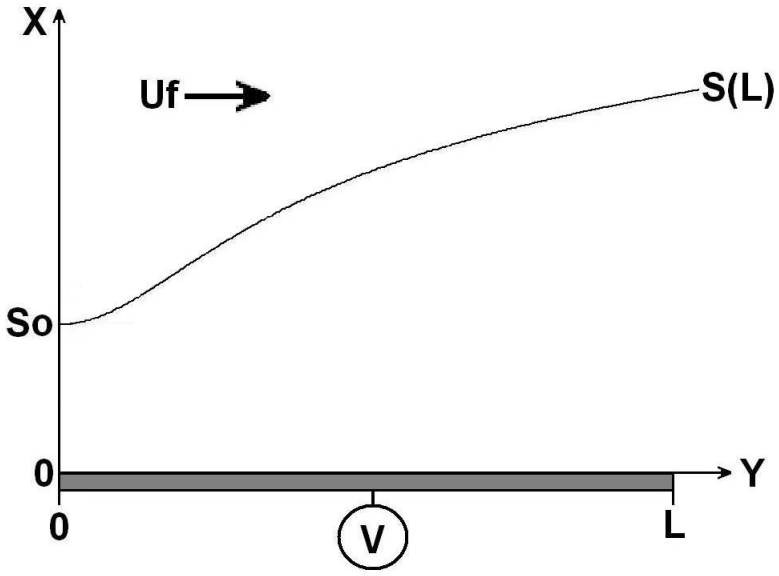

(a) Diagram of the physical system.

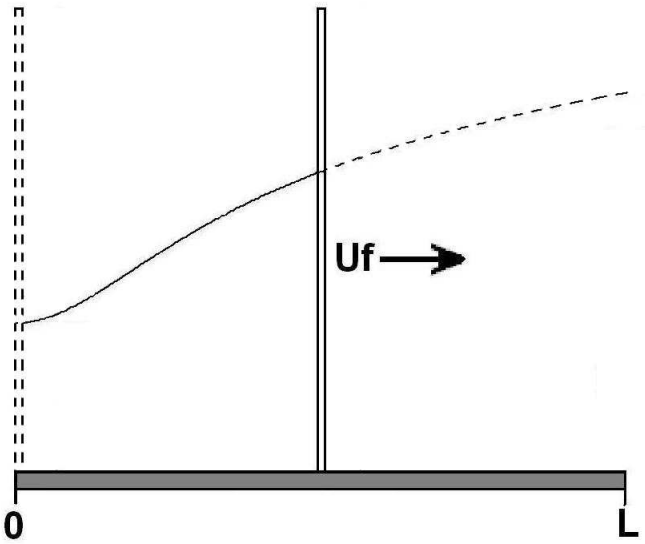

(b) 1D models description of 2D system.

Figure 2.2: *(a) Diagram of the physical system of a probe of length L and bias V with a sheath of width S in a plasma of flow u_f. (b) Diagram showing how the 1D evolution of the model in time is related to the evolution along the probe's length by $\tau = y/u_f$*

the creation of an expression for the current density $J(x = 0, 0 < y < l)$ along the probe's length covered by the *matrix extraction phase* (sec. 2.4).

With this expression and our own extension to cover the *sheath expansion phase* (sec. 2.5) the equations can be integrated along the length of the probe and multiplied by the probe's width to give the total ion current to the probe. This is done for the probe oriented parallel (sec. 2.6.1), upstream (sec. 2.6.2) and downstream (sec. 2.6.3) of the plasma flow.

We make the following assumptions:

- The ion motion in the sheath is collisionless.
- The plasma consists of singly charged ions of density n_i and electrons of density n_e.
- $u_f > u_B$, the flow velocity u_f of the plasma is supersonic with respect to the ion sound speed u_B.
- $n_i = n_e = n_0$, before the plasma flow encounters the probe it is homogeneous and quasi-neutral.
- As the flow is supersonic, disturbances are unable to propagate upstream.
- Electrons are represented by a Boltzmann fluid (sec. 1.3.2) with temperature T_e and ions by a cold fluid.
- $\omega_{pe} >> \omega_{pi}$, i.e. the electrons react instantaneously compared to the ions.
- $u_0 = 0$, for the probe oriented parallel to the direction of flow.
- $u_y = u_f$ for the probe oriented parallel to the direction of flow.

- $u_0 = u_f Sin\theta$, for the probe oriented θ degrees off parallel to the direction of flow.
- $u_y = u_f Cos\theta$ for the probe oriented θ degrees off parallel to the direction of flow.

The probe surface is oriented parallel or near parallel to the direction of flow (fig. 2.2a). The probe has a length L in the direction of the flow and is assumed to be of sufficient width to prevent edge effects dominating. The x-axis is designated the direction normal to the surface and the y-axis is parallel to the probe's surface in the direction of flow. The leading edge of the probe is defined to be located at $x = y = 0$. This results in the following boundary conditions at the leading edge of the probe for density $n_i(x,0) = n_e(x,0) = n_0$ and ion velocity $\mathbf{u}_i(x,0) = (0, u_f)$.

2.3 Basic Equations

The conservation equations for the ion density and momentum in the absence of a magnetic field are written

$$\frac{\partial n_i}{\partial t} + \nabla \cdot (n_i \mathbf{u}_i) = 0, \tag{2.3}$$

$$m_i n_i \left[\frac{\partial \mathbf{u}_i}{\partial t} + (\mathbf{u}_i \cdot \nabla)\mathbf{u}_i \right] = e n_i \mathbf{E}, \tag{2.4}$$

where $\mathbf{E}$ is the electric field intensity. As both the density and velocity of the flow are considered constant at the leading edge of the probe, the partial time derivatives can be discarded and the equations rewritten explicitly in

terms of the velocity components along the x and y axis

$$\frac{\partial}{\partial x}(n_i u_x) + \frac{\partial}{\partial y}[(u_y + u_f)n] = 0, \tag{2.5}$$

$$u_x \frac{\partial u_x}{\partial x} + (u_y + u_f)\frac{\partial u_x}{\partial y} = eE_x, \tag{2.6}$$

$$u_x \frac{\partial u_y}{\partial x} + u_y \frac{\partial u_y}{\partial y} = eE_y, \tag{2.7}$$

where $\mathbf{u}_i = (u_x, u_y + u_f)$ and u_y is any initial velocity not flow related. On the condition that u_y can be discarded relative to u_f the first two equation can be rewritten

$$u_f \frac{\partial n_i}{\partial y} + \frac{\partial}{\partial x}(n_i u_x) = 0, \tag{2.8}$$

$$u_f \frac{\partial u_x}{\partial y} + u_x \frac{\partial u_x}{\partial x} = eE_x. \tag{2.9}$$

To determine the electric field in the above equations we solve Poisson's equation:

$$\nabla^2 \Phi = -\frac{e(n_i - n_e)}{\epsilon_0}, \tag{2.10}$$

with the following boundary conditions:

- $\Phi(0, 0 \leq y \leq L) = V$, i.e. the potential along the surface of the probe is equal to the applied potential.
- $\Phi(\infty, 0 \leq y \leq L) = 0$, i.e. the potential vanishes far from the probe.

In one dimension Poisson's equation reduces to

$$\frac{d^2\Phi}{dx^2} = -\frac{e(n_i - n_e)}{\epsilon_0}. \tag{2.11}$$

It now becomes convenient to replace y in equations (2.8) and (2.9) with τ, measuring time from the point of view of the slice of plasma (see fig. 2.2b).

Equations (2.8),(2.9) and (2.10) can then be written in the form

$$\frac{\partial n_i}{\partial \tau} + \frac{\partial}{\partial x}(n_i u_x) = 0, \tag{2.12}$$

$$\frac{\partial u_x}{\partial \tau} + u_x \frac{\partial u_x}{\partial x} = eE_x, \tag{2.13}$$

$$\frac{\partial E_x}{\partial x} = \frac{e(n_i - n_e)}{\epsilon_0}. \tag{2.14}$$

In this form, the equation set is almost identical to the initial equation set of the Riemann and Daube model [45] to describe the relaxation of an ion matrix in time t. However, the initial ion velocity towards the probe is no longer assumed to be the Bohm velocity ($u_x \neq u_B$).

Taking advantage of the similarities between the models we can proceed in the same manner. Utilizing both the *ansätze*

$$n(x,\tau) = \bar{n}(\tau) = \int_0^S n(x,\tau)dx,^{1} \tag{2.15}$$

and

$$u_x(x,\tau) = \upsilon(\tau) + a(\tau)x \tag{2.16}$$

proposed by Riemann[45] the equations can be written in the form

$$\frac{d\bar{n}}{d\tau} + \bar{n}a = 0, \tag{2.17}$$

$$\frac{d\upsilon}{d\tau} + x\frac{a}{\tau} + (\upsilon + ax)a = -\frac{e}{m_i}\frac{\partial \Phi}{\partial x}, \tag{2.18}$$

$$\frac{\partial^2 \Phi}{\partial x^2} = -\frac{e\bar{n}}{\epsilon_0}, \tag{2.19}$$

where

$$a \equiv -\frac{1}{\bar{n}}\frac{d\bar{n}}{d\tau}. \tag{2.20}$$

Differentiating equation (2.18) with respect to x and substituting equation (2.19) yields

$$\frac{da}{d\tau} + a^2 = \omega_i^2 \frac{\bar{n}}{n_0}. \tag{2.21}$$

[1] The ion distribution within the sheath is approximated by a homogenous population.

where ω_i is the ion plasma frequency. The solution of equation (2.21) is given by

$$\bar{n}(\tau) = \frac{2n_0}{2 + (\omega_i \tau)^2}. \tag{2.22}$$

Equation (2.18) can now be rewritten using equation (2.21) to give

$$\frac{d\upsilon}{d\tau} - \frac{d\bar{n}}{d\tau}\frac{\upsilon}{\bar{n}} + \omega_i^2 x \frac{\bar{n}}{n_0} = -\frac{e}{m_i}\frac{\partial \Phi}{\partial x}, \tag{2.23}$$

which can be rewritten

$$\bar{n}\frac{d}{d\tau}\left(\frac{\upsilon}{\bar{n}}\right) + \omega_i^2 x \frac{\bar{n}}{n_0} = -\frac{e}{m_i}\frac{\partial \Phi}{\partial x}, \tag{2.24}$$

using the inverse chain rule

$$\frac{1}{\bar{n}}\frac{d\upsilon}{d\tau} - \frac{\upsilon}{\bar{n}^2}\frac{d\bar{n}}{d\tau} = \frac{d}{d\tau}\left(\frac{\upsilon}{\bar{n}}\right). \tag{2.25}$$

To derive an expression for the velocity within the sheath this equations is then integrated with respect to x with the boundary conditions

$$u_x(x, 0) = u_0, \tag{2.26}$$

$$\Phi(0, \tau) = V, \tag{2.27}$$

$$\Phi(s_0, \tau) = 0, \tag{2.28}$$

where s_0 is the sheath width (4.2). This yields the equation

$$x\bar{n}\frac{d}{d\tau}\left(\frac{\upsilon}{\bar{n}}\right) + \frac{1}{2}x^2\omega_i^2\frac{\bar{n}}{n_0} = -\frac{e}{m_i}\{\Phi + \varphi(\tau)\}, \tag{2.29}$$

where the arbitrary functions φ and υ are chosen to satisfy the boundary conditions.

The first boundary condition (2.27) on Φ implies that $\varphi(\tau) = -V$. Substitution of the sheath edge condition (2.28) on Φ into equation (2.29) yields

$$s_0\bar{n}\frac{d}{d\tau}\left(\frac{\upsilon}{\bar{n}}\right) + \frac{1}{2}s_0^2\omega_i^2\frac{\bar{n}}{n_0} = -\frac{1}{2}s_0^2\omega_i^2, \tag{2.30}$$

or

$$\frac{d}{d\tau}\left(\frac{\upsilon}{\bar{n}}\right) = -\frac{1}{2}\frac{\omega_i^2 s_0}{n_0}\left\{1+\frac{n_0}{\bar{n}}\right\}, \tag{2.31}$$

so that

$$\upsilon(\tau) = u_x(0,\tau) = \frac{\bar{n}}{n_0}\left[u_0 - \omega_i^2 s_0\tau - \frac{1}{12}s_0\omega_i^4\tau^3\right], \tag{2.32}$$

and

$$u_x(x,\tau) = \frac{\bar{n}}{n_0}\left[u_0 - \omega_i^2(s_0-x)\tau - \frac{1}{12}s_0\omega_i^4\tau^3\right]. \tag{2.33}$$

To derive an expression for the potential across the ion matrix sheath, equation (2.29) can be rearranged to get

$$-\frac{e}{m_i}\Phi(x,\tau) = \frac{1}{2}\frac{\bar{n}}{n_0}x^2\omega^2 + x\bar{n}\frac{d}{d\tau}\left(\frac{\upsilon(\tau)}{\bar{n}}\right) + \frac{e}{m} + \varphi(\tau). \tag{2.34}$$

Substituting in equation (2.32) and applying the boundary condition that at $x = s_0$ then $\Phi(s_0,\tau) = 0$ we find

$$\varphi(\tau) = \left(\frac{\omega_i^2 m_i}{e}\right)\frac{s_0^2}{2}. \tag{2.35}$$

Using $\varphi(\tau)$ and engaging the expression for the plasma frequency

$$\omega_i^2 = \frac{e^2 n_0}{\epsilon_0 m_i}, \tag{2.36}$$

results in

$$\Phi(x,\tau) = \frac{e}{\epsilon_0}\left(\frac{\bar{n}x^2 - \bar{n}xs_0}{2}\right) - \frac{en_0}{\epsilon_0}\left(\frac{xs_0 - s_0^2}{2}\right), \tag{2.37}$$

the expression for the potential across the ion matrix sheath.

2.4 Matrix Extraction Phase

The matrix extraction phase lasts from the moment the plasma first encounters the probe to the point where ions beginning at the sheath edge ($x = s_0$

at $\tau = 0$) reach the surface of the probe. To calculate the current during this phase an expression for the current density J_i along the length of the probe's surface is required.

The current density is determined by the flux to the surface

$$J_i = e\bar{n}u_x. \tag{2.38}$$

Substituting in the expression for density (2.22) and velocity (2.33) yields

$$J_i = \frac{en_0[u_0 - \omega_i^2(s_0 - x)\tau - \frac{1}{12}s_0\omega_i^4\tau^3]}{[1 + (\omega_i\tau)^2/2]^2}. \tag{2.39}$$

The current density along the surface of the probe at $x = 0$ is thus

$$J_i(\tau) = \frac{en_0[u_0 - s_0(\omega_i^2\tau + \frac{1}{12}\omega_i^4\tau^3)]}{[1 + (\omega_i\tau)^2/2]^2}. \tag{2.40}$$

As pointed out by Riemann in his model[45], this expression holds only during the matrix extraction phase, because of the assumed homogenous ion distribution within the ion matrix sheath (2.15). Once all the ions within this region have reached the probe this approximation is no longer valid. After this point only ions uncovered by the sheath's expansion now contribute to the ion current.

The time at which this occurs, is determined by how long an ion initially at $s_1(0) = s_0$ takes to travel to the surface (i.e. What point along the length of the probe it strikes). Again in the same fashion as Riemann only working in un-normalised units and with the arbitrary initial velocity u_0 towards the probe, this is described by the differential equation

$$\frac{ds_1}{d\tau} = u(s_1, \tau). \tag{2.41}$$

Substituting in expression (2.33) for the velocity, then making use of equation (2.22) and multiplying across by e yields

$$\frac{d(ns_1)}{d\tau} = \bar{n}\upsilon(\tau), \tag{2.42}$$

$$e\frac{d(ns_1)}{d\tau} = e\bar{n}\upsilon(\tau) = J_i(\tau), \tag{2.43}$$

which shows the initial homogenous population of ions in the sheath decreases by the amount lost to the probe. This is then integrated with respect to τ yielding

$$e\bar{n}(\tau)s_1(\tau) - e\bar{n}(0)s_1(0) = \int_0^\tau J(\tau)d\tau, \tag{2.44}$$

$$e\bar{n}(\tau)s_1(\tau) = en_0s_0 + \int_0^\tau J(\tau)d\tau, \tag{2.45}$$

which relates the current number of ions within the sheath at τ to the original number of ions minus the total lost to the the probe. From this the position of $s_1(\tau)$ is found to be

$$s_1(\tau) = \frac{5s_0}{6} + \frac{u_0\tau}{2} + \left(\frac{2+(\omega\tau)^2}{2}\right)\left[\frac{u_0}{\omega\sqrt{2}}tan^{-1}\left(\frac{\omega\tau}{\sqrt{2}}\right) + \frac{s_0}{6}\left(1 + ln\left(\frac{2}{2+(\omega\tau)^2}\right)\right)\right], \tag{2.46}$$

in terms of τ.

By comparing the results of the analytical model against those of the 2D hybrid PIC code, the point y_{end} along the probe where this happens in the parallel case corresponds to approximately

$$y_{end} \approx \frac{3u_f}{\omega_{pi}}. \tag{2.47}$$

Unsurprisingly this agrees with the value suggested by Rienmann [45] in his paper. In the case of an orientation other than parallel, the positions of this point move based on the magnitude and direction of the initial plasma flow velocity u_0.

2.5 Sheath Expansion Phase

Sheaths form as charged particles move to shield out the presence of a potential from the rest of the plasma. In the case of a negative potential, electrons

are repelled and ions attracted. To screen out a set potential the sheath requires an appropriate number of ions to be present within it.

In the steady state of a Child Law sheath, the sheath width is constant, with the number of ions entering the sheath equal to the number lost to the surface [4]. However, the artificially high initial ion population of the matrix sheath does not share this equilibrium. As ions are lost to the surface the sheath width must expand to maintain the required number of ions within the sheath to continue to shield the potential.

For the latter part of the probe lying outside the matrix extraction phase, the sheath is expanding outwards and the distribution of the ions within the sheath is inhomogeneous. As has been pointed out by both Liebermann [60] and Riemann [45, 46] there is little or no hope of finding a rigorous analytical solution under these conditions.

We considered three different approaches for estimating the current density during during the sheath expansion phase. This first was the original model suggested by Riemann in his paper [45], who proposed an approximation for the current using an expression for the sheath balance,

$$\frac{ds}{d\tau} = u_0 - \frac{1}{en_0} J_i(\tau) + \frac{\epsilon_0}{en_0} \frac{d}{d\tau} \frac{\partial \Phi(0,\tau)}{\partial x}, \tag{2.48}$$

given here in unnormalized units with an arbitrary initial velocity towards the surface of the probe u_0. This expression relates the loss of ions to the wall, to the sheath's rate of expansion (*Appendix B*), thus allowing the current density at the wall to be calculated if the field strength at the wall $\Phi(0,t)$ and the sheath rate of expansion were known.

He then proposed that by the end of the matrix extraction phase the sheath obeyed the Child-Law conditions sufficiently well[2], that its expressions

[2] An assumption not borne out by result or numerical simulation.

for field strength and sheath width could be used to satisfy the balance equation. The resulting expression, again given here in unnormalized units with an arbitrary initial velocity, yields,

$$J_i(0,\tau) = en_0u_B - \beta\left(en_0 + \frac{\alpha V_0\epsilon_0}{s(\tau)^2}\right)\left(\frac{2}{9}\frac{s_0^2u_c}{s(\tau)^2} - u_0\right), \quad (2.49)$$

where $s(\tau)$ is the sheath expansion rate,

$$u_c = \left(\frac{2eV_0}{m_i}\right)^2, \quad (2.50)$$

is the characteristic ion velocity, α and β are the same fitting parameters suggested by Riemann[3]

$$\alpha = \frac{5}{3}, \quad (2.51)$$

$$\beta = 1 + \frac{2s_0^2}{s\tau^2}. \quad (2.52)$$

The introduction of the two fitting parameters is required to provide satisfactory agreement to the numerical solution as without them the agreement is very poor.

The second approach considered was adapting an improved late time model by Israel[46] for the field strength at the surface and the sheath's expansion in an attempt to avoid the fitting parameters. Israel's improved model was based on the unipolar ion sheath theory described in papers by Benilov[62] and Riemann[63]. The unipolar ion sheath region is defined as the electron free region of the sheath starting at the surface and extending out to the point where

$$n_e = 0.1n_0. \quad (2.53)$$

[3]While Riemann's choice of β appears arbitrary the choice of α is a reasonable assumption as it matches the value proposed by Birdsall [61] and Lieberman [60] for a Child Law Sheath.

with the accurate description of the region by a matched asymptotic expansion. However, while it provided superior expressions for the field strength at the surface and the sheath's expansion, the solution for the current density at the surface

$$J_i(0,\tau) \;=\; en_0u_B - \left(en_0 + \frac{\alpha V_0\epsilon_0}{s(\tau)^2}\right)\left(\frac{s_c^2u_B}{s(\tau)^2} - u_B\right) \tag{2.54}$$

surprisingly proved even poorer.

While the methods based on the Riemann and Israel models produced expressions for the current density, neither can be integrated successfully to provide an analytical expression for the total ion current I to the probe. In the end a third approach was taken to approximate the current density over the sheath expansion phase J_{se}.

Assuming a constant bias on the probe is maintained, then from the moment after the matrix sheath forms it begins to evolve towards a Child-Law like sheath. There is an intermediate period as one sheath regime gives way to the other.

Strictly speaking the expression for the current density (2.40) along the early part of the probe is only accurate to the end of the extraction phase. However without any real physical justification, the expression for the current density J_{me} from the matrix extraction phase can be extended into the sheath expansion phase. As the output drops to zero over τ an increasing portion of the standard Child-Law current density[4]

$$J_{cl} = en_0u_B, \tag{2.55}$$

is included.

With this approximation in mind we proposed the following

$$J_{se}(0,\tau) = J_{me}(0,\tau) + (J_{cl}\times\gamma), \tag{2.56}$$

where J_{me} is equation (2.40), J_{cl} is the Child-Law current density and γ is a free parameter.

Searching for a appropriate value for γ, the relationship

$$\gamma = \frac{s_0}{s_{cl}}, \tag{2.57}$$

between the initial matrix sheath width s_0 and the Child-Law sheath width s_{cl} was found to give satisfactory agreement with the numerical results from the 1D hybrid PIC code.

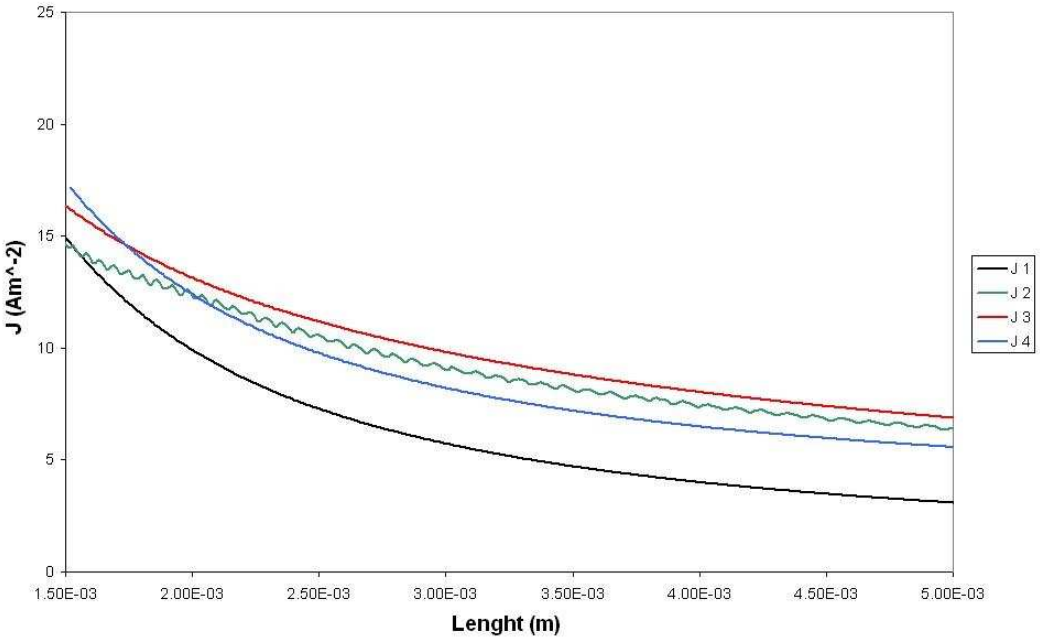

Figure 2.3: *Comparison of the current densities over the sheath expansion phase of a 5mm probe. Here J1 is the early time equation (2.40), J2 is the result of the 1D Hybrid PIC model, J3 is the late time model based on Riemann's work (2.49) and J4 is our proposed model (2.56). The Israel derived model (2.54) is not shown as its estimate of J is too low to be meaningfully graphed.* $V_0 = -32\,V$; $T_e = 0.22\,eV$; $n_0 = 7 \times 10^{16}\,m^{-3}$; $m_i = 1.79 \times 10^{-25}\,kg$

The results of the different methods are compared in fig. 2.3 against the

results of the 1D hybrid PIC model. The analytical approximation (2.56) proposed here gives acceptable agreement in comparison to both the results of the numerical simulation and those of the model proposed by Riemann (2.49). While it does not have the other's rigourous physical justification, it does have the advantage of allowing the current density to be integrated over the full length of the probe to create an analytical expression for the total current collected by the probe.

2.6 Total Ion Current

The total ion current collected by the probe is the sum of the currents collected over the full length of the probe (fig. 2.4). The leading part of the probe operates under the matrix extraction regime (section 2.4) while the latter section of the probe operates under the sheath expansion regime (section 2.5).

The ion current collected over the matrix extraction phase is found by integrating the expression for the current density (2.40) along the appropriate length of the probe and multiplying by the width of the probe. The equation (2.56) can likewise be integrated and multiplied by the width for the current over the sheath expansion phase.

It had been originally been planned to calculate the ion current during the sheath extraction phase using either the adapted Riemann model (2.49) or the Unipolar model (2.54). However the term for the sheath width $s(\tau)$ has a natural log that prevents their integration except by numerical means. So the crude approximation (2.56) must be used instead.

Taking the sign convention that the current collected by the probe is

positive, the total current I_{total} is described by

$$I_{total} = (I_{me} + I_{se}) \times W, \tag{2.58}$$

where W is the probe width. If the length of the probe L_2 is less than L_1 (fig. 2.4) then the I_{se} contribution is neglected.

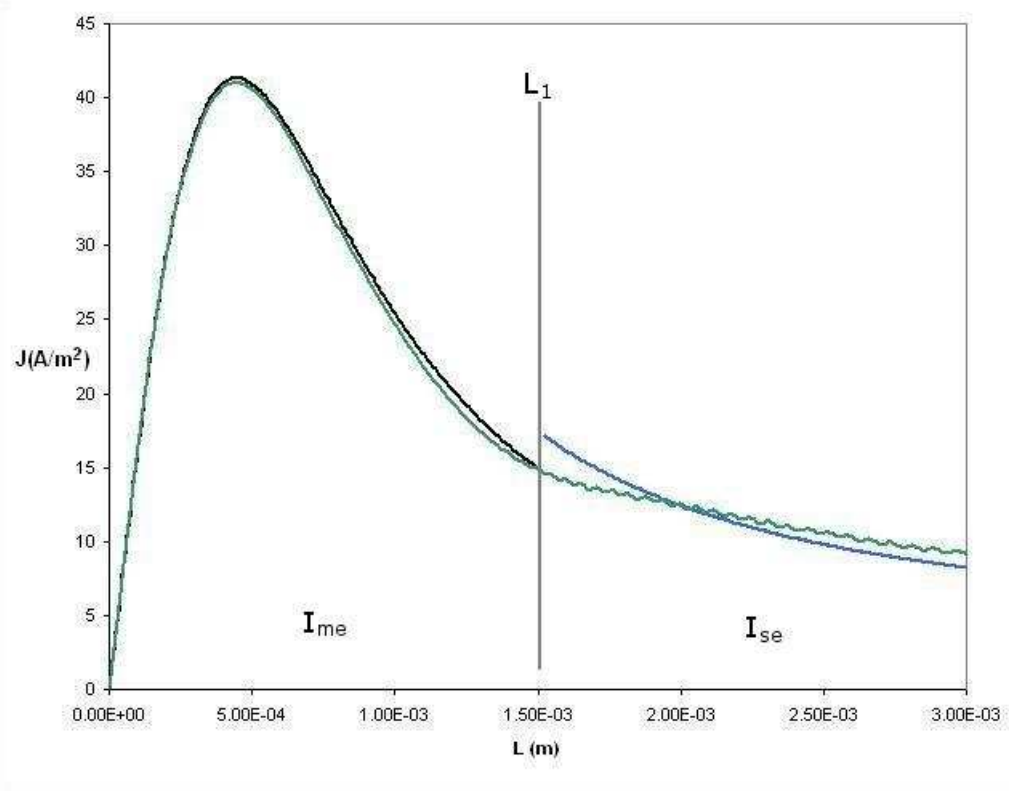

Figure 2.4: *Graph of the current density along the length of the probe showing which regions I_{me} and I_{se} apply to, with numerical results for comparison (green line). J_{me} is traced in black, J_{se} is traced in blue and the boundary between the two phases at L_1.*

Starting with equation (2.40) we use the relationship

$$\tau = \frac{y}{u_f}, \tag{2.59}$$

between τ and length to integrate the current density with respect to length.

$$I_{me} = -\int_0^L J_{me}(0,y)dy, \tag{2.60}$$

$$= -\frac{u_f}{\omega_i}\int_0^{\frac{L\omega_i}{u_f}} J_{me}(z)dz, \tag{2.61}$$

$$= \frac{en_0u_f}{\omega_i}\left[s_0\omega_i\int_0^{\frac{L\omega_i}{u_f}}\frac{(z+z^3/12)dz}{(1+z_2/2)^2} - u_0\int_0^{\frac{L\omega_i}{u_f}}\frac{dz}{(1+z_2/2)^2}\right], \tag{2.62}$$

where $z = \omega_i\tau = \omega_i y/u_f$ and I_{me} is the current per unit length (Am^{-1}) in the direction parallel to the flow.

2.6.1 Parallel Condition

The simplest case arises when the surface of the probe is oriented parallel to the direction of flow. Under this condition no component of the flow velocity u_f is directed toward the probe's surface. Additionally the assumption of a supersonic flow means disturbances should not propagate upstream. Thus it is reasonable to assume that there is no initial flow towards the surface of the probe, $u_0 = 0$.

Under this condition equation (2.62) for I_{me} takes the form

$$I_{parallel} = en_0u_fs_0\int_0^{\frac{L_2\omega_i}{u_f}}\frac{(z+z^3/12)dz}{(1+z_2/2)^2}, \qquad (Am^{-1}) \tag{2.63}$$

when integrated this yields

$$I_{parallel} = \frac{1}{6}en_0s_0u_f\left[ln\left\{1+\frac{1}{2}\left(\frac{L_2\omega_i}{u_f}\right)^2\right\} + \frac{5\left(\frac{L_2\omega_i}{u_f}\right)^2}{2+\left(\frac{L_2\omega_i}{u_f}\right)^2}\right], \tag{2.64}$$

describing the current per unit length (Am^{-1}) along the length of the probe parallel to the direction of flow. This is then multiplied by the width of the probe to get the current (A).

Thus the total current collected by the probe is give by

$$I_{total} = (I_{parallel} + I_{cl}\gamma) \times W, \qquad (A) \tag{2.65}$$

$$= (I_{parallel} + en_i u_B (L_2 - L_1)\gamma) \times W, \tag{2.66}$$

where W is the width (m) of the probe. In the event the total length of the probe L_2 is shorter than L_1 the contribution of I_{cl} should be dropped and $I_{parallel}$ integrated between 0 and $\left(\frac{L\omega_i}{u_f}\right)$.

2.6.2 Upstream Small Angle Condition

Figure 2.5: *Diagram illustrating the physical orientation of the probe's surface to the flow under the upstream small angle condition.*

Under the upstream small angle condition the probe is oriented so that the surface faces into the direction of flow (fig. 2.5). Thus the flow velocity u_f is split into the components

$$u_0 = u_f \times Sin\theta, \tag{2.67}$$

$$u_y = u_f \times Cos\theta, \tag{2.68}$$

where u_0 is directed normal to the surface and u_y parallel to the surface of the probe.

This initial flow velocity towards the surface of the probe has implications for the length over which J_{me} is valid. This can be estimated by solving equation (2.46) for L where $s_1 = 0$ which must be done numerically.

As $u_0 \neq 0$ but is positive, equation (2.62) takes the form

$$I_{upstream} = \frac{en_0u_y}{\omega_i}\left[s_0\omega_i\int_0^{\frac{L_2\omega_i}{u_y}}\frac{(z+z^3/12)dz}{(1+z_2/2)^2} - u_0\int_0^{\frac{L_2\omega_i}{u_f}}\frac{dz}{(1+z_2/2)^2}\right], \tag{2.69}$$

where $z = \omega_i\tau = \omega_i y/u_f$ and $I_{upstream}$ the current per unit length (Am^{-1}) in the direction of the surface of the probe. Which when integrated yields

$$I_{upstream} = \frac{en_0u_y}{\omega_i}\left[\omega_i s_0\left\{\frac{1}{6}ln(1+\alpha^2/2) - \frac{\alpha^2/12}{1+\alpha^2/2} - \frac{1}{1+\alpha^2/2} + 1\right\} - u_0\left\{\frac{\alpha^2/2}{1+\alpha^2/2} + \frac{1}{\sqrt{2}}\tan^{-1}\frac{\alpha}{\sqrt{2}}\right\}\right], \tag{2.70}$$

where the substitution $\alpha = L_2\omega_i/u_f$, giving the current per unit width (Am^{-1}) along the length of the probe. In many cases this can be approximated as

$$I_{upstream} \approx \frac{en_0u_y}{\omega_i}\left[\frac{\omega_i s_0}{6}\{ln(\alpha^2/2)+5\} + \frac{\pi u_0}{2\sqrt{2}}\right], \tag{2.71}$$

where the assumption $\alpha \gg 1$ can be made. The current per unit width can then be multiplied by the width of the probe to get the current (A).

Thus the total current collected by the probe is give by

$$I_{total} = (I_{upstream} + I_{cl} \times \gamma) \times W \tag{2.72}$$

$$= (I_{Upsream} + en_iu_x(L_2 - L_1)\gamma) \times W \tag{2.73}$$

where W is the width (m) of the probe and u_x is the greater of u_B or u_0. Again in the event the total length of the probe is shorter than L_1 the contribution of I_{cl} should be neglected and the limits of integration changed accordingly, though given the typical shortening in the length of validity for J_{me} this is unlikely to occur.

2.6.3 Downstream Small Angle Condition

Under the downstream small angle condition the probe is oriented so that its surface is in the shadow of the flow (fig. 2.6). Thus we have the rather unusual condition of the initial component of the flow velocity normal to the surface of the probe

$$u_0 \quad = \quad -u_f \times Sin\theta, \tag{2.74}$$

being directed away from it, while

$$u_y = u_f \times Cos\theta, \tag{2.75}$$

is still parallel to the surface in the direction of flow.

At the leading edge of the probe the plasma starts in contact with the probe. The ions then move away from the probe till the electric field slows them to the point where they are accelerated back towards the surface of the probe. This leads to an ion free zone along the leading section of the probe, which means a time delay before current begins to be collected and a reduced area of collection.

At angles near to parallel it can be assumed that this region is small in comparison to that of the matrix sheath that forms. Instead, rather than

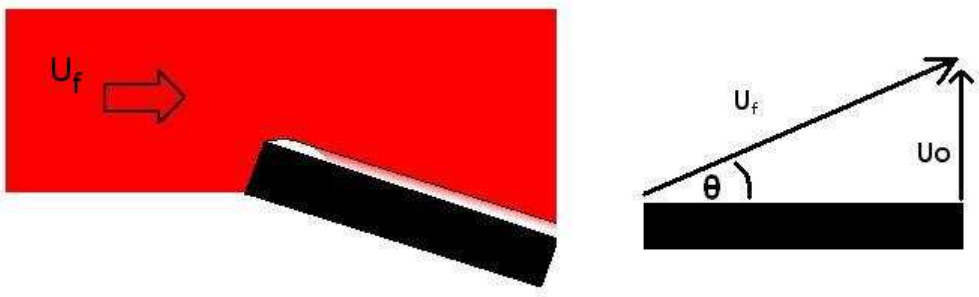

Figure 2.6: *Diagram illustrating the physical orientation of the probe's surface to the flow under the downstream small angle condition.*

explicitly taking its presence into account, we can integrate from the point where the ions drawn back by the electric field strike the probe. To this end we start with the expression (2.33) for the initial ion velocity u_0 to the surface

$$u_x(x,\tau) = \frac{\bar{n}}{n_0}\left[u_0 - \omega_i^2(s_0 - x)\tau - \frac{1}{12}s_0\omega_i^4\tau^3\right], \tag{2.33}$$

so

$$u_x(0,\tau) = \frac{\bar{n}}{n_0}\left[u_0 - \omega_i^2 s_0\tau - \frac{1}{12}s_0\omega_i^4\tau^3\right]. \tag{2.76}$$

By then integrating this expression we can find the displacement of the ion front from the surface of the probe so that

$$x(\tau) = \frac{\bar{n}}{n_0}\left[u_0\tau - \frac{1}{2}\omega_i^2 s_0\tau^2 - \frac{1}{48}s_0\omega_i^4\tau^4\right], \tag{2.77}$$

with the boundary condition of $x(\tau = 0) = 0$. The ion current will start to be collected when $x = 0$ at some point $\tau = L/u_y > 0$ along the probe. The solution to (2.77) that satisfies this condition is

$$(\omega_i\tau)^3 + 24(\omega_i\tau) - \frac{48u_0}{\omega_i s_0} = 0, \tag{2.78}$$

which has the unique real solution, given by

$$\omega_i\tau_0 \approx \frac{2u_0}{\omega_i s_0} \text{ for } \frac{u_0}{\omega_i s_0} \ll 1 \tag{2.79}$$

so that

$$\tau_0 \approx \frac{2u_0}{\omega_i^2 s_0} \tag{2.80}$$

Integrating from the point τ_0 the equation (2.62) takes the form

$$I_{downstream} = \frac{en_0u_y}{\omega_i}\left[s_0\omega_i\int_{\omega_i\tau_0}^{\frac{L\omega_i}{u_y}}\frac{(z + z^3/12)dz}{(1 + z_2/2)^2} - u_0\int_{\omega_i\tau_0}^{\frac{L\omega_i}{u_y}}\frac{dz}{(1 + z_2/2)^2}\right] \tag{2.81}$$

where $z = \omega_i\tau = \omega_i y/u_y$ and $I_{downstream}$ is the current per unit length (Am^{-1}) in the direction of the probe's surface, which making use of the substitution

$\alpha = L\omega_i/u_y$ and $\beta = \omega_i\tau_0 \approx 2u_0/\omega_i s_0$ gives

$$I_{downstream} = \frac{en_0u_y}{\omega_i}\left[\omega_i s_0\left\{\frac{1}{6}ln\left(\frac{1+\alpha^2/2}{1+\beta^2/2}\right) - \frac{\alpha^2/12}{1+\alpha^2/2} + \frac{\beta^2/12}{1+\beta^2/2} - \frac{1}{1+\alpha^2/2} + \frac{1}{1+\beta^2/2}\right\} - u_0\left\{\frac{\alpha/2}{1+\alpha^2/2} - \frac{\beta/2}{1+\beta^2/2} + \frac{1}{\sqrt{2}}\tan^{-1}\frac{\alpha}{\sqrt{2}} - \frac{1}{\sqrt{2}}\tan^{-1}\frac{\beta}{\sqrt{2}}\right\}\right]. \quad (2.82)$$

This can be approximated as

$$I_{downstream} \approx \frac{en_0u_y}{\omega_i}\left[\frac{\omega_i s_0}{6}\{ln(\alpha^2/2) + 53\beta^2\} - u_0\left\{\frac{\pi}{2\sqrt{2}} - \beta\right\}\right], \quad (2.83)$$

where the assumptions $\alpha \gg 1$ and $\beta \ll 1$ are valid. The current per unit width can then be multiplied by the width of the probe to get the current (A).

In the cases of interest it was found that the total length of the probe was generally less than L_1, so the total current collected by the probe is give by

$$I_{total} = I_{downstream} \times W \quad (2.84)$$

where W is the width (m) of the probe.

2.7 Mach Probe Applications

As explained earlier (section 1.2.2), the theory of Mach probes has been well developed for probes operating in magnetized plasmas. However, there is no suitable theory of which this author is aware for unmagnetized plasma. The theory presented here offers the ability to make an estimate of the flow velocity u_f for a planar probe in an unmagnetized plasma provided certain conditions are met.

Firstly it requires that the the orientation of the probe's surface with respect to the flow can be accurately estimated, which can prove problematic

depending on the experimental setup. Secondly, accurate estimates for the values of the plasma density n_0 and temperature T_e are required. This should be attainable either though theory or ideally an independent diagnostic technique.

With these two conditions met it is possible to then use the expressions for the ion current collected by the probe (2.66) to estimate the flow velocity, by fitting to experimental results over a range of probe bias'.

2.8 Discussion

This chapter set out to present the development of an analytical model for a negatively biased planar Langmuir probe within an unmagnetized plasma possessing a supersonic flow velocity ($u_f \gg u_B$). It has been shown that the PIII model of Riemann and Daube [45] for the current density of a non-flowing plasma at an electrode can, under the outlined conditions, be modified to described a plasma flowing past a planar probe. Expressions for the current density over the matrix extraction and sheath expansion phases are described. Expressions for the total ion current collected by a probe with its surface oriented parallel, upstream to, and downstream from the direction of flow are also presented. Finally a method by which the flow velocity can be estimated has been suggested.

CHAPTER 3

Hybrid Particle in Cell Code

3.1 Motivation

The initial computer modeling performed for the simulation work in this project was carried out using an existing standard 1D PIC and a 1D hybrid PIC codes. The standard PIC code used was a mature general code[1] needing no modification for the work, while the hybrid code needed further modification in the course of the early part of the project to allow the injection of ions for small angle work and the testing of assumptions about warm ions.

The results of the 1D hybrid work then provided data against which to test the early analytical work and later validate the behaviour of the 2D hybrid code. In addition, lessons learned in making the necessary adaption were then integrated into its design and structure.

[1]EN Code, Prof. Miles Turner, e-mail:miles.turner@dcu.ie

Just as the analytical model does, the initial 1D work tracked the evolution in time of a slice of plasma in contact with a planar electrode. This was then related to the plasma evolution along the length of the probe's surface. However the 1D treatment lacked the ability to replicate the effect that the leading and trailing edges of the probe would have on the current collected by the probe. For this reason it was necessary to construct a 2D code describing the plasma flow. The code was constructed so that the probe would be imbedded within the grid to fully study edge effects.

3.2 Standard 1D Code

The existing 1D PIC code that was first used contained both particle ions and electrons, configured for an electrostatic simulation of an initially homogenous plasma in contact with a planar electrode. The left side wall of the simulation was a periodic boundary with a zero potential representing the bulk from which plasma could be injected with constant density and velocity, while the right side wall was fully absorbing and had a negative bias applied to it. The results obtained gave insight into the system however the null rise time and an artificially-fixed, zero-potential boundary condition on the bulk side of the simulation caused undesirable effects in the electron behaviour.

When the simulation started the null rise time in probe bias caused electrons to be rapidly repelled from the probe in a electron shockwave [64] as a sheath formed. Upon reaching the left hand side with its fixed potential the shockwave was reflected back towards the probe, where it was again reflected continuing to oscillate back and forth. This in turn affects the ion current (fig. 3.1) causing an increase in the initial ion current early on and then an oscillation in the later current collection.

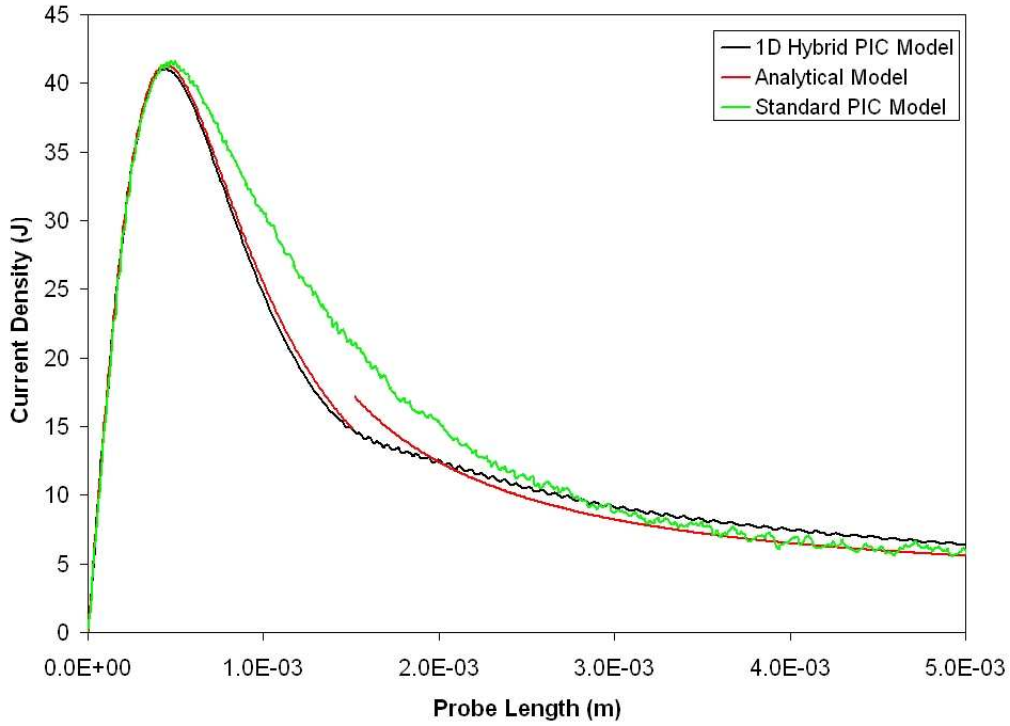

Figure 3.1: *Graph of comparison between full PIC, hybrid PIC and analytical model showing current density (A/m^2) along a probe's length angled parallel to the direction of flow. Probe bias $-32V$, $u_f = 1.7^4$, $n_0 = 7 \times 10^{16} m^{-3}$, $\mathrm{T}_e = 0.22eV$.*

This electron shock wave phenomenon occurs when rise times in probe bias are less than the electron plasma period ($2\pi/\omega_{pe}$) [64]. In the case of a flowing plasma, as the plasma approaches the probe it is aware of the presence of the potential and so there is a finite rise time. In the plasma considered, this time should exceed that required for an electron shock wave to form[2] yet not invalidate the assumptions of the analytical model[3]. To remove this artificially induced shock wave and the effects of the resultant oscillation of the electrons on the ion motion the move to a 1D hybrid model was made. In addition this also had the added advantage of faster run times as only the particle ions now needed to be tracked allowing a larger time step to be selected. In the subsequent move to two dimensions, these computational savings were particularly significant.

3.3 1D Hybrid Code

The existing code was a standard hybrid code, in which the ions were represented as particles and the electrons were treated as a Boltzmann fluid. One side of the simulation was set to a zero potential while the other was user defined. The simulation space could be loaded with a single species of particles of set physical characteristics and a homogeneous distribution. Finally the boundary walls were absorbing.

Two main modifications had to be made to the code. The first was the addition of particle injection in order to allow for the inclusion of particles with an initial directed velocity. This allowed for the simulation of the probe oriented at angles both upstream and downstream depending on whether the

[2]This condition should be kept in mind when applying hybrid codes to a plasma as while it will eliminate the effect of the electron shockwave it could in fact be a real effect.

[3]See chapter 2,section 2.2.

initial drift velocity was set to be positive or negative. To this end a simpler one dimensional version of the injection method detailed in section 3.4.4 was implemented. The second was the adaption made to allow for the inclusion of an initial thermal ion velocity.

3.3.1 Cold Ion Assumption

Both the analytical model and hybrid codes make the assumption that the thermal velocity of the ions can be neglected ($T_i \ll T_e$). In order to test this assumption the 1D hybrid code was adapted to allow the simulation of ions with a thermal velocity,

$$u_{th} = \sqrt{\left(\frac{k\mathbf{T}_i}{m_i}\right)}. \tag{3.1}$$

To achieve this the ions were loaded with a Maxwellian distribution of thermal velocities, divided evenly between the two degrees of freedom. The distribution was generated from a series of random numbers using the method described in 'Seminumerical Algorithms' [65]. Each particle's velocity was then modified so that the overall distribution is Maxwellian.

Simply loading the particles into the simulation with the appropriate spread of thermal velocities is insufficient. This is because while the overall distribution may be Maxwellian but the distribution within any give cell could be very different [55].

To ensure a Maxwellian distribution both globally and locally within the simulation, firstly the initial number of particles needed to be greatly increased beyond that needed for the cold ion condition. Secondly, and vitally, the *Quiet Start* method outlined by Birdsall and Langdon [55] was also implemented. This involved the particles being initially loaded with thermal velocities according to the Maxwellian distribution. The position of the par-

ticles within the cells is then scrambled using a bit reversal algorithm (figure 3.2) before being assigned to cells.

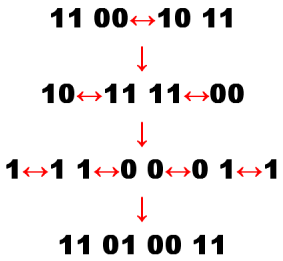

Figure 3.2: *An example of the operations carried out using binary operators and masks by the bit reversal algorithm (http://www.aggregate.org/MAGIC/) on the index of the array. The array elements were then moved to the new positions, scrabbling the contents of the array.*

This adapted code was then run with varying densities and potentials for a variety of thermal ion velocities. Even at average thermal velocities of up to twice the Bohm velocity the current collected during the early matrix extraction phase and the later sheath expansion phase are not seriously disturbed (figure 3.3). There is however a small initial current collected due to the initial thermal drift velocity towards the probe.

3.4 2D Hybrid Structure

The two dimensional code I wrote to meet the needs of this project is a collisionless electrostatic hybrid model. The ions are representative of a single species of cold, singly charged ions while the electrons are represented by a fluid in Boltzmann equilibrium with the potential on the grid. The local number density n_e is described by the simplified Boltzmann relation

$$n_e = n_0 \, exp \, \frac{e\Phi}{k_B T_e}, \tag{3.2}$$

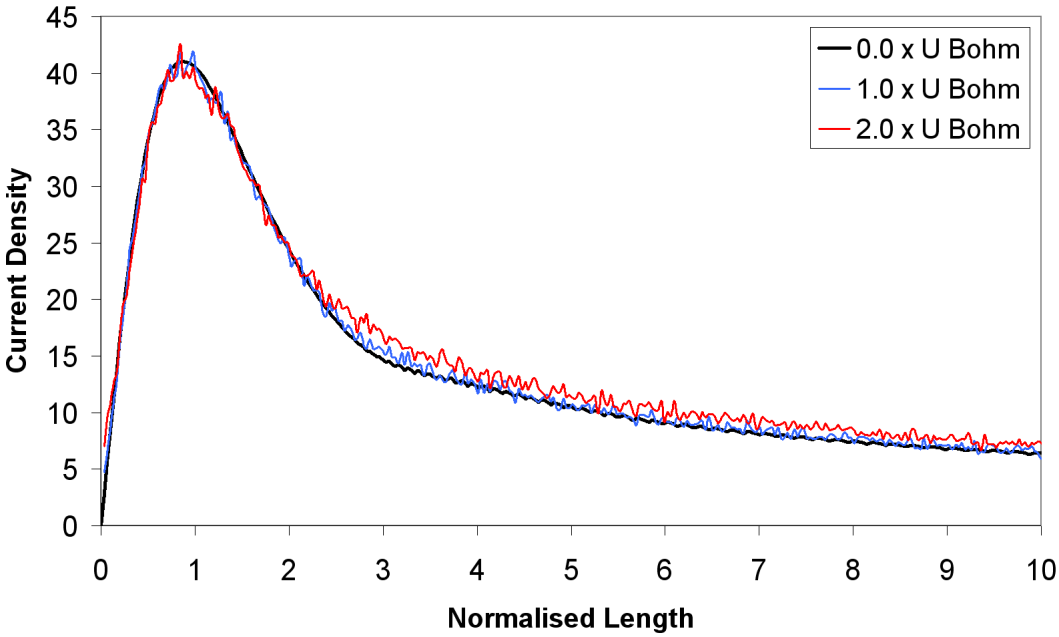

Figure 3.3: *Graph of current density* (A/m^2) *along the normalized probe length* $(\omega_i L/u_f)$ *oriented parallel to the direction of flow for a range of thermal velocities.* $V_0 = -32\,V$; $T_e = 0.22\,eV$; $n_0 = 7 \times 10^{16}\,m^{-3}$; $m_i = 1.79 \times 10^{-25}\,kg$

where n_0 is the plasma particle number density, T_e is the electron temperature and Φ the local potential.

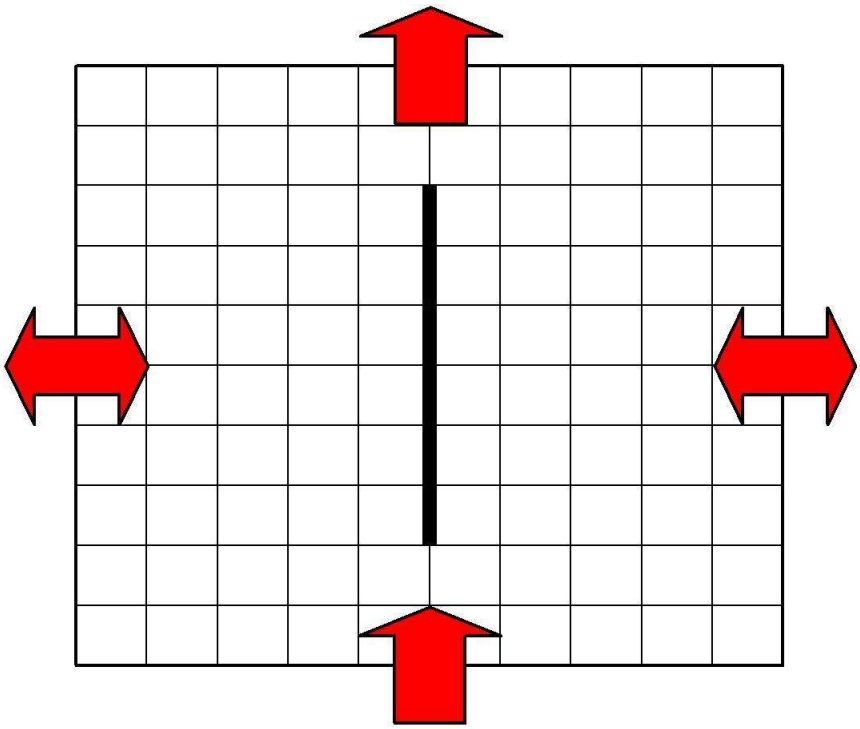

Figure 3.4: *Diagram of the grid structure, boundary conditions and probe location (centre) for the 2D hybrid code. Typical grids ranged from 300-600 cells a side.*

In figure 3.4 the grid structure implemented by the code is illustrated. The grid is made up of cells of equal length along each side, chosen to be small enough to allow phenomenon of interest to be resolved. The choice of cell size is also constrained by the stability conditions which we discuss later (section 3.4.5). The probe itself (thick black line) is embedded within the grid along a line of cell boundaries and separated from the edges of the simulation.

The particle boundary conditions along the sides of the simulation are periodic, meaning that a particle leaving one side re-enters from the other. The

upper boundary is a perfectly absorbing wall and any particles that strike the wall are removed from the simulation. Particles crossing the cell boundaries occupied by the probe are likewise removed and they contribute to the flux recorded for the relevant side of the probe. To allow for the simulation of a plasma flow, particles can be injected along the lower boundary with the required velocities and density.

3.4.1 Weighting Techniques

For the obvious reason of computational cost it is not feasible to simulate the behaviour of every particle within a plasma. Instead so called super particles are used [55, 56]. In the case of the 2D code presented here typically 10^7 super particles take the place of anywhere from 10^{14} to 10^{24} real particles depending on the nature of the plasma to be investigated. In order to achieve realistic behaviour and valid results all of the relevant physical quantities must be scaled using an appropriate weighting scheme within the PIC code. There are two groups of operations where such scalings are used.

The first is the allocation of physical quantities such as density from the particles to the grid and the reverse operation of applying the force from the calculated electric field back onto the particle (grid weighting). The second is the weighting of the physical quantities of the plasma particles to the super particles in proportion to the number of real particles each one represents (particle weighting).

In the case of *grid weighting* the standard first order bilinear interpolation for two dimensions [55] has been implemented in this code. For example in assigning the density of the super particle in figure 3.5 to the grid the density is divided up between the four grid nodes enclosing the cell within which it resides. This is carried out according to the equation set (3.3→3.6) where a

percentage of the particle's total ion density δ_i is distributed to each node according to its relative distance from the particle.

$$\delta_{j,k} = \delta_i \frac{(\Delta x - x)(\Delta y - y)}{\Delta x \Delta y}, \tag{3.3}$$

$$\delta_{j+1,k} = \delta_i \frac{x(\Delta y - y)}{\Delta x \Delta y}, \tag{3.4}$$

$$\delta_{j+1,k+1} = \delta_i \frac{xy}{\Delta x \Delta y}, \tag{3.5}$$

$$\delta_{j,k+1} = \delta_i \frac{(\Delta x - x)y}{\Delta x \Delta y}, \tag{3.6}$$

where $\delta_{j,k}$ is the fraction of the density assigned to the relevant nodes, x, y mark the coordinates of the particle within the cell and $\Delta x, \Delta y$ are the dimensions of the cells.

This grid weighting scheme smooths out the noise on the grid as the par-

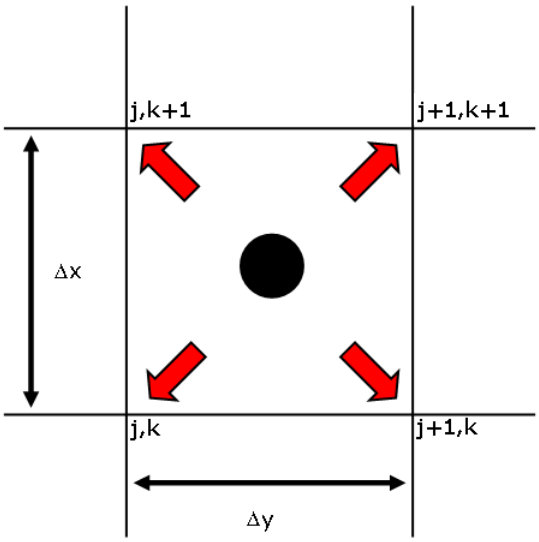

Figure 3.5: *Diagram of a cell within a two dimensional square grid with x,y coordinates. The particle's charge is divided evening between the four nearest grid points using a weighting scheme.*

ticles travel across it, if for example a zero-order weighting such as (NGP[4]) was to be used the total density of the particle would jump suddenly from node to node. Instead with the first-order scheme the density smoothly flows across the nodes of the grid. While higher order weightings can be implemented, the additional smoothing is seldom worth the added computational costs incurred [57].

In the second case of *particle weighting* each super particle represents a large population of real physical particles. This necessitates the scaling of the physical properties to ensure an accurate physical representation. The field solver used with this code deals with normalized values for reasons of computational ease and efficiency (section 3.4.2). The weighting used scales both by cell size and the ratio of real to super particles as follows

$$system\,length\,in\,\alpha = \Delta\alpha \times nc_\alpha, \tag{3.7}$$

$$np_0 \times weighting = n_0 \times nc_x \times nc_y, \tag{3.8}$$

where α is the relevant axis, nc_α is the number of cells and np_0 initial number of super particles loaded in simulation.

The initial number of particles (np_0) loaded into the simulation is calculated from the number of particles loaded per cell times the initial number of cells to be filled. Higher numbers of particles per cell lowers computational noise while increasing the computational cost. The choice of 100 super particles per cell has been suggested [66] as an acceptable compromise between cost and accuracy, though when examining the current to the probe it can require up to 256 particles per cell to satisfactorily reduce noise.

[4]Nearest Grid Point, where a particles total density is assigned to its nearest grid point.

Time Varying Plasma Flow Density

Certain flowing plasmas of interest, such as laser produced plasma plumes, possess a time varying density. This density can vary by several orders of magnitude as the plume passes the probe [31]. Keeping the particle weighting constant and lowering the number of super particles injected is impractical. Not only would an unfeasibly large number of particles per cell be required at peak flow to allow viable numbers a lower flow, but the problems of smoothly distributing the varying numbers on injection would be nontrivial.

Instead it was hoped the particle weighting could be varied in time as the particles are injected into the grid, which should allow for the simple treatment of a beam with time varying density for the minor additional computational cost of tracking the weight of each particle. Unfortunately the field solver makes use of a scaling parameter (eqn. 3.9) detailed in the next section, which is dependent on the Debye length. This is of course dependent on the plasma density n_0. As the density would not be constant this scaling parameter becomes useless. Implementing this would require the writing of an entirely new field solver, a task beyond the time available to complete the work.

3.4.2 Field Solver

This code utilizes a two stage field solver written by Prof. Miles Turner which is described below.

The field solver calculates the potential ψ on the grid as well as the electric fields E_x, E_y all in normalized units. The inputs taken by the solver are the normalized density on the grid and the scaling parameter

$$\gamma^2 = \frac{\Delta x^2}{\lambda_D^2}, \tag{3.9}$$

where Δx is the cell size and λ_D the Debye length.

To calculate the electric fields the solution to Possions equation

$$\nabla^2 \Phi = -\frac{\rho}{\epsilon_0}, \tag{3.10}$$

must be found, for which the electron and ion densities are required.

The ion densities are tracked by particles and their densities assigned to the grid. As this is a hybrid code the electron density is described by a Boltzmann fluid rather than particles. Thus local density of the electrons is found using the Boltzmann relation (3.2). So the charge density ρ becomes

$$\rho = e(n_i - n_e) = e\left(n_i - exp\left(\frac{e\Phi}{k_B T_e}\right)\right). \tag{3.11}$$

The potential is normalized using

$$\psi = \frac{e\Phi}{k_B T_e}. \tag{3.12}$$

These are then combined into the following finite difference equation

$$\psi_{i+1,j} + \psi_{i-1,j} + \psi_{i,j+1} + \psi_{i,j-1} - 4\psi_{i,j} = -\left(\frac{\Delta x}{\lambda_D}\right)^2 (\eta - exp(\psi_{i,j})), \tag{3.13}$$

where $\eta = n_i/n_0$ is the normalized ion density. The presence of the exponential term in equation (3.13) indicates a nonlinear system.

For the first stage, the solver takes inputs of the normalized ion density (η) across the grid and scaling parameter (3.9). The code then solves the difference equation (3.13) using the Newton-Raphson method.

In the second stage the resulting linear system from the first stage is then solved using an alternating direction implicit method (ADI). This method functions by first solving along a row, then a column and then a row again, *alternating* back and forth as it goes. For example consider a 3×3 grid with nodes numbered 1-9 in rows. An ADI method would solve along 123 then 147 then 456 and so on . This process is then repeated till it converges on a satisfactory solution [67].

3.4.3 Particle Pusher

Using the E_x and E_y components of the electric field calculated by the field solver, the acceleration on a charge due to the Lorentz force is calculated

$$\mathbf{F} = q\mathbf{E}. \tag{3.14}$$

To do this first the electric field is un-normalized as follows

$$\mathbf{E}_{real} = \mathbf{E}_{norm}\frac{k_B T_e}{e\Delta x}. \tag{3.15}$$

The acceleration can then be found using the Lorentz force (3.14) neglecting the magnetic component to give

$$\mathbf{a} = \frac{q\mathbf{E}_{real}}{m_i}. \tag{3.16}$$

The acceleration is then applied back onto the particle using the same grid weighting scheme as before. The particle's velocity components are then updated in x and y before it is finally moved to its new position.

3.4.4 Particle Injection

To model the plasma flow though the simulation space it is necessary to smoothly inject a continuous stream of plasma. The injection method used must be able to replicate the physical parameters of the plasma stream such as the component velocities ($u_x,\ u_y$) of the flow (u_f) and the density n_0. In the case of the plasma flow directed parallel to the long axis of the probe, the particles are simply injected with the velocity $u_y = u_f$.

For the near parallel case particles need to be injected with different velocity components in the x and y direction. This allows the simulation of flows at a range of angles to the surface of the probe, though care must be

exercised to ensure that a wide enough grid is chosen to prevent disturbances propagating across the periodic side boundaries (figure 3.4).

Initially the particles are appropriately distributed across the cells (typically homogenously across the first number of rows) and physical characteristics are assigned. With each time step the particles advance some distance dependant on the flow velocity and step size. The new empty area at the leading edge of the simulation is then filled. Care must be taken in ensuring that there is no discontinuity in the distribution between the injected plasma and the trailing edge of the existing particles. In this way a smooth flow of particles into the simulation is maintained.

3.4.5 Stability Conditions

In order to be confident of the results of the simulation, steps need to be taken to ensure stability, because of the use of finite difference equations. In the case of electrostatic PIC simulations two general stability conditions need to be obeyed. These enforce limits on the choice of cell size and time step. It should also be remembered that stability does not necessarily ensure the accuracy of the results [56, 57]. Thus these conditions need to be restrained further yielding

$$\omega_{pi}\Delta t < 0.2, \tag{3.17}$$

$$\frac{\Delta x}{\lambda_D} \leq 1. \tag{3.18}$$

The first condition (3.17) ensures the stability of the leap frog method used to advance the motion of the particles in time. As it is the ion motion that is of interest, the time step Δt is chosen to follow the minimum oscillation of ions (i.e. the ion plasma frequency ω_{pi}). The limit of < 2 ensures stability, while < 0.2 is required for accuracy [56, 57]. A different formula-

tion of this condition on the time step has been presented by A. Meige in his hybrid PIC model [68].

The second condition (3.18) is concerned with the length scale over which the mesh can resolve physical structures within the plasma. The characteristic length scale within a plasma is defined by the Debye length λ_D. In order to resolve structures such as sheaths within the plasma a cell size Δx less than this length must be chosen.

As the plasma being simulated is fast flowing there is an additional time of flight stability condition. The Courant-Friedrich-Lewy (CFL) condition [55, 56] is used,

$$\frac{u_f \Delta t}{\Delta x} << 1. \tag{3.19}$$

This additional condition ensures that particles do not cross more than a single cell during any give time step. It should be noted that the velocity of particles crossing the sheath can exceed twice the Bohm velocity u_B [62, 63]. Thus in cases where the Bohm velocity is not insignificant when compared to the flow velocity extra care must be taken to ensure the CFL condition is met within the sheath.

3.5 Discussion

In this chapter the different particle in cell (PIC) codes used have been described. The reasons for the move from full particle in cell codes to hybrid codes has been explained. In the case of the existing one dimensional hybrid code all changes made and its use in testing the validity of the cold ion assumption have been detailed. The structure and behaviour of the two dimensional electrostatic hybrid particle in cell code has also been described.

3.5 Discussion

The stability conditions under which it must be used to ensure accurate results and their reasons have also been described.

CHAPTER 4

Comparison of Analytical and Particle in Cell Models

Reliable numerical simulations provide an excellent method for testing the accuracy of an analytical model. To this end, the 2D hybrid code is compared against the 1D hybrid code to consider the impact of edge effects on the plasma's interaction with the probe. The ability of the analytical model to describe the current density and total probe current is also compared against the 2D numerical simulations over a range of plasma flow velocities.

The 2D code has the ability to resolve the sheath's behaviour at the probe's edge, particularly around the leading edge of the probe. This provides the chance to test the model's assumption of an initial matrix sheath and its expansion towards a Child-Law like sheath. Both moderate and highly supersonic speeds over a range of probe orientations are investigated.

Finally the source of the experimentally observed square root dependence of the currents on probe bias and the analytical model's ability to describe

it are considered.

4.1 1D and 2D PIC Comparisons

The 1D hybrid code, like the analytical model, equates the evolution of a plasma in time to its evolution along the probe's length (fig. 2.2b). This prevents the consideration of any inherently two dimensional phenomena such as those surrounding the leading edge of the probe.

While the 1D code could in theory use inhomogeneous starting distributions these would have to be assumed rather than evolving naturally. The analytical model does not have this option as it depends on the assumption of a homogenous plasma upstream of the probe.

The 2D hybrid code was written in order to allow the simulation to resolve these effects, in particular the sheath formation at the leading edge of the probe, which has two important implications. The first is that rise time of the potential is a deciding factor in the formation of an electron shock-wave (section. 3.2). Secondly how far it propagates ahead of the probe has implications for the validity of the analytical model's assumptions.

To investigate the difference between the two simulations, both codes were run for a highly supersonic (mach 38) and moderately supersonic (mach 5) plasma flow. A $3mm$ probe with an applied bias of $-30V$ was used in all cases. Three different orientations relative to the direction of flow, parallel, 5° degrees upstream and downstream were considered.

In each case, the density profiles along the length of the probe for the 1D and 2D simulations were compared. The percentage by which the 2D results differed from the 1D results was measured and the results graphed.

High Mach Flow (Mach 38)

For a highly supersonic flow of $u_f = 1.7 \times 10^4 ms^{-1}$ the differences were relatively modest (fig. 4.1), typically less than 7%. From the 2D simulations the rise time of the potential ahead of the probe was typically found to be $9.7 \times 10^{-9} s$ which is greater than the electron plasma period ($2\pi/\omega_{pe}$). This means that no electron shock wave of the type seen in the full 1D particle simulation (section 3.2) should occur [64], indicating that the decision to move to a hybrid code was valid.

For all three orientations, the 1D code consistently overestimated and then underestimated the ion density over the leading section of the probe. This is due to 2D code's ability to resolve the effect of the probe's potential extending beyond the leading edge of the plasma (fig. 4.2a). The ions will have already started to react to the probe's presence ahead of its leading edge (fig. 4.2b), by the time they reach the probe.

Where the probe was oriented with its surface downstream to the direction of flow (fig. 4.1b) the 1D simulation formed an ion free region just in front of the probe. In the 2D simulation the expected delay in the collection of current is observed, but instead of a ion free region an slight increase in density is observed.

Low Mach Flow (Mach 5)

For the moderately supersonic case $u_f = 2.21 \times 10^3 ms^{-1}$ the same general structures are observed for all three orientations, except on a larger scale (fig. 4.3). Like the highly supersonic flow the rise time of the potential ahead of the probe is typically $8.3 \times 10^{-8} s$, and again greater than the electron plasma period ($2\pi/\omega_{pe}$).

In the highly supersonic flow the matrix extraction phase covered almost

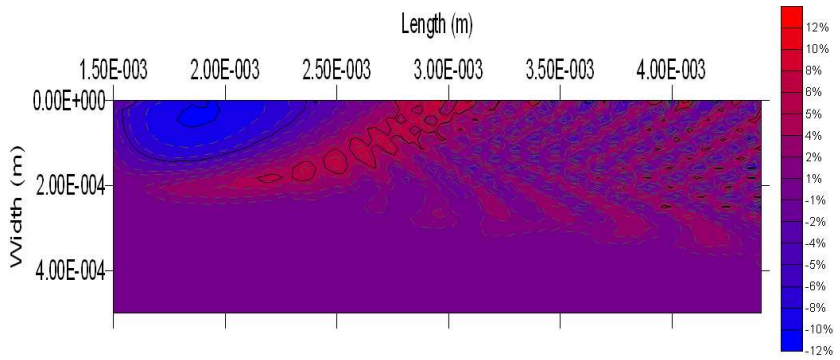

(a) Parallel

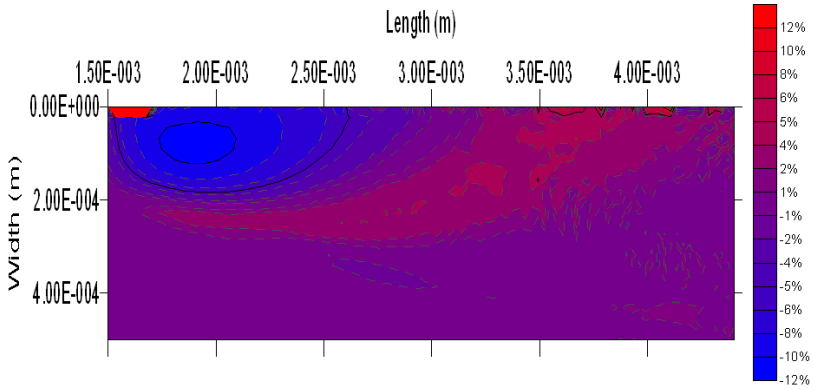

(b) Downstream 5° angle

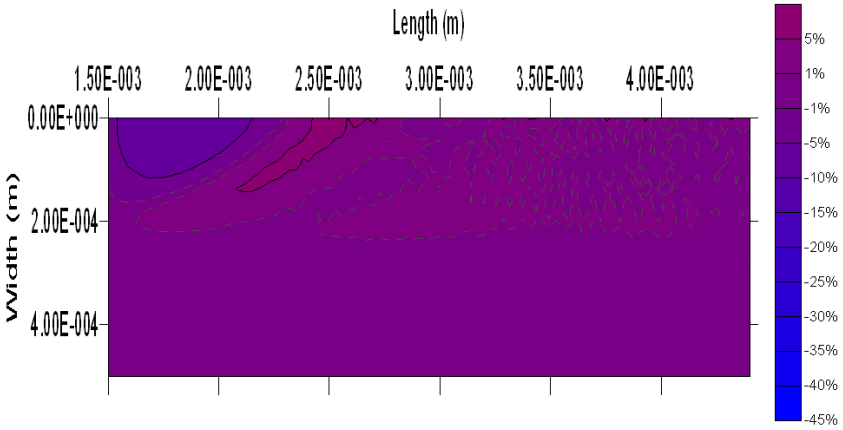

(c) Upstream 5° angle

Figure 4.1: *Graphs of the percentage difference in ion density between the 1D and 2D hybrid PIC simulation of a highly supersonic plasma flow along the length of a 3mm probe located at 1.5mm. Plasma parameters:* $u_f = 1.7 \times 10^4 ms^{-1}$, $u_B = 443.7 ms^{-1}$, $n_i = 7 \times 10^{16} m^{-3}$, $m_i = 1.79 \times 10^{-25} kg$, $T_e = 0.22eV$, $V_0 = -30V$.

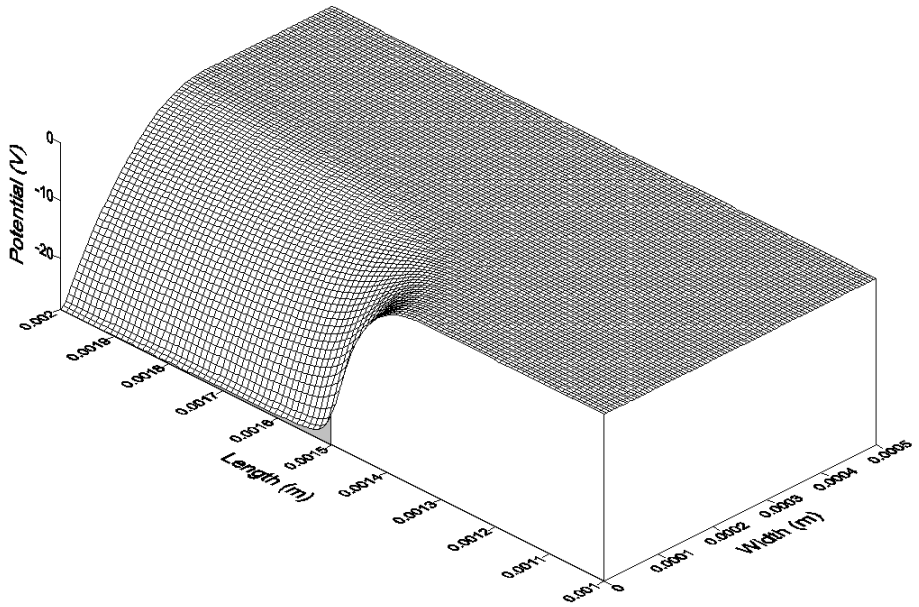

(a) Potential Profile

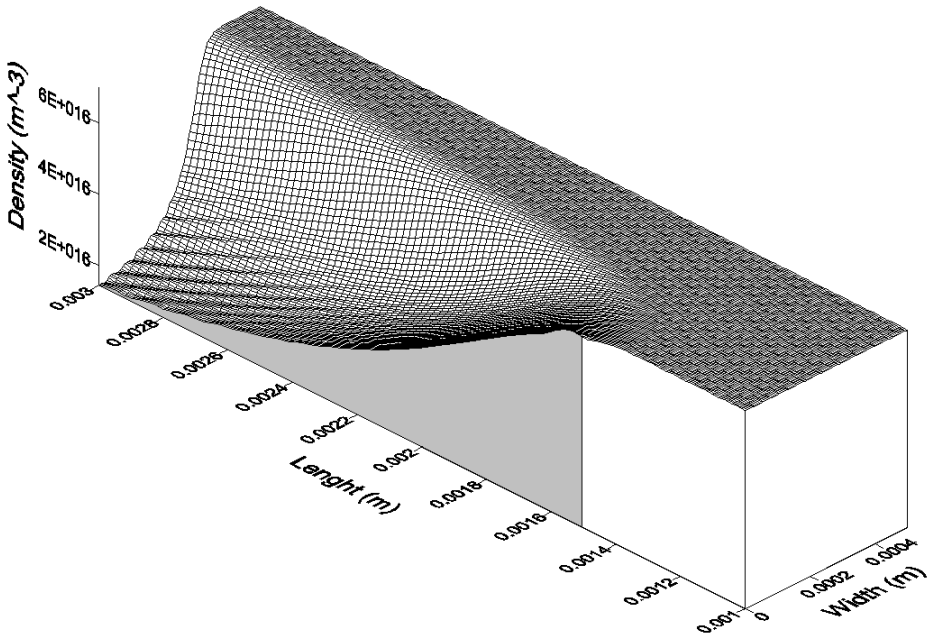

(b) Density Profile

Figure 4.2: *Graphs of the density and potential surrounding the leading edge of the* $3mm$ *probe located at* $1.5mm$ *and orientated parallel to the direction of flow. Plasma parameters:* $u_f = 1.7 \times 10^4 ms^{-1}$, $u_B = 443.7 ms^{-1}$, $n_i = 7 \times 10^{16} m^{-3}$, $m_i = 1.79 \times 10^{-25} kg$, $T_e = 0.22eV$, $V_0 = -30V$

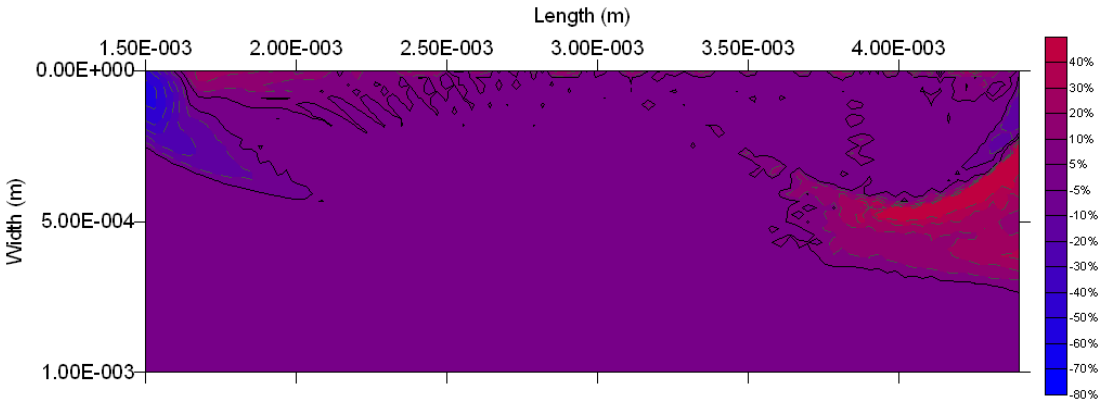

(a) Parallel

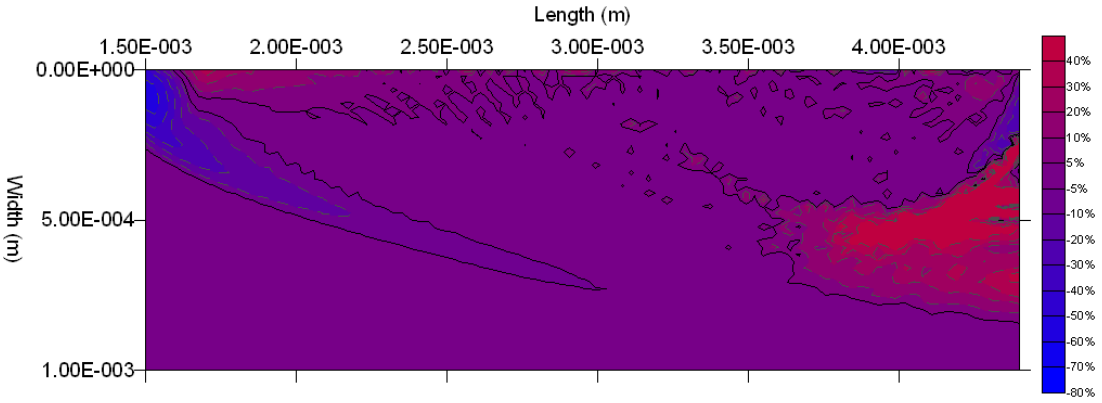

(b) Downstream 5° angle

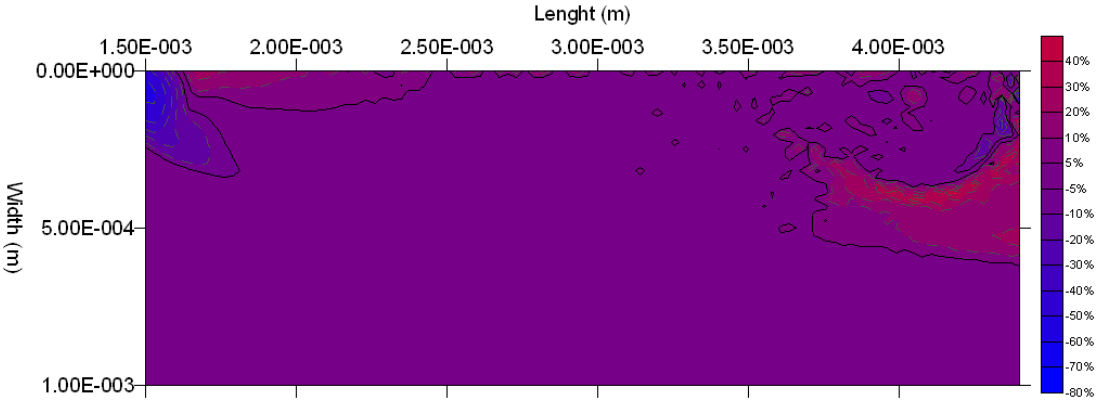

(c) Upstream 5° angle

Figure 4.3: *Graphs of the percentage difference in ion density between the 1D and 2D hybrid PIC simulation of a supersonic plasma flow along the length of a* $3mm$ *probe located at* $1.5mm$*. Plasma parameters:* $u_f = 2.21 \times 10^3 ms^{-1}$, $u_B = 443.7 ms^{-1}$, $n_i = 7 \times 10^{16} m^{-3}$, $m_i = 1.79 \times 10^{-25} kg$, $T_e = 0.22 eV$, $V_0 = -30V$.

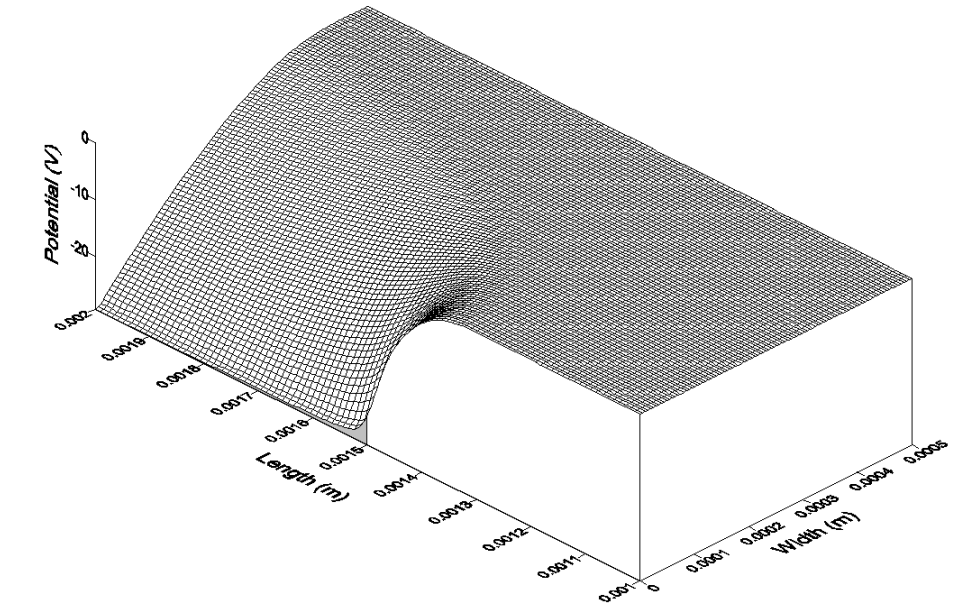

(a) Potential Profile

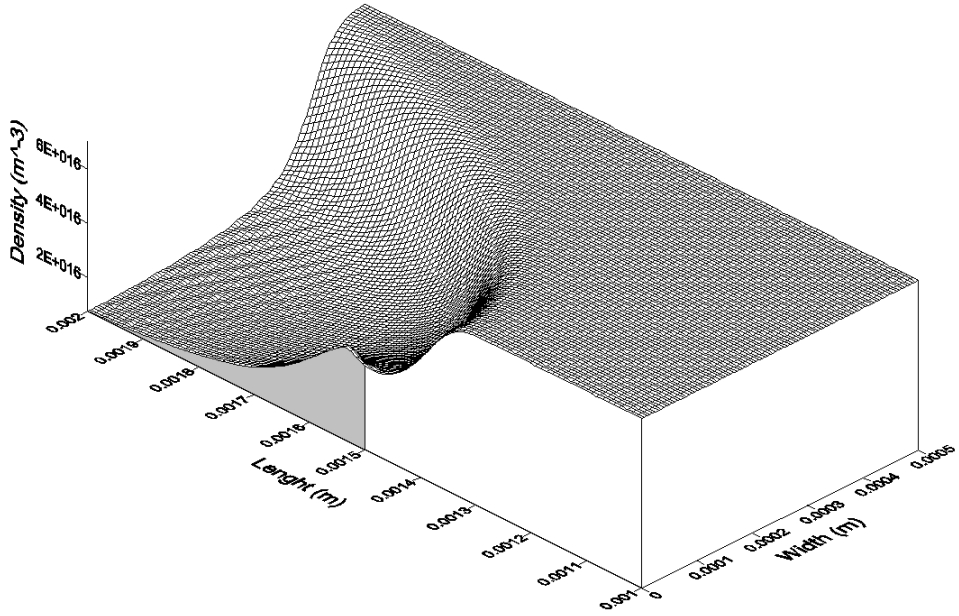

(b) Density Profile

Figure 4.4: *Graphs of the density and potential surrounding the leading edge of the* $3mm$ *probe located at* $1.5mm$ *and orientated parallel to the direction of flow. Plasma parameters:* $u_f = 2.21 \times 10^3 ms^{-1}$, $u_B = 443.7 ms^{-1}$, $n_i = 7 \times 10^{16} m^{-3}$, $m_i = 1.79 \times 10^{-25} kg$, $T_e = 0.22eV$, $V_0 = -30V$.

half the probe's $3mm$ length while for this case it accounts for just 7% of the probe's length. The unusual structures observed at the tail of the probe are caused by ions reflected back towards the probe by the fixed zero boundary condition on the grid. It should be noted that the use of percentage difference in these graphs greatly exaggerates the perceived size of these structures. The same effect is responsible for the structure's seen in figures 4.6b and 4.9b.

As the flow speed approaches the ion sound speed the probe disturbance upstream of the probe becomes less compressed. The probe potential (fig. 4.4a) and the disturbance to the ion density (fig. 4.4b) propagating further upstream of the probe raised concern over the analytical model's assumption of a homogenous ion density. Yet as the assumption became less valid the agreement between the total ion current to the probe from the analytical model and hybrid simulation was found to be similar over a range of flow velocities (table 4.1).

4.2 Comparison of analytical model and 2D simulations

The analytical model aims to describe the total current collected for three distinct probe orientations: parallel (section 2.6.1), upstream (section 2.6.2) and downstream (section 2.6.3), for each of which the theory attempts to predict the total ion current collected by a Langmuir probe in a plasma with supersonic flow.

The comparison between the 1D and 2D simulations demonstrates the scale of the edge effects present and how they are affected by the velocity of the plasma flow. At lower flow velocities the disturbance to the flow upstream of the probe was found to become more pronounced and propagate further

$u_f(ms^{-1})$	Mach	I Analytical (Am^{-1})	I Hybrid PIC (Am^{-1})	% Diff
1.7×10^4	38	5.64×10^{-2}	5.60×10^{-2}	+0.7%
8.87×10^3	20	3.84×10^{-2}	3.92×10^{-2}	-2.1%
4.43×10^3	10	2.57×10^{-2}	2.64×10^{-2}	-2.7%
2.21×10^3	5	1.77×10^{-2}	1.80×10^{-2}	-1.7%

Table 4.1: *Comparison of total ion current at various flow speeds for a probes surface aligned parallel to the flow and biased at $-30V$ as predicted by the analytical model and 2D hybrid code, alongside the percentage difference between the two.*

than at higher velocities where the entire sheath was seen to be compressed.

The analytical model's assumptions match the initial conditions of the 1D code almost exactly. It is likewise unable to account for the edge effects seen in the 2D model. Determining the model's assumption's divergence from the system and its resilience to this divergence is important. In order to assess the impact on the accuracy of the model the results for a variety of flow velocities at each orientation were considered.

The behaviour for a range of plasma density, electron temperature and probe biases were also considered, over the ranges of plasma densities (10^{15} to 10^{16} m^{-3}) and electron temperatures (0.22 to 1 eV) from the experimental results considered (chapter 5) and reasonable agreement between the analytical model and 2D simulations was observed. Within the ion saturation region where the probe bias was sufficiently negative to prevent electrons from reaching the probe, reasonable agreement was again observed.

4.2.1 Parallel 0° Degree Angle

The best agreement between the analytical model and the 2D simulations is observed with the probe's surface orientated parallel to the direction of flow. Table 4.1 presents the total ion current predicted by the analytical model and the results of the 2D hybrid simulation for a range of flow velocities. In each case the two sets of results were found to be in close agreement over the full range of flow velocity.

The sheath edge is defined to correspond to the point where the ion velocity toward the probe matches the ion sound speed ($u_x = u_B$) [4]. The position where this occurred in the 2D simulation was compared against the position predicted by an adapted version of the Riemann expression [45] for sheath width (fig. 4.6). The adapted expression (Appendix B, eqn. B.7) allows for the use of an arbitrary initial velocity u_0 normal to the probe surface u_x to represent this component of the flow velocity.

In the case of the highly supersonic flow the initial sheath width falls short of the predicted matrix sheath width (eqn. 4.2) due to the compression caused by the high velocity. As the flow velocity drops, the agreement in the sheath width at the leading edge of the probe improves as the disturbance upstream of the plasma expands. The distance along the probe for the matrix extraction phase exists(fig 4.6 *green line*) was also noted to be dependant on the flow velocity, accounting for the correlation between a greater length of the probe and a higher velocity.

Comparing the current densities along the probe for the two flow rates (fig. 4.7), the higher flow rate was found to produce a better agreement between the analytical model and the 2D simulations. The actual peak current at the probe is higher ($\sim 37.5 Am^{-2}$) than shown (fig. 4.7a) as the results from one

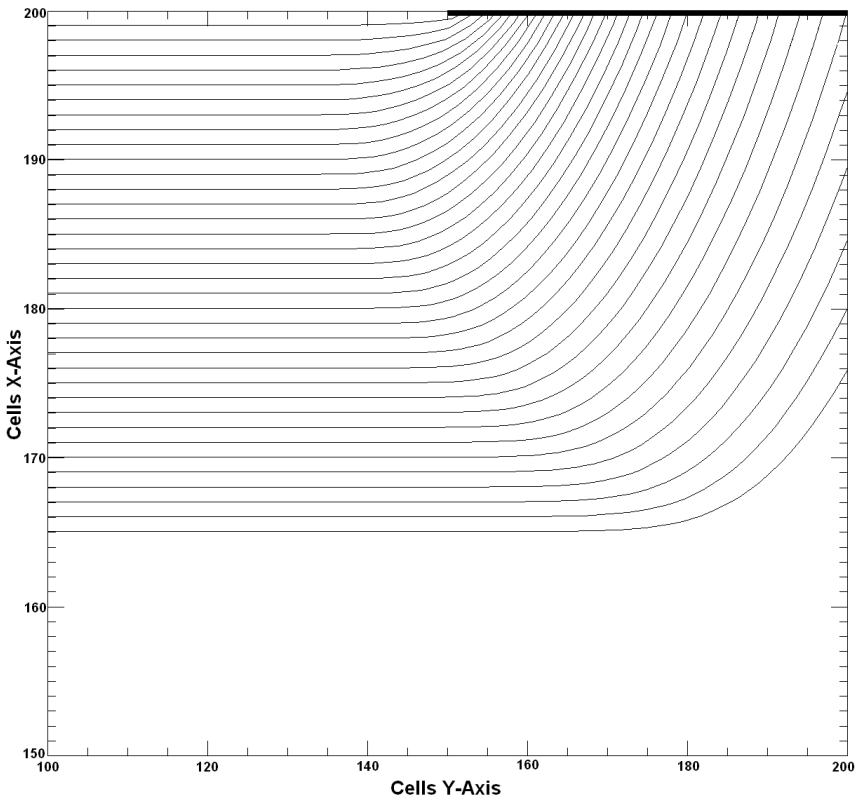

Figure 4.5: *Diagram of the flight paths of ions around the leading edge (150,200) of a probe orientated parallel to the direction of flow. Plasma parameters:* $u_f = 2.21 \times 10^{-3} ms^{-1}$, $n_i = 7 \times 10^{16} m^{-3}$,$V_0 = -30V$.

cell out from the probe's surface were used due to noise[1].

In the case of lower flow rates the agreement became progressively worse, in particular over the matrix extraction phase which had been assumed to be the most accurate. The reason for the disagreement appears to stem from the sheath extending ahead of the probe (fig. 4.6b). However, as pointed out earlier, the agreement between the total ion current predicted by the analytical model and the simulation remained close.

[1]Whole super particles striking the probe are removed from the simulation, causing the current density at the surface to vary in chunks rather than smoothly.

In order try to understand why the agreement did not drop at lower Mach numbers, the results of the 2D code were used to map the ion flight paths around the leading edge of the probe. It was found that for high Mach number where the homogenous assumption is better satisfied, the flight paths and predicted current density along the probe matched those expected. However, for the flow at lower mach numbers the ion paths are distorted (fig. 4.5).

As show in the previous section (fig. 4.4), at lower flow velocities edge effects are able to extend further upstream of the probe. It is this that leads to the altered flight paths as the ions start to move towards the probe earlier. This results in the same flux of particles striking the probe, however the current density along the length of the probe will be different to that predicted by the analytical model.

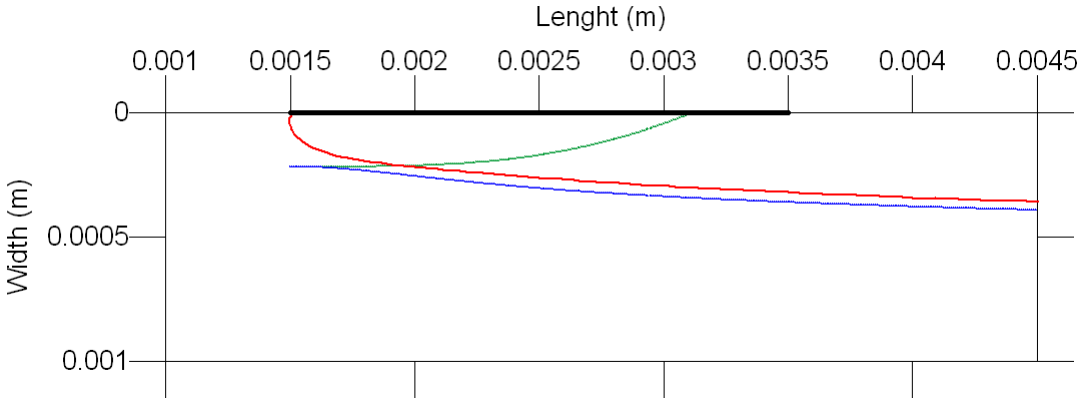

(a) Mach 38

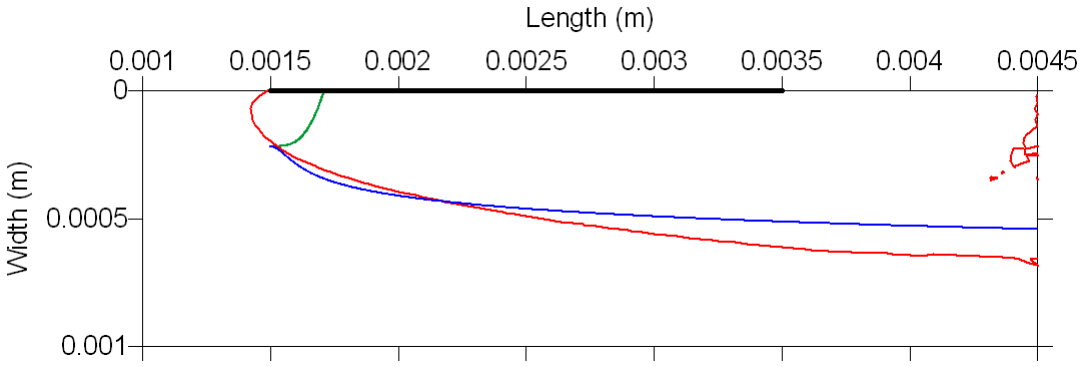

(b) Mach 5

Figure 4.6: *Graphs comparing the sheath width of the 2D simulation (red) against the analytical model (blue) for the parallel case of a* $3mm$ *probe positioned at* $1.5 \times 10^{-3}mm$. *The path of an ion starting at the assumed sheath edge is marked in green. Plasma parameters:* $u_B = 443.7ms^{-1}$, $n_i = 7 \times 10^{16}m^{-3}$, $m_i = 1.79 \times 10^{-25}kg$, $T_e = 0.22eV$, $V_0 = -32V$.

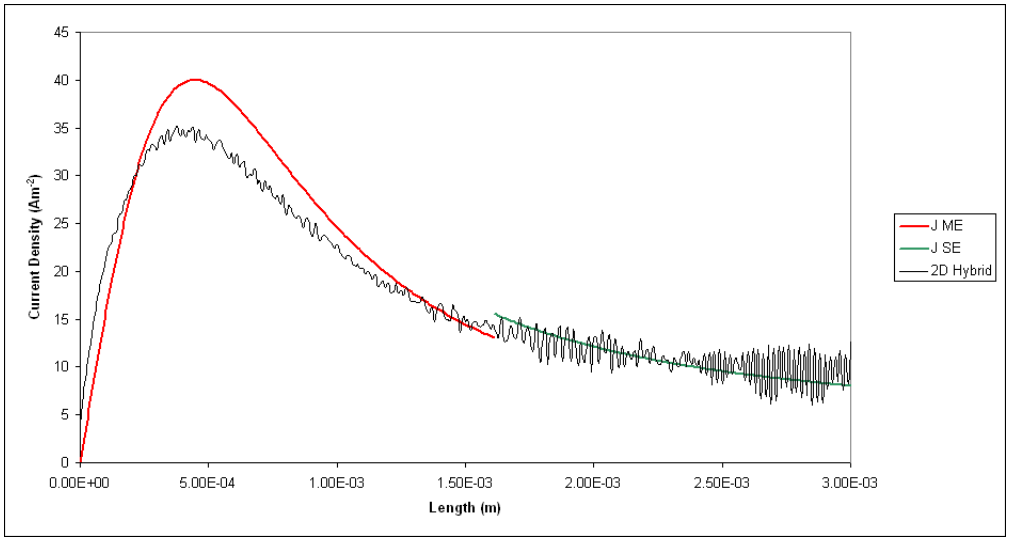

(a) Mach 38

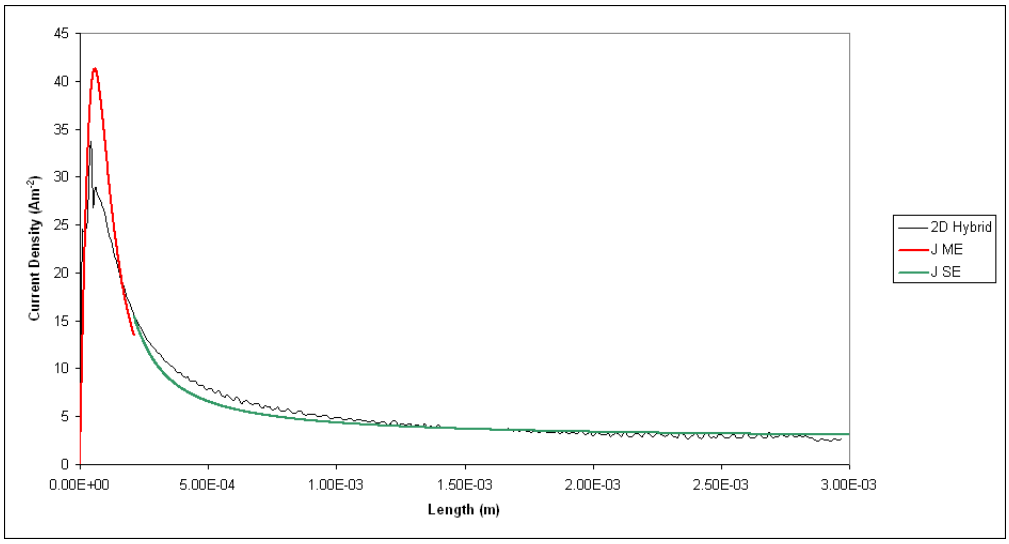

(b) Mach 5

Figure 4.7: *Graphs comparing the current density along the length of the probe in parallel orientation for difference flow velocities. The results of the analytical model J_{me} (eqn. 2.40) and J_{se} (eqn. 2.56) are compared with those of the 2D simulation. Plasma parameters:* $u_B = 443.7ms^{-1}$, $n_i = 7 \times 10^{16}m^{-3}$, $m_i = 1.79 \times 10^{-25}kg$, $T_e = 0.22eV$, $V_0 = -32V$.

$u_f(ms^{-1})$	Mach	I Analytical (Am^{-1})	I Hybrid PIC (Am^{-1})	% Diff
1.69×10^4	38	6.85×10^{-2}	8.07×10^{-2}	-15.1%
8.84×10^3	20	4.15×10^{-2}	5.14×10^{-2}	-19.3%
4.42×10^3	10	2.64×10^{-2}	3.22×10^{-2}	-18%
2.21×10^3	5	1.82×10^{-2}	2.08×10^{-2}	-12.5%

Table 4.2: *Comparison of total ion current at various flow speeds for a probe's surface oriented upstream to the flow direction and biased at $-30V$ as predicted by the analytical model and 2D hybrid code, alongside the percentage difference between the two.*

4.2.2 Upstream $+5^\circ$ Degree Angle

The analytical model was found to consistently underestimate the total ion current in comparison to the results of the 2D simulations (table 4.2). With difference of up to almost 20% in some cases the model's use is drastically limited even at such a relatively small angle off parallel.

Comparing the current density along the probe from the simulation against the analytical model (fig. 4.8) shows the poor estimation of the current density over the sheath expansion phase. Furthermore the high initial velocity towards the surface of the probe means that the more accurately described matrix extraction phase accounts for less of the probe length, increasing the impact of the poor sheath expansion phase description (fig. 4.8a).

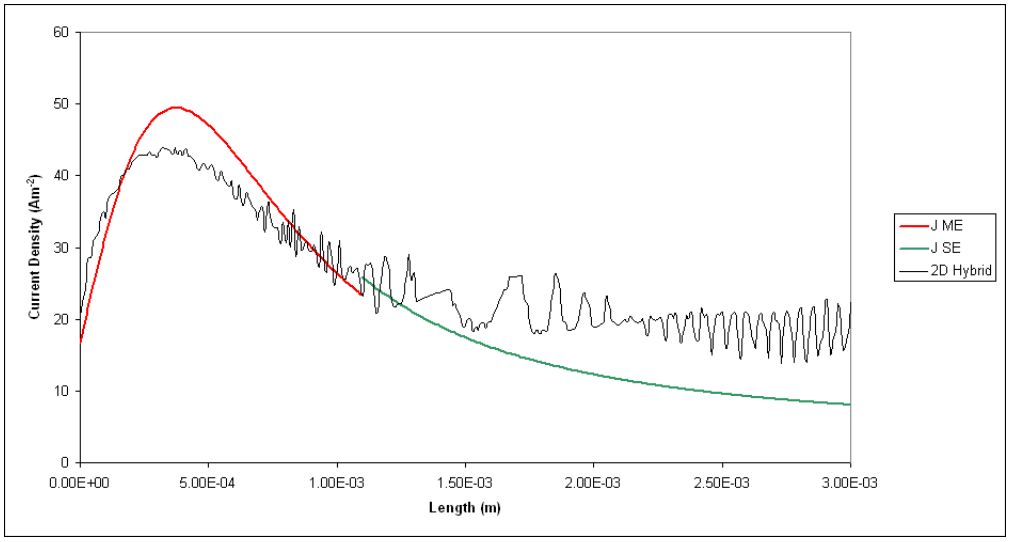

(a) Mach 38

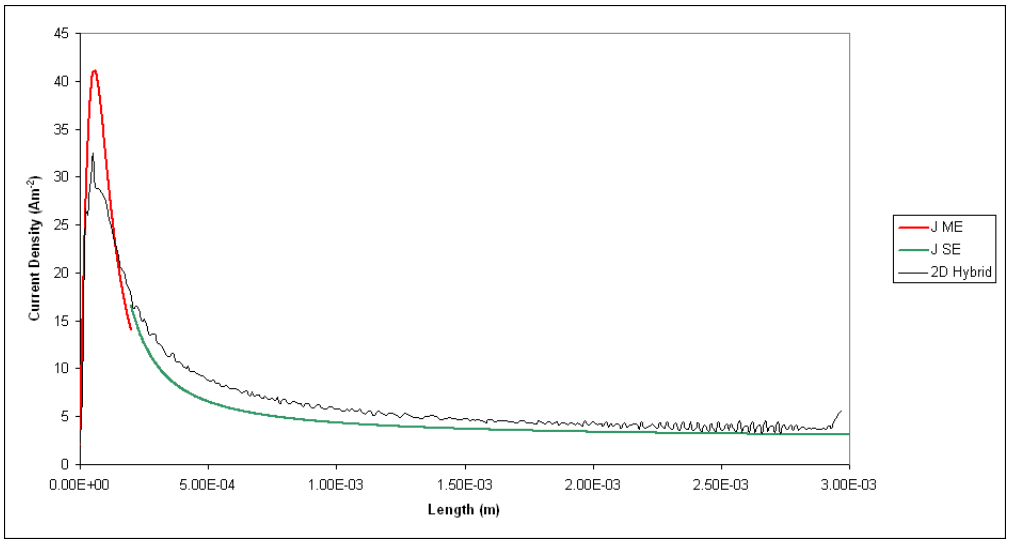

(b) Mach 5

Figure 4.8: *Graphs comparing the upstream current density along the length of the probe for difference flow velocities. The results of the analytical model J_{me} (eqn. 2.40) and J_{se} (eqn. 2.56) are compared with those of the 2D simulation. Plasma parameters:* $u_B = 443.7ms^{-1}$, $n_i = 7 \times 10^{16}m^{-3}$, $m_i = 1.79 \times 10^{-25}kg$, $T_e = 0.22eV$, $V_0 = -32V$.

$u_f(ms^{-1})$	Mach	I Analytical (Am^{-1})	I Hybrid PIC (Am^{-1})	% Diff
1.69×10^4	38	4.59×10^{-2}	4.05×10^{-2}	+13.3%
8.84×10^3	20	3.54×10^{-2}	3.10×10^{-2}	+14.1%
4.42×10^3	10	2.49×10^{-2}	2.21×10^{-2}	+12.6%
2.21×10^3	5	1.78×10^{-2}	1.57×10^{-2}	+13.3%

Table 4.3: *Comparison of total ion current at various flow speeds for a probe's surface oriented downstream to the flow direction and biased at $-30V$ as predicted by the analytical model and 2D hybrid code, alongside the percentage difference between the two.*

4.2.3 Downstream -5° Degree Angle

In the case of the probe's surface oriented downstream of the plasma flow the matrix extraction phase covers a greater length of the probe than that of other orientations (fig. 4.9 *green line*). It had been assumed that given the physical justification of the equations governing this phase, an accuracy close to that of the parallel case would be achieved. Unfortunately, despite the reasonable agreement of sheath behaviour at lower flow velocities (fig. 4.9b), this was not reflected in the results for the total ion current (table 4.3).

At all flow velocities the model continually overestimated the current density along the length of the probe. In turn the model is found to overestimate the total ion current by an average of $\sim 13\%$. Even for the highly supersonic case where matrix extraction phase was estimated to cover most of the probe length the accuracy is not improved.

Like the upstream case before it this failure of the model to predict the ion current to the probe makes its use in interpreting experimental data or

estimating the flow velocity questionable at best.

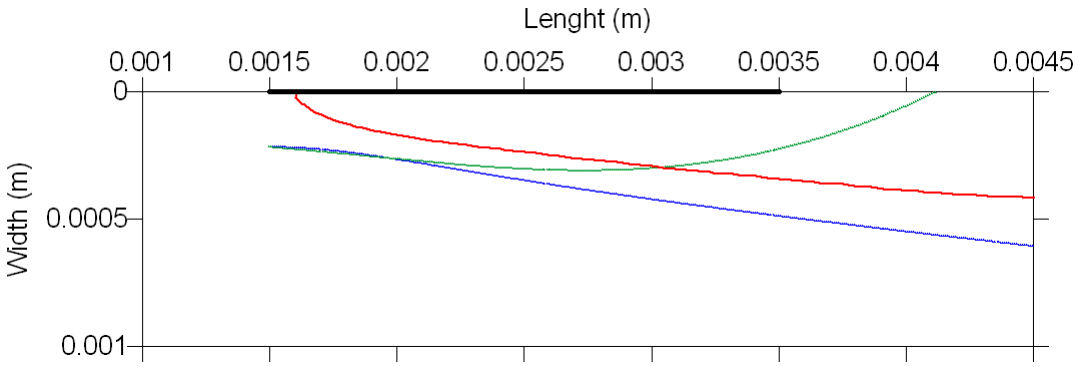

(a) Mach 38

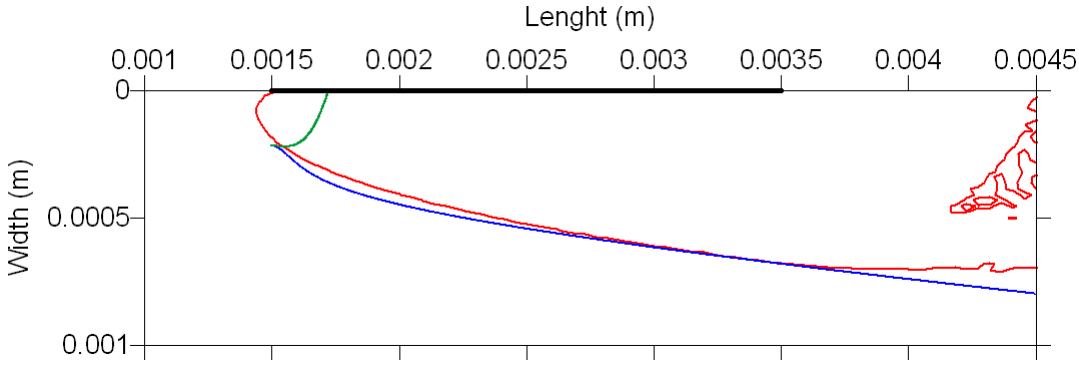

(b) Mach 5

Figure 4.9: *Graphs comparing the sheath width of the 2D simulation (red) against the analytical model (blue) for the downstream case of a 3mm probe positioned at* $1.5 \times 10^{-3} mm$. *The path of an ion starting at the assumed sheath edge is marked in green. Plasma parameters:* $u_B = 443.7 ms^{-1}$, $n_i = 7 \times 10^{16} m^{-3}$, $m_i = 1.79 \times 10^{-25} kg$, $T_e = 0.22 eV$, $V_0 = -32 V$.

4.3 Current Voltage Dependance

A square root dependance of ion current on probe bias has been reported in the literature [18] and seen in experimental results (fig. 5.5a, 5.12) for a

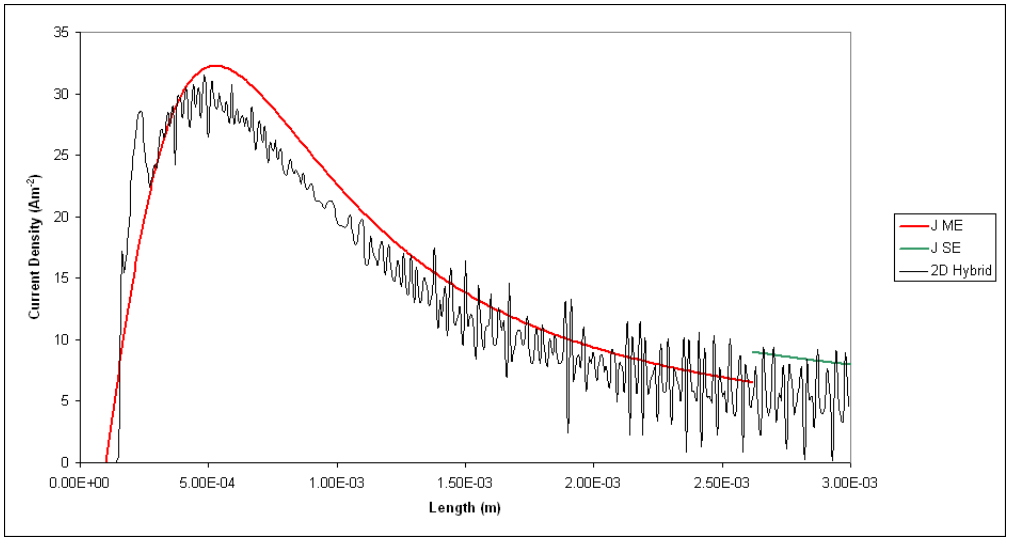

(a) Mach 38

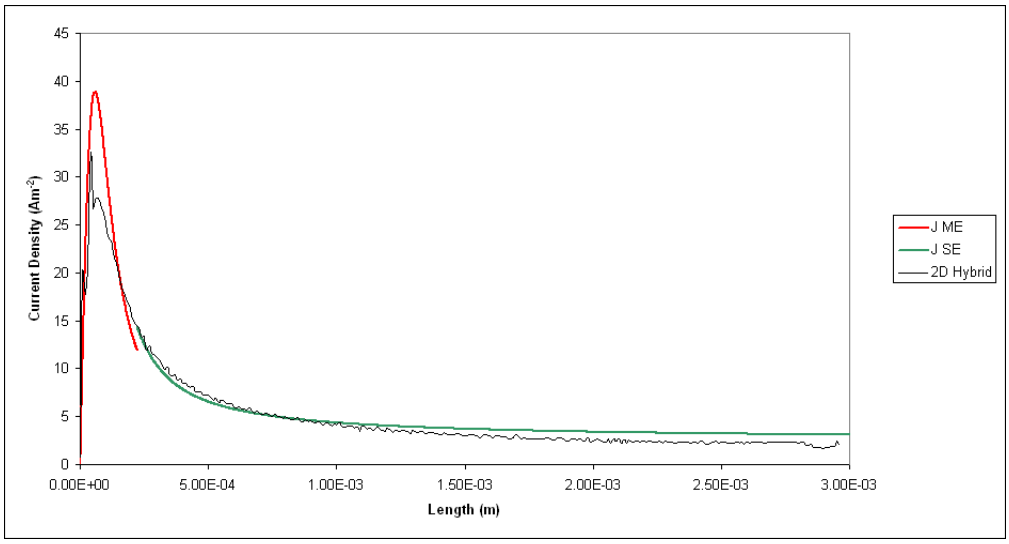

(b) Mach 5

Figure 4.10: *Graphs comparing the downstream current density along the length of the probe for difference flow velocities. The results of the analytical model* J_{me} *(eqn. 2.40) and* J_{se} *(eqn. 2.56) are compared with those of the 2D simulation. Plasma parameters:* $u_B = 443.7ms^{-1}$, $n_i = 7 \times 10^{16}m^{-3}$, $m_i = 1.79 \times 10^{-25}kg$, $T_e = 0.22eV$, $V_0 = -32V$.

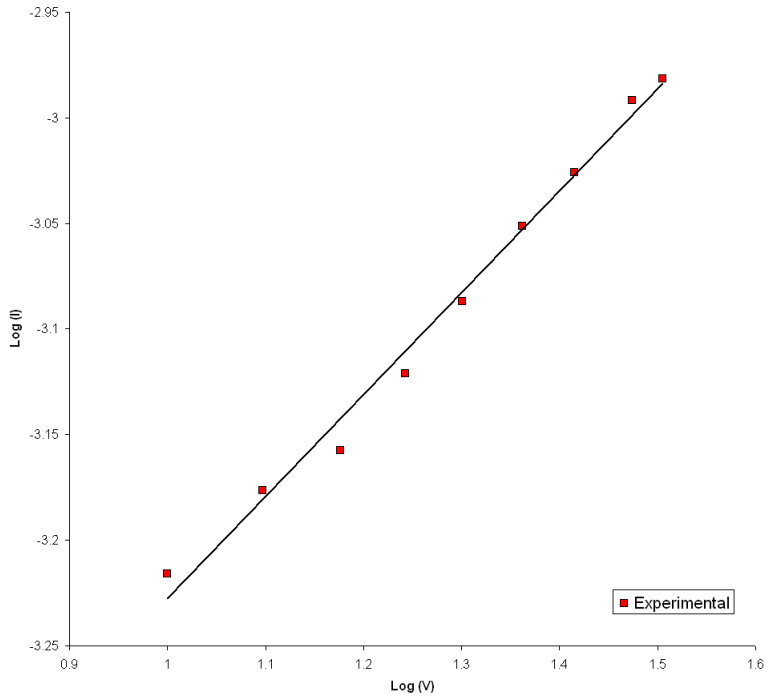

Figure 4.11: *Log-log plot of experimental results for planar probe parallel to the direction of flow within a laser ablation plasma [18]. A linear fit to the experimental data (black line) has a slope of 0.48 illustrating the current's dependance on bias is close to* $I \propto V^{0.5}$

planar probe orientated parallel to the direction of flow. This dependence is also predicted by the analytical model.

Under the parallel condition the model predicts the ion current for the matrix extraction phase to be

$$I_{parallel} = \frac{1}{6} W e n_0 s_0 u_f \left[ln \left\{ 1 + \frac{1}{2} \left(\frac{L\omega_i}{u_f} \right)^2 \right\} + \frac{5 \left(\frac{L\omega_i}{u_f} \right)^2}{2 + \left(\frac{L\omega_i}{u_f} \right)^2} \right], \quad (4.1)$$

where L is the length of the phase, W is the probe width and

$$s_0 = \sqrt{\frac{2\epsilon_0 V_0}{e n_0}}, \quad (4.2)$$

is the sheath width.

The bias applied to the probe controls the sheath width which for a plasma with constant physical parameters exhibits the relationship

$$I_{parallel} \propto s_0 = \sqrt{\frac{2\epsilon_0 V_0}{e n_0}}, \quad (4.3)$$

between the current and the probe bias.

So long as the length of the probe does not exceed the matrix extraction phase this relationship holds. Once the probe's length extends into the sheath expansion phase it starts to break down. This happens gradually with increasing length as most current is collected over the matrix extraction phase.

4.4 Discussion

This chapter set out to compare the performance of the analytical model against numerical simulations carried out using the 2D hybrid code. This was done to assess the resilience of the model to any two dimensional phenomena such as the probe's edge effects.

The results of the 2D simulations were compared against those of the 1D hybrid code. It was found that for highly supersonic flows the comparison was reasonable, but as the flow velocity dropped the size and impact of the edge effects grew. On the positive side these disturbances were found to be sufficient to prevent the electron shock waves seen in the full particle simulations, justifying the use of hybrid codes.

The results of the comparison between the analytical model and the more accurate physical simulation of the 2D code was also presented. For the parallel condition good agreement was obtained over a variety of flow velocities. Even at lower flow velocities where the upstream disturbances were greatest this remained true and an explanation was presented. The results for the upstream and downstream conditions were also presented. The reasons and implications for the poor performance of the model at these orientations and the implications for its use in the interpretation of experimental results was considered.

Finally the observed square root dependance of the ion current on the applied bias was shown and the prediction of this relationship by the analytical model was illustrated.

CHAPTER 5

Experimental Comparisons

The true test of any model is how well it compares against real experimental results. In this chapter the analytical model presented in Chapter 2 is compared against the results of two very different experimental plasmas. The first is a DC plasma with a constant density flow measured over a wide range of applied bias. The second is a laser produced plasma plume with time varying density. In both cases the flow speed is supersonic with respect to the ion sound speed and a planar probe oriented parallel to the direction of flow was used to make the measurements.

5.1 Planar Probe in Double Plasma Device

In University College Cork a campaign of experimental work was carried out in 2006 by Deirdre O'Leary under the supervision of Dr. Paddy McCarthy

and Prof. Richard Armstrong. The results of this work provide the opportunity to compare the analytical model against actual experimental work. For her analysis of the results for her report [69] we provided an early version of our analytical model's matrix extraction phase to which they added their own extension for the sheath expansion phase.

What follows here is an independent comparison of the experimental results against the analytical model detailed in chapter 2, using the original experimental data kindly provided by Dr. Paddy McCarthy[1].

5.1.1 Experimental Setup

The experimental setup used by Deirdre O'Leary [69] to investigate transport in a Xenon plasma using Langmuir probes is shown in figure 5.1 . The Double plasma device consists of a cuboid source chamber and a cylindrical target chamber.

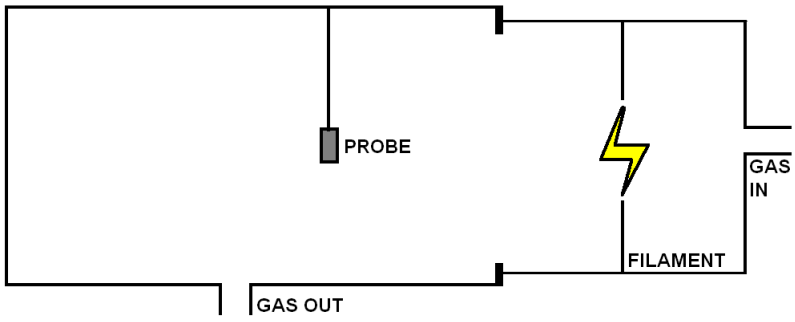

Figure 5.1: *Diagram of the Double plasma device chamber used in the experiments [69] carried out in University College Cork. The cylindrical target chamber* $24.7cm \times 46cm$ *is shown on the left and the cuboid source chamber* $24cm \times 19cm \times 20cm$ *on the right.*

The source chamber consisted of two regions, the driver region containing

[1]Department of Physics, University College Cork, Ireland. e-mail: pjm@ucc.ie

the filaments and an extraction region separated by a magnetic filter. Xenon gas was fed into the source chamber and a large DC bias applied to the filaments to generated the plasma. The plasma was then directed into the target chamber though the extraction region.

The cylindrical target chamber contained the various diagnostic apparatus and pump aperture from which the gas was extracted from the chamber. This area was assumed to be free of magnetic fields though the experimenters admitted that some bleed from the source chamber may have been possible. Pressure within the chamber was measured using both Pirani and Penning gauges from which the plasma density was estimated.

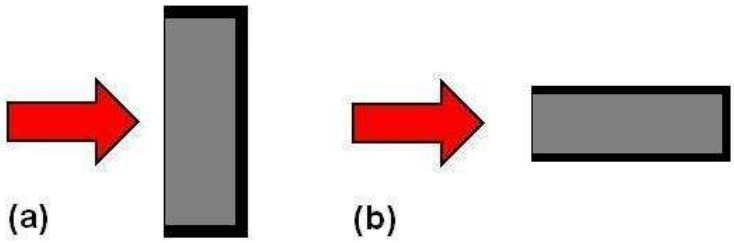

Figure 5.2: *Diagram of a planar probe with (a) "radial" and (b) "axial" orientation to the direction flow.*

Several configurations of probe were used for the experiments, but only the planar Langmuir probe results are of relevance to this work. The probe used was mounted as shown in figure 5.1 so that it lay along the central axis of the chamber allowing it to be rotated 360 degrees presenting either the short edge "axial" or long edge "radial" directly into the flow. In both cases the surface of the probe was oriented parallel to the direction of flow. It was constructed from iron foil with dimensions $40\mu m \times 25.5mm \times 1.23mm$ and one side insulated using "Cermabond".

5.1.2 Plasma Parameters

In addition to the recorded current versus probe bias results from the experiment, estimates of the pressure, ion density and election temperature were also provided (table 5.1.2). The A and R suffix indicate which of the probes edges was presented to the flow.

The chamber pressure was measured using both Pirani and Penning gauges. The ion density and electron temperature were estimated using fits to the experimental data. As the plasma is weakly ionized the flow velocity was determined from the ion flux written in the form of Fick's Law [4]

$$\Gamma = nu_f = -D_a \nabla n, \tag{5.1}$$

which for this case results in

$$u_f = \frac{D_a}{\lambda}, \tag{5.2}$$

where D_a is the ambipolar diffusion coefficient and $\lambda = 11.9 \pm 0.4cm$ [69] the electron density fall off for the Xenon plasma along the centre of the target chamber (fig. 5.1).

The full set of the experimental plasma parameters and flow velocity supplied by the team in University College Cork for use in the simulations and analytical models are listed in the following table.

Data Set	$P_{Xe}(mbar)$	$n_i\,(m^{-3})$	$T_e\,(eV)$	$u_B\,(ms^{-1})$	$u_f\,(ms^{-1})$
A1	8.0×10^{-5}	3.58×10^{15}	0.71	7.22×10^{2}	4.03×10^{3}
R1	8.0×10^{-5}	4.30×10^{15}	0.78	7.57×10^{2}	4.23×10^{3}
A2	3.2×10^{-5}	1.46×10^{15}	1.03	8.70×10^{2}	1.21×10^{4}
R2	3.2×10^{-5}	2.50×10^{15}	1.03	8.70×10^{2}	1.31×10^{4}
A3	4.0×10^{-5}	1.88×10^{15}	0.88	8.04×10^{2}	8.98×10^{3}
R3	4.0×10^{-5}	2.10×10^{15}	0.86	7.94×10^{2}	8.88×10^{3}
A4	2.4×10^{-5}	1.19×10^{15}	1.05	8.78×10^{2}	1.63×10^{4}
R4	2.4×10^{-5}	1.76×10^{15}	1.02	8.66×10^{2}	1.61×10^{4}

Table 5.1.2: Measured and estimated plasma parameters for experimental work carried out using a Xenon plasma ($m_i = 2.18 \times 10^{-25} kg$) in University College Cork by Deirdre O'Leary.

5.1.3 Comparison with Analytical Model

The results of the experimental work when compared against the results of the analytical model and the 2D hybrid PIC code. Only values from the experimental data for the physical parameters of the Xenon plasma were used in the model and simulations. In all cases the probe was parallel to the direction of flow in either an radial or axial orientation.

The predicted end of the matrix extraction phase according to the estimate (eqn. 2.47) was found to be consistently within about 93% of the value predicted by equation (2.46), which describes the time taken for an ion starting at $(x = s_0;\, y = 0)$ to cross the sheath. Depending on flow velocity and the plasma's physical properties, this equated to distances of between $7mm$ and $14mm$ along the probe's length.

Radial Orientation

In the case of the probe oriented radially, the long edge of the probe was facing into the flow (fig. 5.2a). Despite the probe's short length of $1.23mm$ the current collection doesn't occur entirely within the matrix extraction phase.

The R1 case demonstrated the best agreement of all radial cases, with very good agreement between the experimentally recorded current and that predicted by both the simulations and the analytical model up to a probe bias of $-60V$ with approximate agreement beyond (fig. 5.3a).

In cases R2-R4 (figs. 5.3b, 5.4a, 5.4b)satisfactory agreement is observed at smaller negative bias ($< -30V$). However, as the bias becomes increasingly negative the agreement becomes increasingly poorer.

Inaccuracies in the estimation of the plasma physical parameters cannot solely explain the reason for this disparity at greater negative bias, as all four sets of data are assumed to have been subject to the same sources of error.

In the case of R1 the probe length covers over 68% of matrix extraction phase while the other cases cover as little as 12%. Given the approximate nature of the sheath expansion phase's current description this difference was considered as a possible source for the poor agreement.

Data Set	% of matrix extraction phase covered
R1	68%
R2	19%
R3	24%
R4	12%

However, the lack of a significant difference in accuracy of case R3 over R2 or R4 along with the lack of any justification for the existence of a mini-

mum coverage threshold for the matrix extraction phase that would impact accuracy lead to the conclusion that it was also unlikely to be the cause.

As noted earlier in 4.3, the current in the parallel case exhibits a square root dependance on the probe bias, $I \propto V_0^{\frac{1}{2}}$. A log-log plot of the current versus probe bias for the case R1 (fig. 5.5a) shows the experimental result is close to the expected behaviour. By contrast in the cases of R2-R4 the relationship would appear to be almost linear, as shown in the log-log plot for case R2 (fig. 5.5b), which is typical of the behaviour in all three cases. This suggested that there was a fundamental change in the conditions under which the probe operated.

The theory assumes that the probe is both planar and large enough that edge effects do not need to be explicitly considered (i.e. the sheath width is small compared to the probe length). If this condition is violated then the model can no longer be valid. The applied bias at which the initial sheath width (eqn. 4.2) exceeded the probe length for each case was measured.

Data Set	Breakdown Bias
R1	$-60V$
R2	$-30V$
R3	$-15V$
R4	$-20V$

In each case at increasing negative bias beyond this point the initial sheath width becomes progressively greater than the probe length. When this occurs the physical assumptions on which the analytical model depends breakdown. In the case of each data set, R1-R4 the agreement between the model and the experimental results begins to deteriorate at approximately the same bias at which this occurs (fig. 5.3 & 5.4), indicating that this is the most probable cause of the failure of the model.

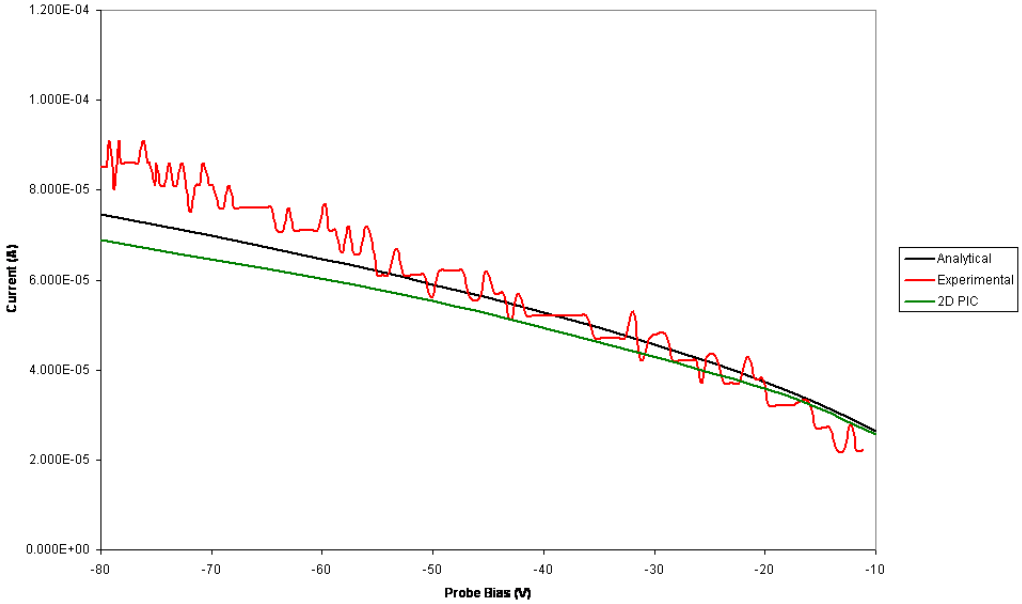

(a) Case R1

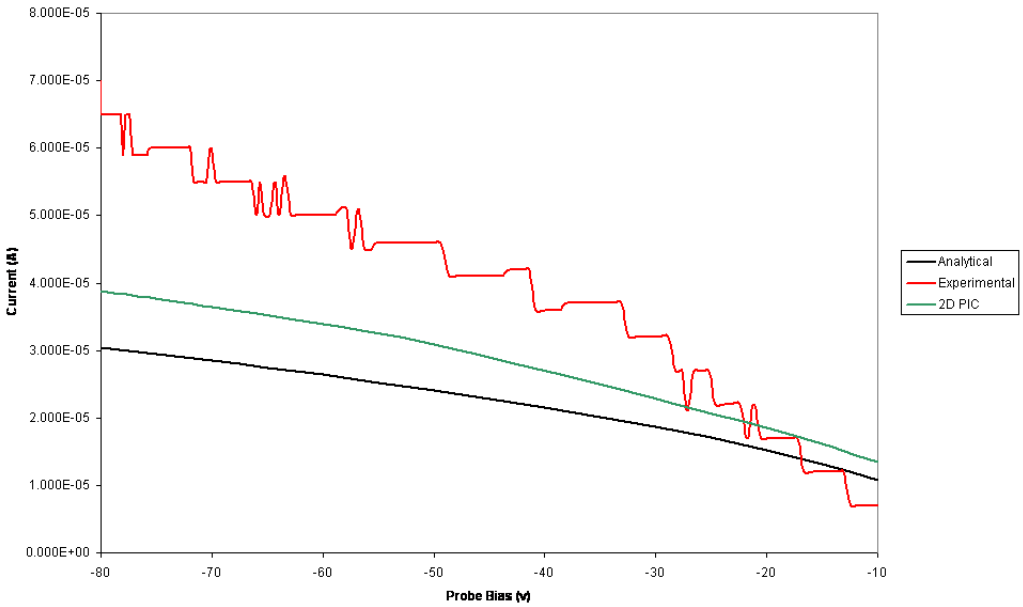

(b) Case R2

Figure 5.3: *Comparison of the results from the analytical model and 2D hybrid PIC against the experimental data (see Table 5.1.2).*

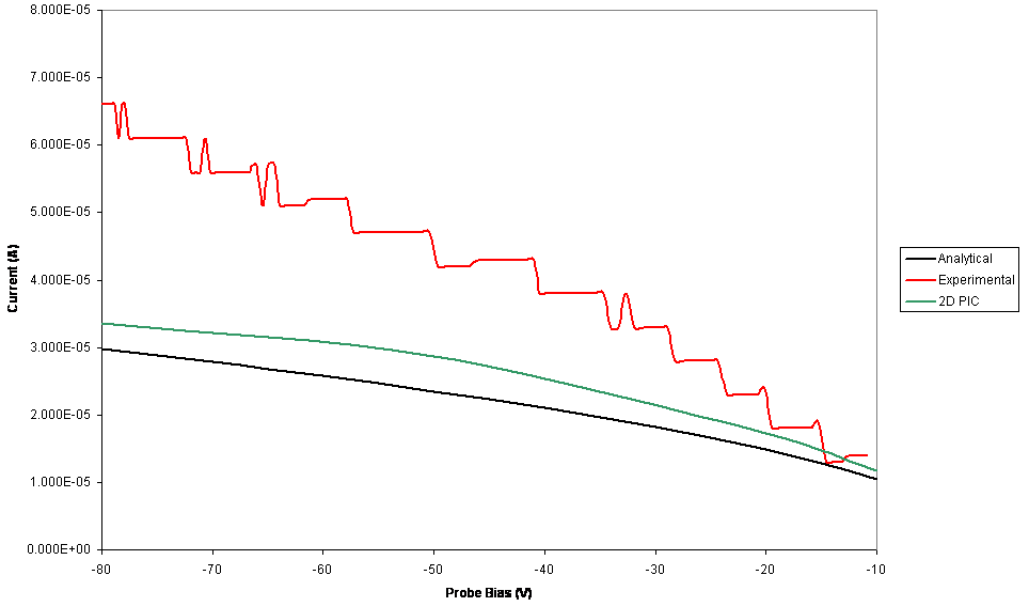

(a) Case R3

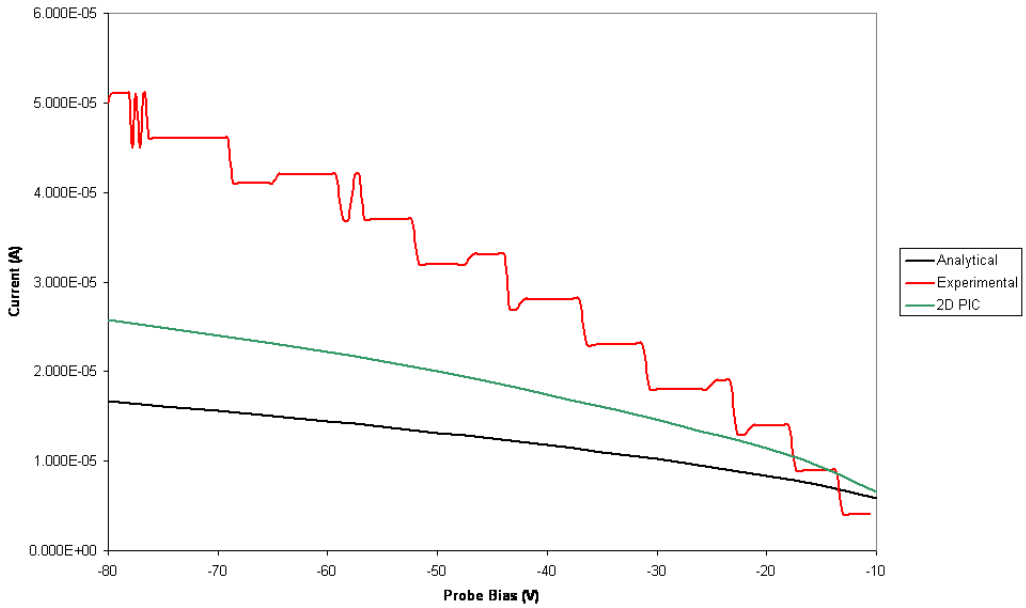

(b) Case R4

Figure 5.4: *Comparison of the results from the analytical model and 2D hybrid PIC against the experimental data (see Table 5.1.2).*

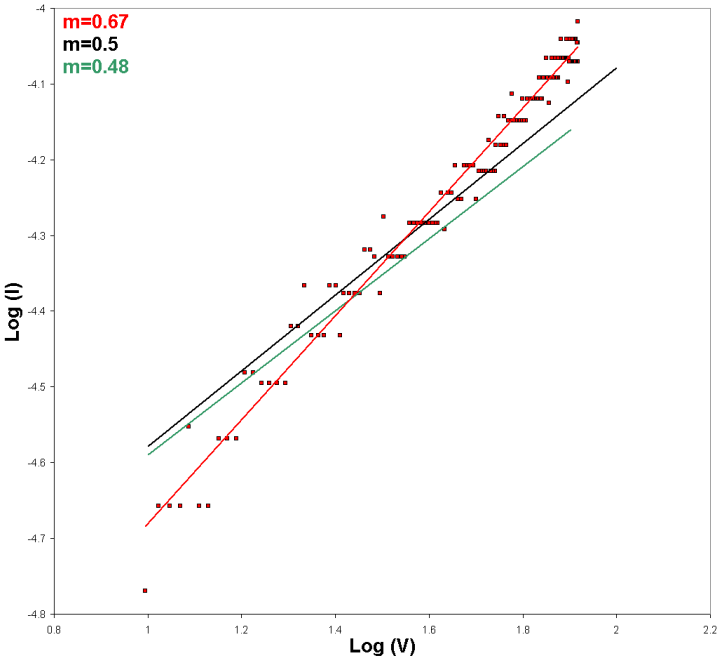

(a) Case R1

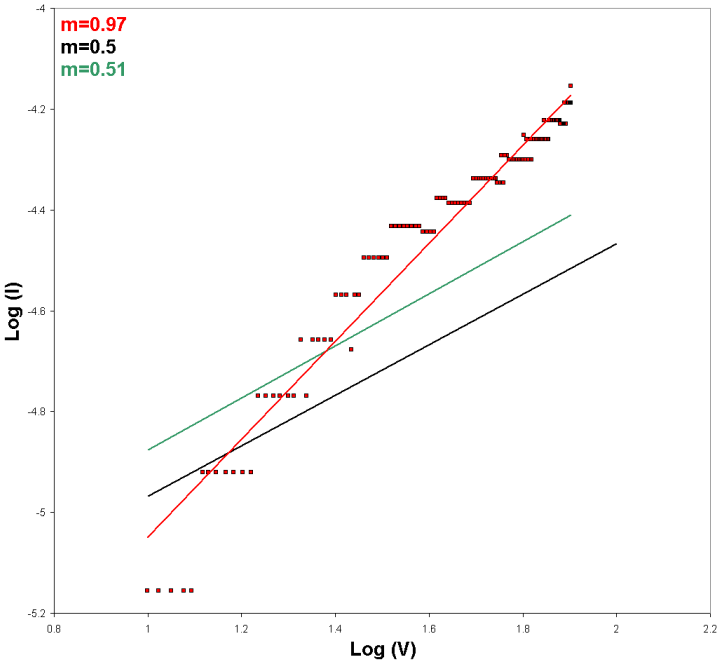

(b) Case R2

Figure 5.5: *Comparison of the log-log plots showing the variation of ion current with probe bias. Fitted slopes for the analytical model, 2D hybrid PIC and experimental data are graphed.*

Axial Orientation

In the case of the probe oriented axially, the short edge of the probe faces into the flow (fig. 5.2b). The probe's rather excessive length of $2.25cm$ means that the current is collected almost entirely in the sheath expansion phase in all four cases.

The agreement between the model and the experimental data in all four cases is very poor, as illustrated by the graphed examples (fig. 5.6). The reason for this poor agreement is again most likely due to the initial sheath width exceeding the probe width and the resulting edge effects dominating. However, a failure of the model to adequately describe the sheath expansion phase over the long term cannot be entirely ruled out. From the experimental data that was available we are unable to state this definitively, though given the results from comparisons for similar conditions (section 4.7b) it is unlikely. Inaccuracies in the experimental values for n_i and T_e also cannot account for the poor agreement as they affect the magnitude of the I-V curve rather than its slope.

No numerical results using the 2D hybrid code were generated, as the length of the probe and the constraints on cell size due to the CFL condition (sec. 3.4.5) required a number of particles beyond the resources of the machines available to us.

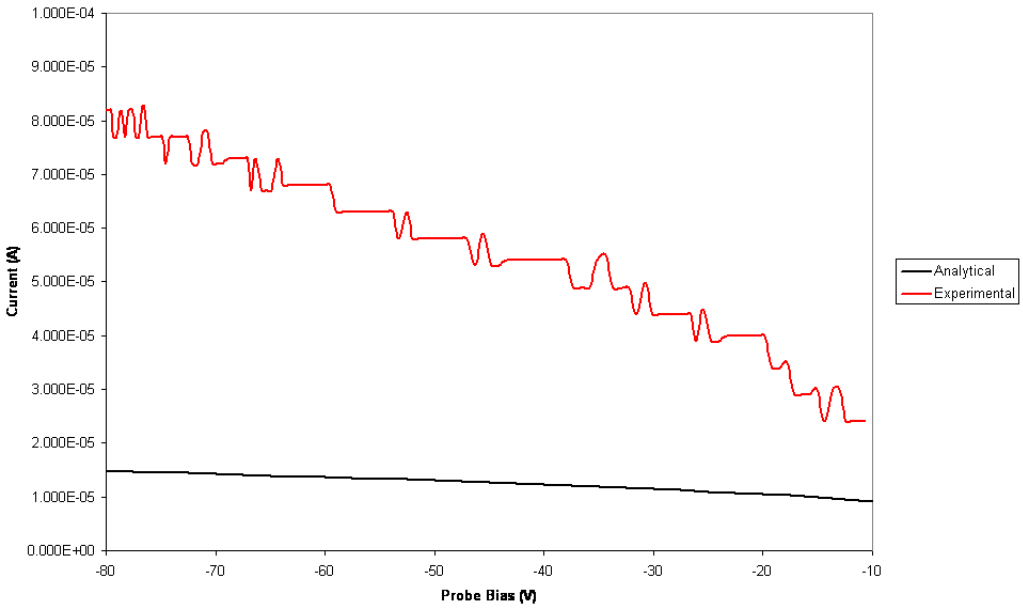

(a) Case A1

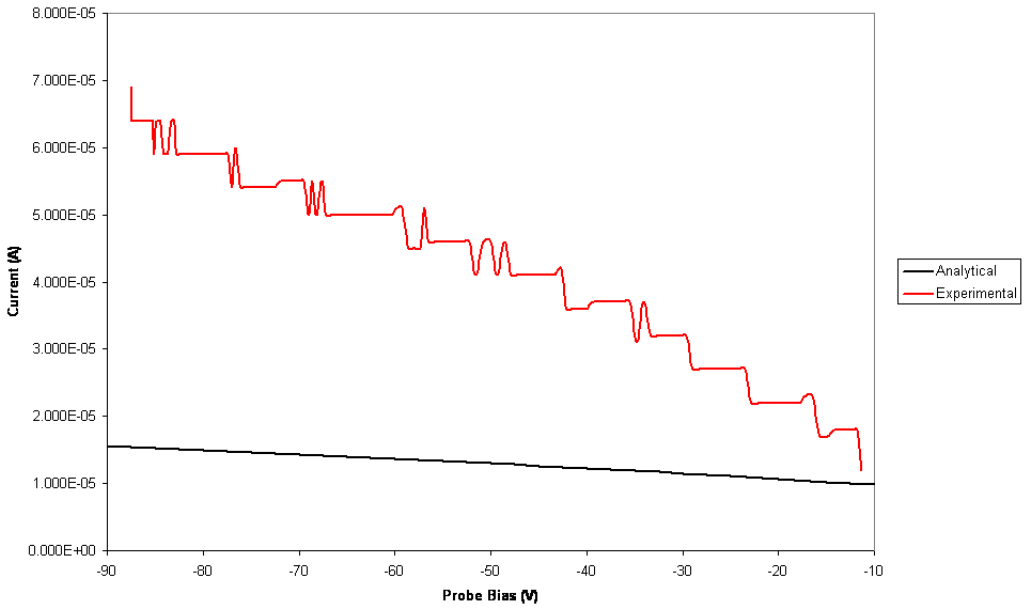

(b) Case A3

Figure 5.6: *Comparison of the results from the analytical model against the experimental data (see Table 5.1.2).*

5.2 Planar Probe in Laser Ablation Plasma

Along side our computational work here in Dublin City University a campaign of experimental work was carried out by Dr Brendan Doggett under the supervision of Prof. James Lunney in Trinity College Dublin, to investigate the behaviour of a planar Langmuir probe in a laser ablation plasma, as part of their work on the characterisation of laser produced plasma.

The following results from the experimental work were kindly provided by Dr Doggett[2] for comparison against the analytical model.

- Current versus Time for the probe surface oriented parallel to the direction of flow, with an applied bias of -32V,-20V,-15V, -10V.
- Current versus Time for the probe surface oriented perpendicular to the direction of flow, with an applied bias of -30V, -20V, -15V, -5V.
- The flow velocity as determined from the time of flight (TOF) between the target and the probe.
- The estimation of electron temperature (eV) from experimental results for the parallel or perpendicular orientations.

In each case the probe used by the TCD team to collect the measurements was a planar Langmuir probe of width $13mm$ and length $3mm$ and the results averaged over 10 laser shots.

5.2.1 Experimental Setup

The experimental setup used by Dr Doggett in his work was illustrated in figure 5.7 and further detailed in the paper [18], but a summary is also provided here.

[2]e-mail: doggettb@gmail.com

The vacuum chamber, within which the apparatus was mounted, is a stainless steel barrel. It had an internal volume of 15 litres and an obtainable pressure of $5 \times 10^{-6} mbar$.

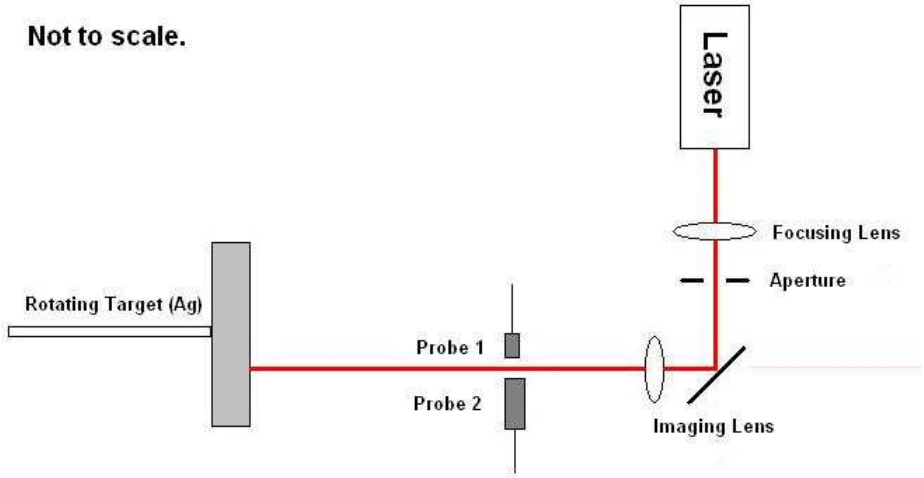

Figure 5.7: *Diagram of the experimental set up used in the experiments [18][70] carried out in Trinity College Dublin (TCD). The probes and target were mounted in a 15 litre stainless steel barrel vacuum chamber with the laser outside.*

The laser used in the experiments was a Lambda Physics Krf (LPX 100) with a wavelength of 248 nm and 26 ns pulse width. The laser was focused onto the target with a spot size of approximately $1mm \times 0.5mm$ giving a laser fluence of $1 Jcm^{-2}$.

The target was composed of sliver and rotated during laser shots, thus minimizing the effects of surface ablation on the plume formed.

Two planar probes were were used in the experiment. Both were mounted $9.5mm$ from the target. Probe 1 with a size of $4.5mm \times 2mm$ was used to ensure reproducibility of the ablation plume was achieved. Probe 2 of width $13mm$ and length $3mm$ was positioned normal to the surface. It was mounted with its long side normal to the direction of flow and could be rotated around

its short axis.

5.2.2 Plasma Parameters

To justify the application of the analytical model to the laser ablated plasma plume requires that the plasma meets several conditions. The first regarding the lack of magnetic fields is reasonable and the plume is also reported to be collisionless [18]. In addition with a flow velocity of 38 times the ion sound speed of $443.7ms^{-1}$, it can be safely assumed that the plasma is supersonic when it encounters the probe.

The analytical model also makes the assumption that the ions are singly charged. In his thesis [70], Doggett reports that for a laser fluence of $1.1Jcm^{-2}$ only singly charged ions were detected in the plume. However in the case of a rotating target the plume was found to be contaminated with carbon or oxygen at very early times. This is identifiable as the early "knuckle" in the recorded current in figure 5.10 and 5.11. Comparisons against the stationary target that lack the contamination showed it was confined to the leading edge of the plume. Therefore it meets the model's assumption of only singly charged ions within the plume with reasonable confidence.

The plasma parameters, as determined by the TCD group for the experimental results [18] for the laser ablated plume at a distance of $9.5cm$ from the target were:

Parameter	Symbol	Value
Silver Ion mass	m_i	1.79×10^{-25} kg
Flow Velocity	u_f	$1.7 \times 10^4 \pm 0.1$ ms^{-1}
Probe bias	V	$-32V \rightarrow -5V$
Ion Density	n_i	time dependant
Electron Temp.	Te	time dependant

The density of the laser ablation plume as explained in section 1.1.1 is time dependent. Therefore the current collected by the probe is not constant. As explained in section 1.2.1 the current collected by a negatively biased planar probe with its surface normal to a constant flow is described by [47]

$$I_i = Aen_i u_f, \tag{5.3}$$

where A is the probe area, n_i the ion density, u_f the ion flow velocity and e absolute electron charge. Thus, taking the current recorded by the probe (fig. 5.8a) in this orientation and rearranging equation (5.3) gives

$$n_i = \frac{I_i}{Aeu_f}, \tag{5.4}$$

which allows the density at a give time t to be calculated (fig. 5.8b).

The electron temperature of the plasma plume has also been reported, in the literature, to be time dependant [8, 12]. Electron temperatures are normally determined from the slope of the linear part of the electron-retarding region of the I-V trace. However, as noted in the thesis by Dr Doggett [70] the estimation of the electron temperature can vary by as much as an order of magnitude depending on whether the results from the perpendicular or parallel probe orientation are used:

Probe Orientation	Peak Current	Low Current
perpendicular	2.5 eV	0.2 - 1.0 eV
parallel	0.22 - 0.5 eV	0.1 - 0.22 eV

It is a reasonable assumption that as for the ion current collected by the probe, the parallel orientation will minimize the influence of the flow velocity on the measured electron temperature. Unfortunately the experimental results required to estimate the temperature at each of the relevant density points was unavailable. Therefore an average temperature of $0.22eV$

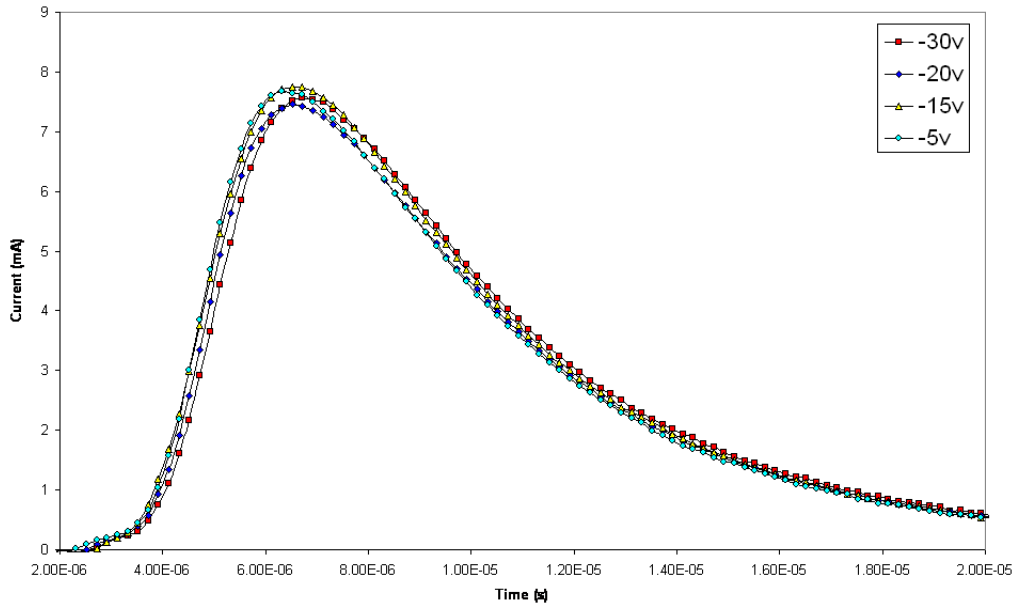

(a) Current versus Time [18]

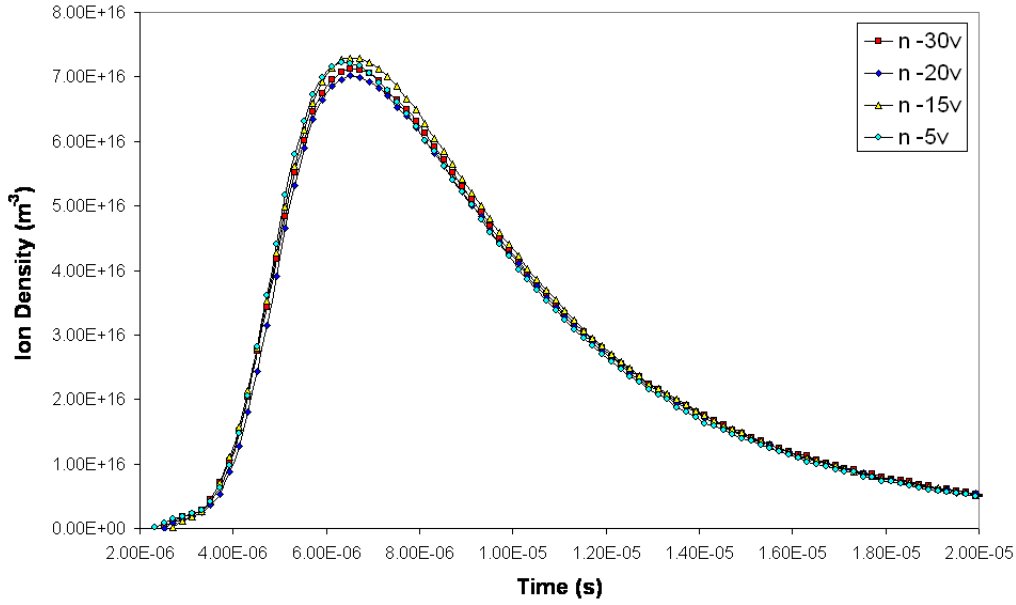

(b) Density versus Time

Figure 5.8: *Graphs of: (a) the measured ion current for a planar probe (*$13mm \times 3mm$*) oriented perpendicular to the flow at varying probe bias, as recorded by Dr Doggett [18]; (b) the changing density of the plasma plume over time, derived from the measured experimental values.*

was selected from the results for the parallel orientation [18, 70] for use in comparing the model against the experimental results.

5.2.3 Comparison with Analytical Model

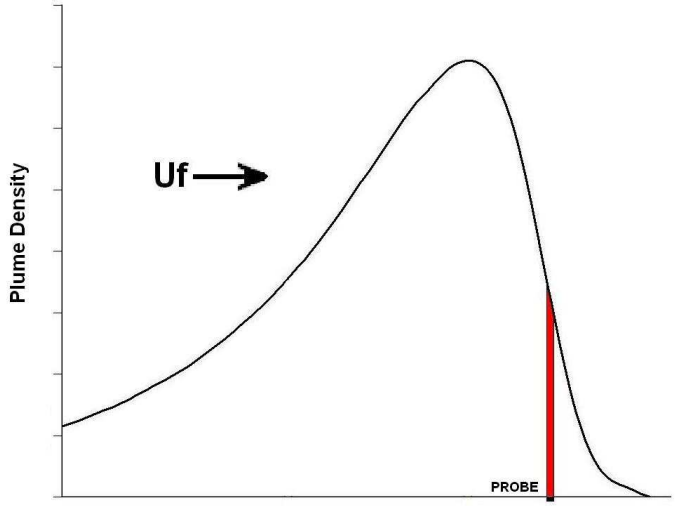

Figure 5.9: *Diagram of the change in plume density as it flows over the probe. The variation in density along the length of the probe is represented by the red area (to approximate scale).*

The results of the experimental work are compared against the results of the analytical model in this section. Comparison between with the 2D hybrid code is not provided as it was not possible to simulate a time varying density for the reasons explained in section 3.4.1. The probe is parallel to the direction of flow with the long axis facing into the flow. The model had no free parameters and only values from the experimental data for the physical parameters were used.

The experimental data was collected at intervals of $2 \times 10^{-7} s$, timed from the firing of the laser at $t = 0s$. The time taken for an element (fig. 2.2b)

of the plume to travel the probe's length of $3mm$ is calculated from the flow velocity of $1.7 \times 10^4 ms^{-1}$ to be $1.76 \times 10^{-7} s$.

Examining the change in density between data points (fig. 5.8b) the largest change observed was 35% and the median change just $\sim 4.4\%$. Given that (a) the time for an element to cross the probe is less than the time between sample points, (b) over this time the typical change in density was small and (c) the density at the leading edge of the probe is most accurate for the matrix extraction phase that dominates the current collected (fig. 2.4), it is justifiable to assume the density at time t is representative of the plume for the time taken to traverse the probe. This assumption along with the use of the averaged value for T_e, greatly simplifies the application of the model to the experimental data.

The general agreement between the model and the experimental results over the total duration of the plume is reasonably good (fig. 5.10 and 5.11) at each value of the probe bias. However, two regions of disagreement are apparent at early time and over the period of peak current. As pointed out earlier the "knuckles" in the experimental results at early time is due to the suspected contamination by oxygen and carbon, which due to the assumption that only silver is present, leads to an inaccurate density estimate.

Over the period of peak current the model exhibits the same trend as the experimental data, however the predicted peak current is $\sim 75\%$ of the experimental value in each case. A problem with the model for the the sheath expansion phase as suggested in the axial case of the Cork data (sec. 5.1.3) is unlikely. The contribution to the total current from this phase is small ($> 10\%$) and the problem is also seen beyond the area of peak current.

It is instead most likely that the use of the averaged electron temperature instead of the higher actual peak value over this region has caused the diver-

gence. However, the maximum value of $0.5eV$ for the parallel orientation is still short and a value approaching that recorded for the peak current in the perpendicular orientation ($\sim 2eV$) is required to get closer agreement to the peak current.

It is possible that the electron temperature as measured by the probe parallel to the flow underestimates the true temperature. It is certain that the measure of T_e from the perpendicular case overestimates its value due to the high flow speed. Without access to a more accurate experimental measure of T_e over the life time of the plume it is not possible to rule out other causes. However, it is at the very least a large contributor to the short fall in predicted current.

As discussed in section 4.3 the results are expected to show a square root dependance of current on voltage $I \propto V_0^{\frac{1}{2}}$. Looking at the experimental peak current at $t = 5.92 \times 10^{-6}s$ over the full range of applied bias (fig. 5.12), the expected behaviour is evident with the measured slope of 0.48 on a log-log graph[3]. This result is typical and the same behaviour is repeated at earlier and later times. The analytical model's ion current collected over the matrix extraction phase has a perfect square root dependance. The total current collected from both phases still shows behaviour close to that expected with a slope of 0.43 on a log-log graph even though at this time the sheath expansion phase accounts for almost 50% of the total probe length.

[3]The greater current in the experimental results is due to the use of the median value for electron temperature resulting in the underestimation of the peak current by the hybrid code and the analytical model.

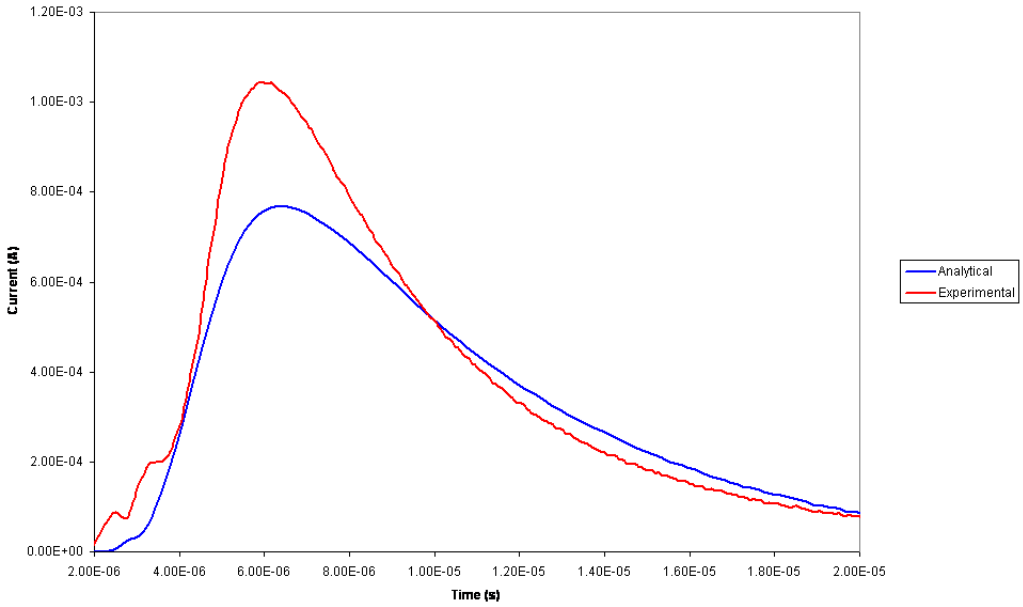

(a) Probe bias -32v

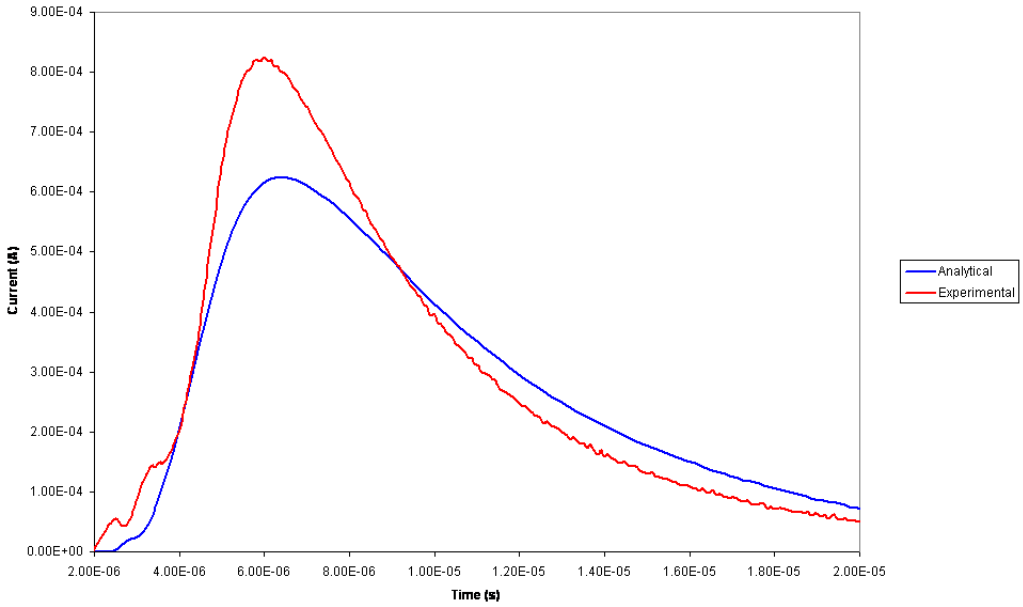

(b) Probe bias -20v

Figure 5.10: *Comparison of the results of the analytical model against the experimental data for the parallel oriented probe in a laser ablated plasma plume of silver,* $u_f = 1.7 \times 10^4 ms^{-1}$*, average electron temperature* $T_e \approx 0.22eV$ *at points of known density* n_i *(figure 5.8b).*

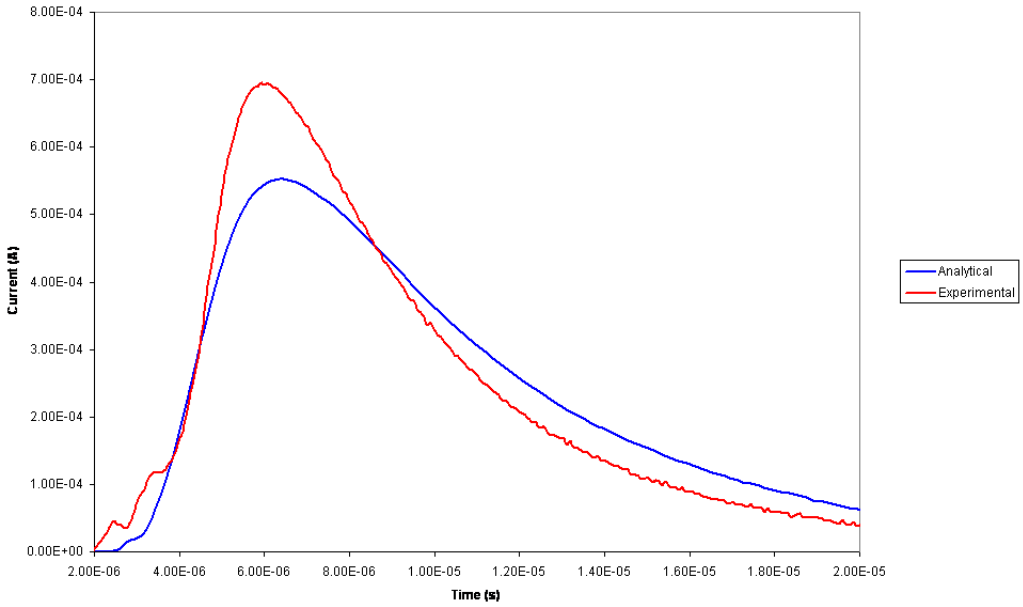

(a) Probe bias -15v

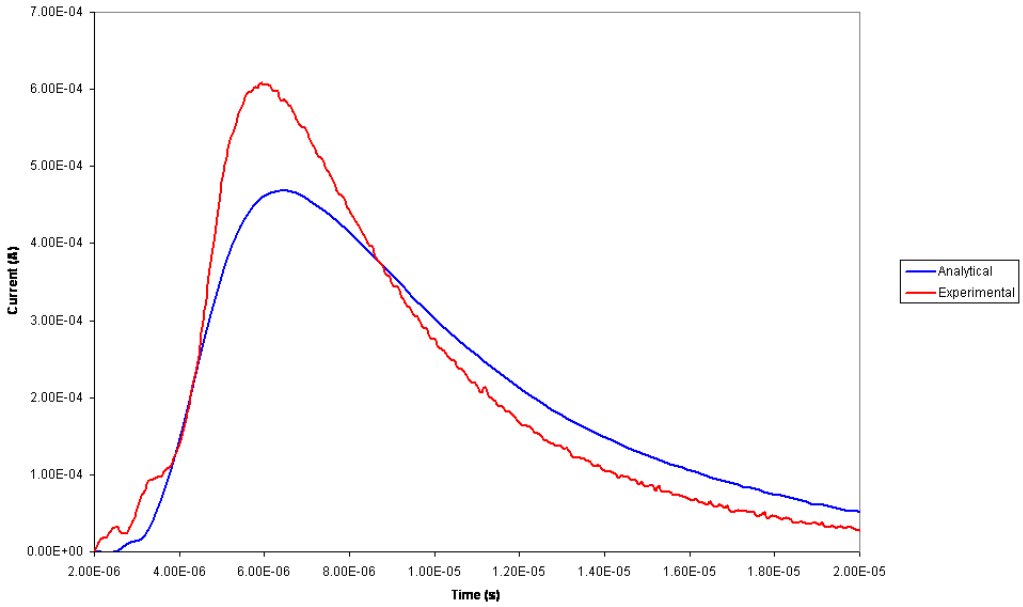

(b) Probe bias -10v

Figure 5.11: *Comparison of the results of the analytical model against the experimental data for the parallel oriented probe in a laser ablated plasma plume of silver,* $u_f = 1.7 \times 10^4 ms^{-1}$*, average electron temperature* $T_e \approx 0.22eV$ *at points of known density* n_i *(figure 5.8b).*

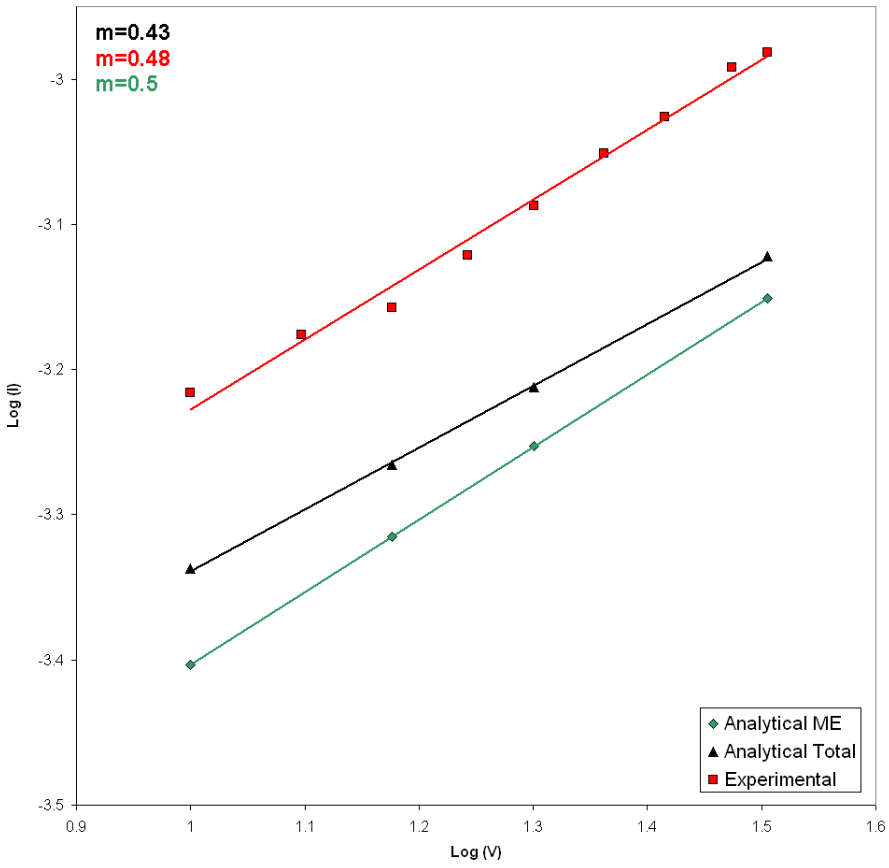

Figure 5.12: *Log-log plots showing the variation of the ion current with applied bias at peak current ($t = 5.92 \times 10^{-6} s$) for a probe in the parallel position. Results from experimental data (red) are compared against the results from the complete analytical model (black) and from the matrix extraction phase (green). The difference in magnitude between the experimental data and the model is caused by the models underestimation of the peak current as shown in the previous figures.*

5.3 Discussion

This chapter set out to compare the results of the analytical model against real experimental results to assess its performance. The first set of experimental results considered was carried out in University College Cork and involved a series of measurements for a Xenon plasma over range of densities, electron temperatures and flow velocities (mach 5-15). In each case the flow density was reported to be constant in time. It was shown that where the initial sheath width was less than the dimensions of the probe's surface good agreement between the analytical model and the experimental results was recorded. It was also noted that where the plasma's physical properties fell within the valid range of the model, behaviour close to the predicted $I \propto V^{0.5}$ was observed.

The second set of experimental results considered was that of a laser ablation plume with a highly supersonic flow (mach 38) and a time varying density carried out in Trinity College Dublin. While the model assumes a constant flow density it was shown that in this case it could be applied. The first justification is that for much of the plume the amount the density variation compared to the time taken to cross the probe was low. Secondly, the estimate of the density was best at the leading edge of the probe and the matrix extraction phase. Over this phase the most of the current is collected and therefore the impact of inaccuracies in density over the sheath expansion phase is minimized. The electron temperature is also known to vary in time but a lack of experimental data forced the assumption of an average value estimated from the parallel probe results.

The model was still found to be in reasonable agreement with the experimental results over a range of probe potentials. The range of greatest disagreement occurred over the peak current, matching the range over which

the electron temperature diverged most from the assumed value. It was found that an electron temperature approaching that estimated from the perpendicular results provided an improved agreement at peak current, leading to the assumption that the true electron temperature is somewhere between the two values measured at perpendicular and parallel orientations. Again, as with the results from UCC, the analytical models predicted a relationship between ion current and probe bias which was seen at the different potentials and flow densities.

CHAPTER 6

Conclusions and Future Work

6.1 Conclusions

This thesis has attempted to improve the application of planar Langmuir probes to unmagnetized collisionless plasma with supersonic flows. The physical conditions under which the presented model is valid and can be applied have been discussed.

It has been shown that when a planar probe's surface is oriented parallel or near parallel to the direction of flow in a plasma with a supersonic flow velocity it bears close resemblance to the conditions seen in plasma immersion ion implantation (PIII). The steps take to modify the model developed by Riemann and Daube [45] to describe the current density at the electrode during PIII to describe current density along the planar probe during the matrix extraction phase have been presented. The further extensions made

to account for the sheath expansion phase and the integration to allow the calculation of the total ion current collected by the probe have also been detailed.

Expressions for the total ion current collected by the probe were derived for the surface oriented parallel, as well as with small angles up and downstream of the direction of flow. In the case of the parallel expression it has been proposed that if the electron temperature and plasma density are known then the plasma's flow velocity could be inferred by fitting the model to the ion current over a range of negative probe bias. This is the only model of which the author is aware that addresses the lack of a satisfactory Mach probe theory for the measurement of the flow velocity in unmagnetized plasma with supersonic flow [54], though it must be conceded that it is limited in its applications.

As part of the development and testing of the analytical model a 2D hybrid particle in cell model was developed. The model was constructed with the probe embedded in the centre of the grid and separated from the boundaries on every side. The ability to inject plasma at various speeds and angles into the simulation was included to allow non-parallel orientations to be simulated. The code's structure and operation has been detailed along with the relevant conditions to ensure the stability of its numerical methods and the accuracy of its results.

The 2D code was then compared against 1D hybrid simulations to investigate how edge effects affected the behaviour of the plasma flow around the probe's leading edge at different velocities. As discussed, the edge effect proved great enough at lower flow velocities to warrant comparison against the analytical model to determine the 2D code performance.

It was found that for the parallel case the model's description of the

current density along the probe and the total ion current for highly supersonic flows agreed well, while at lower flow velocities the current density agreement was poor although the total ion current remained good. An explanation for the physical reasons behind this found that as the disturbance propagated further upstream of the probe's leading edge, the ions reacted earlier to the probe's potential. This led to the same ion flux striking the probe but with a different current density along its length.

The same comparison for the upstream and downstream conditions found that the total ion current was overestimated and underestimated, respectively by the model. The size of the disagreement even at 5° off parallel makes the use of the model under these conditions doubtful though further investigation might provide clues to corrections to increase its accuracy.

With the numerical simulations validating the success of the analytical model under parallel conditions, it was compared to experimental results. The first was a Xenon plasma for which I-V traces from the ion saturation region for a variety of densities, electron temperatures, flow velocities and applied bias were made available by Dr. McCarthy of University College Cork. In the course of the analysis it was found that where the dimensions of the probe exceeded the sheath width the model and the experimental results were in good agreement. Additionally, the predicted ion current's square root dependance on voltage was observed, over a range of conditions where the model is valid.

In the second case the plasma was a plume of silver created though ablation by a pulsed laser. For such a plasma the flow velocity is highly supersonic but the plasma density and electron temperature varies over time. The results from this experimental work were provided by Dr. Doggett of Trinity College Dublin. The density over the full time of the plume was estimated

from the experimental results of the ion current for the probe orientated perpendicular to the flow. Estimates of the electron temperature as measured for the probe perpendicular and parallel were also provided. Again the model's prediction of the ion current was found to be in good agreement with that recorded by the experiment, except where only poor estimates of the electron temperature were available. In addition, the predicted ion current's dependance on voltage was again observed.

In summary, we have presented an analytical model that gives a good estimation of the ion current collected by a negatively biased planar probe oriented parallel to the direction of flow of a plasma possessing a flow velocity in excess of the ion sound speed. In addition to a supersonic flow velocity the plasma is required to be collisionless, of a single species, singly charged and free from magnetic fields. Accurate estimations of the plasma electron temperature and density are required, both of which should be constant at least over the time taken to traverse the probe's length. The probe's dimensions must also exceed those of the initial sheath width but not be excessively long in comparison to the matrix extraction phase. Best agreement was found for the probe with its short axis parallel to the flow. The model offers the potential to determine the flow velocity of an unmagnetized plasma using a simple probe construction by fitting the predicted ion current to experimental results over a range of negative bias.

6.2 Future Work

The problem of using a planar Langmuir probe in unmagnetized flowing plasma remains. The work in this thesis has made a substantial contribution by developing a solution for the ion saturation range of the I-V trace.

Investigation to assess if the novel approach of orientating the probe parallel to the flow allows similar success in describing the current over the electron saturation and retardation ranges should be carried out. If successful this would provide a new diagnostic tool for the investigation of flowing plasma.

Related to the investigation of flowing plasma, this work also proposed a method where by the probe could be used to estimate the flow velocity of the plasma. In essence this would allowing it to function as a Mach probe provided good estimates of the density and electron temperature were available. The initial proof of concept work could be carried out with relative ease and developed further if it proved promising. The technical challenge of ensuring the probes accurate orientation to the flow would also need to be addressed.

The 2D hybrid PIC code developed as part of this thesis can be utilised to investigate several problems of interest. The first is the problem identified by Hutchinson [54] of characterising the potential drop on the downstream side of a planar probe orientated perpendicular to the direction of flow. With minimal effort the orientation of the probe within the grid could be rotated to allow it to simulate such a system. The results of this work could provide valuable insight for Mach probe theory and in the case of zero flow plasma immersion ion implantation (PIII).

The second concerns the further investigation of the probes interaction with laser ablation plasma. It has been stated earlier that the density of the ablation plume is not constant. While the analytical models excellent agreement supports the justifications used in its application the limits of accuracy have not been fully explored. The improvement of the field solver to handle a plasma flow with variable density would allow the models robustness over different rates of changing density to be evaluated.

Finally the interesting question of the true electron temperature in the laser ablation plume should be further investigated. It was seen in experimental results Doggett [70] that different values were measured depending on how the probe was oriented in relation to the flow. Despite of the fact that the hybrid code assumes the electron temperature as a *priori* rather than solving for it self-consistently, some useful investigation into the observed difference in temperature between the two probe orientations maybe possible.

APPENDIX A

List of Symbols

A	Area (m^2)
a	Acceleration (ms^{-1})
B	Magnetic Displacement Vector (T)
D_a	Ambipolar diffusion coefficient (m^2/s)
E	Electric field (Vm^{-1})
e	Absolute electron charge ($\simeq 1.6022 \times 10^{19}$ C)
F	Force (N)
I	Current (A); I_i Ion current
J	Current Density (Am^{-2})
k_B	Boltzmann's constant ($\simeq 1.381 \times 10^{-23}$ JK^{-1})
L	Length of probe (m)
m	Mass (kg); m_e electron mass ($\simeq 9.1 \times 10^{-31}$kg), m_i ion mass
n	n_0 Particle number density (m^{-3}); n_e electron density; n_i ion density
q	Electric charge (C)
T	Temperature (eV) or (K), T_e electron temperature

τ	time (s)
t	time (s)
s	sheath length (m), s_0 Matrix sheath, s_{cl} Child Law sheath
u	Velocity (ms^{-1}), u_f flow velocity, u_B Bohm velocity
Γ	Particle Flux
γ	Scaling parameter used in field solver
Δ	Δt time step (s), $\Delta x\,\Delta y$ cell size in x and y (m)
ϵ_0	Vacuum Permittivity ($\simeq 8.8 \times 10^{-12}\mathrm{Fm}^{-1}$)
η	Normalized density (section 3.4.2)
ϑ_m	Electron Neutral Collision Frequency
λ_D	Debye Length (m)
$\lambda_{m.f.p.}$	Mean free path
ρ	Charge density (Cm^{-3})
Φ	Potential (v)
π	Physical constant Pi 3.14159...
ψ	Normalized potential (section 3.4.2)
ω_p	Plasma Frequency(rad^{-1}), ω_{pi} ion frequency, ω_{pe} electron frequency
V	absolute potential (V)
V_0	applied potential (V)
W	Probe width (m)

APPENDIX B

Sheath Expansion

B.1 Sheath Expansion

In the same manner as Riemann [45] an expression for the sheath width along the length of the probe can be formulated, in non-normalised units with an arbitrary initial velocity towards the probe.

Starting from equation (2.48), it is integrated to get an expression for the sheath width at any point along the probe $s(\tau)$. Then substituting in equation (2.43) and using equation (2.37)

$$\frac{d}{d\tau}\frac{\partial\Phi(0,\tau)}{\partial x} = \left(\frac{\omega^2 m_i}{n_0 e}\right)\frac{s_0}{2}\frac{d\bar{n}}{d\tau} \tag{B.1}$$

$$= \frac{e}{\epsilon_0}\frac{s_0}{2}\frac{d\bar{n}}{d\tau}, \tag{B.2}$$

to get

$$\frac{ds}{d\tau} = u_0 - \frac{1}{n_0}\frac{d(\bar{n}s_1)}{d\tau} + \frac{1}{n_0}\frac{s_0}{2}\frac{d\bar{n}}{d\tau}, \tag{B.3}$$

$$s(\tau) = u_0\tau - \frac{\bar{n}}{n_0}s_1 + \frac{s_0}{2}\frac{\bar{n}}{n_0} + const, \tag{B.4}$$

and then utilizing the boundary conditions of $s(0) = s_1(0) = s_0$ to work out the constant of integration $const = 3s_0/2$ to give

$$s(\tau) = u_0\tau - \frac{\bar{n}}{n_0}s_1 + \frac{s_0}{2}\frac{\bar{n}}{n_0} + \frac{3s_0}{2}, \tag{B.5}$$

$$= u_0\tau + \frac{3s_0}{2} + \frac{s_0 - 2s_1(\tau)}{2 + (\omega\tau)^2}, \tag{B.6}$$

which, upon once again substituting length for τ gives

$$s(L) = \frac{u_0 L}{u_f} + \frac{3s_0}{2} + \frac{s_0 - 2s_1(L)}{2 + (\frac{\omega L}{u_f})^2}, \tag{B.7}$$

the width of the sheath along the length of the probe.

APPENDIX C

Conferences and Publications

C.1 Publications

Behaviour of a planar Langmuir probe in a laser ablation plasma.
B Doggett, C Budtz-Joergensen, J.G Lunney, P Sheerin and M.M Turner
Applied Surface Science, 247:134138, 2005

C.2 Conferences

Attended the International WE-Heraeus Summer School, Germany. (2004)

Presented Poster (*Particle Simulations of Super Sonic Plasma Expansion*).
IPBPG Conference in University College Cork, Ireland. (2004)

Presented Talk (*Investigating the characteristics of laser produced plasma using Langmuir probes*).

GEC Conference in Bunratty, Ireland. (2004)

Presented Poster (*Interpretation of Langmuir probe characteristics in unmagnetized flowing plasma*).

ICPIG Conference in Eindhoven, Netherlands. (2005)

Presented Poster (*Interpretation of Langmuir probe orientated parallel to the direction of flow in a laser ablation plasma*).

GEC Conference San Jose, California. (2005)

Submitted Poster.

IRCSET Meeting in Dublin, Ireland (2005)

Presented Poster.

IPBPG Conference in Dublin City University, Ireland (2006)

Presented Talk.

ICPIG Conference in Prague, Czech Republic. (2006)

Submitted Poster.

Bibliography

[1] Hudis M. Directional Langmuir probe *Journal of Applied Physics.* 1970;41:50115017.

[2] Roth J.Reece. *Industrial Plasma Engineering.* Bristol 1995.

[3] Goldston R.J. *Introduction to Plasma Physics.* Institure of Physics Pub. 1995.

[4] Lieberman M.A, Lichtenberg A.J. *Principles of Plasma Discharges and Material Processing.* Wiley 2005.

[5] Ruzic D.N. *Electrical Probes for Low Temperature Plasmas.* AVS Press 1994.

[6] Anisimov S.I, Bauerle D, Lukýanchuk B.S. Gas dynamics and film profiles in pulsed-laser deposition of materials *Physics Review B.* 1993;48:12076.

[7] Qi B, Gilgenbach R.M, Jones MC, Johnston MD, Lau YY. Diagnostic characterization of ablation plasma ion implantation *Journal of Applied Physics.* 2003;93:88768883.

[8] Toftmann B, Schou J, Hansen TN, Lunney JG. Angular distribution of electron temperature and density in a laser-ablation plume *Physics Review Letters.* 2000;84:39984001.

[9] Lindley R.A, Gilgenbach R.M, Ching C.H, Lash J.S, Doll G.L. Resonant holographic interferometry measurements of laser ablation plumes in vacuum, gas, and plasma environments *Journal of Applied Physics.* 1994;76:5457.

[10] Lunney J.G, Jordan R. Pulsed laser ablation of metals *Applied Surf. Sci..* 1998;129:941946.

[11] Toftmann B, Schou J, Hansen TN, Lunney JG. Evolution of the plasma parameters in the expanding laser ablation plume of silver *Applied Surf. Sci..* 2002;186:293297.

[12] Hansen T.N, Schou J, Lunney J.G. Langmuir probe study of plasma expansion in pulsed laser ablation *Applied Physics A.* 1999;69:S601-S604.

[13] Toftmann B, Schou J, Lunney JG. Dynamics of the plume produced by nanosecond ultraviolet laser ablation of metals *Physics Review B.* 2003;67:104101.1104101.5.

[14] Hendron J.M, , Mahony C.M.O, Morrow T, Graham W.G. Langmuir probe measurements of plasma parameters in the late stages of a laser ablated plume *Journal of Applied Physics.* 1997;81:21312134.

[15] Fähler S, Kerbs H.U. Calculations and experiments of material removal and kinetic energy during pulsed laser ablation of metals *Applied Surface Science.* 1996;9698:6165.

[16] Lunney J.G. Pulsed laser deposition of metal and metal multilayer films *Applied Surface Science.* 1995;86:7985.

[17] Qi B, Lau Y.Y, Gilgenbach R.M. Extraction of ions from the matrix sheath in ablation-plasma ion implantation *Applied Physics Letters.* 2001;78:706.

[18] Doggett B, Budtz-Joergensen C, Lunney J.G, Sheerin P, Turner M.M. Behaviour of a planar Langmuir probe in a laser ablation plasma *Applied Surface Science.* 2005;247:134138.

[19] Hughes T.P. *Plasma and Laser Light.* Adam Hilger 1975.

[20] Hansen T.N, Schou J, Lunney J.G. Angle-resolved energy distributions of laser ablated silver ions in vacuum *Applied Physics Letters.* 1998;72:18291831.

[21] Amoruso S, Bruzzese R, Spinelli N, Velotta R. TOPICAL REVIEW: Characterization of laser-ablation plasmas *Journal of Physics: B.* 1999;32:R131R172.

[22] Ellegaard O, Nedelea T, Schou J, Urbassek H.M. Plume expansion of a laser-induced plasma studied with particle-in-cell method *Applied Surface Science.* 2002;197:229238.

[23] Witke T, et.al . Deposition of hard amorphous carbon coatings by laser and arc methods *Surf. Coat. Technol..* 1999;116119:609613.

[24] Denavit J. Collisionless plasma expansion into a vacuum *Physics of Fluids.* 1979;22:13481382.

[25] Harilal S.S, Bindhu C.V, et.al . Plume splitting and sharpening in laser-pruduced aluminium plasma *J. Phys. D: Appl. Phys..* 2002;35:29352938.

[26] An C.W, Lu Y.F, Goh Y.W, Tan E. Observation of species distribution in laser induced plasma *Applied Surface Science.* 2000;154155:269275.

[27] Li P, Lim D, Mazumder J. Diagnostics of nanosecond dynamics of the plasma produced during KrF excimer laser ablation of zirconia in vacuum *Journal of Applied Physics.* 2002;92:666671.

[28] Martain G.W, Doyle L.A, et.al . Three-dimensional number density mapping in the plume of a low-temperature laser-ablation magnesium plasma *Applied Surface Science.* 1998;127129:710715.

[29] Kokai F, Koga Y. Time-of-fligh mas spectrometric studies on the plume dynamics of laser ablation of graphite *Nuclear Instruments and Methods in Physics Research B.* 1997;121:387391.

[30] Demidov V.I, Ratynskaia S.V, Rypdal K. Electric probes for plasmas: The link between theory and instrument *Review of Scientific Instruments.* 2002;73:34093439.

[31] Zhang Z, et.al . Muli-diagnostic comparison of femtosecond and nanosecond pulsed laser plasmas *Journal of Applied Physics.* 2002;92:28672874.

[32] Segall S.B, Kooper D.W. Application of cylindrical Langmuir probes to streaming plasma diagnostics *Physics of Fluids.* 1973;18:11491156.

[33] MacLatchy C.S. Charge depletion downstream of a cylindrical Langmuir probe immersed in a flowing, high-pressure plasma *IEEE Transactions on Plasma Science.* 1989;17:2933.

[34] Bergmann A. Two-dimensional particle simulation of Langmuir probe sheaths with oblique magnetic field *Physics of Plasma.* 1994;1:35983606.

[35] Hutchinson I.H. Ion collection by a sphere in a flowing plasma: I. Quasineutral *Plasma Physics and Controlled Fusion.* 2002;44:19531977.

[36] Booth J.P, Braithwaite N.StJ, et.al . *Frontiers in Low Temperature Plasma Diagnostics III Book of Papers*:117120 . 1999.

[37] Braithwaite N.StJ, Booth J.P, Cunge G. A novel electrostatic probe method for ion flux measurements *Plasma Sources Science Technology.* 1996;5:677684.

[38] Clements R.M, Smy P.R. The positively biased planar Langmuir probe in high-pressure plasma *Journal of Physics D Applied Physics.* 1993;26:19161920.

[39] Skøelv A, Armstrong R.J, Trulsen J. Ion beam diagnostics by means of plane Langmuir probes *Phys. Fluids.* 1984;11:2744.

[40] Lee S.G, Diebold D, Hershkowitz N, Intrator T, Wang X, Kim G. Direct measurement of plasma flow velocity using a Langmuir probe *Review of Scientific Instruments.* 1993;64:481.

[41] Sheridan T.E. How big is a small Langmuir probe? *Physics of Plasmas.* 2000;7:30843088.

[42] Lunney J.G, Lawler J.F, Aratari R. Ion emission studies of pulsed laser evaporation of $YBa_2Cu_3O_7$ *J. Applied Phys..* 1993;74:4277.

[43] Hutchinson I.H. *Principles of Plasma Diagnostics.* Cambridge Press2nd ed. 2002.

[44] Godyak V.A, Piejak R.B, Alexandrovich B.M. Probe diagnostics of non-Maxwellian plasmas *J. Apple. Phys..* 1993;73:3657.

[45] Riemann K.U, Daube T. Analytical model of the relaxation of a collionless ion matrix sheath *Journal of Applied Physics.* 1999;86:1202.

[46] Israel D, Riemann K.U, Tsendin L. Relaxation of a collisionless ion matrix sheath *Journal of Applied Physics.* 2004;95:45654574.

[47] Koopman D.W. Langmuir probe and microwave measurements of the properties of streaming plasmas generated by focused laser pulses *Phys. Fluids.* 1971;14:1707.

[48] Ohdachi S, Shoji T, et.al . Flow profiles measurements with a rotating Mach Probe in the scrape-off layer of the JFT-2M tokamak *Fusion engineering and Design.* 1997;3435:725728.

[49] Hong W.Y, Wang E.Y, et.al . The fluctionations and flow velocities measured with a Mach probe array on the HL-1M tokamak *Journal of Nuclear Materials.* 1997;241243:12341237.

[50] Ko E, Hershkowitz N. Asymmetry reversal of ion collection by Mach probes in flowing unmagnitized plasmas *Plasma Phys. Control. Fusion.* 2006;48:621634.

[51] MacLatchy C.S. Gundestrup: A Langmuir/Mach probe array for measuring flows in the scrape-off layer of TedV *Rev. Sci. Instrum..* 1992;63:39233929.

[52] Blac R, Bengtson R.D. A Langmuir/Mach probe array for edge plasma turbulence and flow *Rev. Sci. Instrum..* 1997;68:377380.

[53] Oksuz L, Hershkowitz N. Understanding Mach probes and Langmuir probes in a drifting, unmagnetized, non-uniform plasma *Plasma Sources Sci Technol..* 2004;13:263271.

[54] Hutchinson I.H. The invalidity of a Mach probe model *Phys. Plasmas.* 2002;9:18321836.

[55] Birdsall C.K, Langdon A.B. *Plasma Physics via Computer Simulaton.* IOP Publishing Ltd 1991.

[56] Hockney R.W, Eastwood J.W. *Computer Simulation Using Particles.* Adam Hilger 1988.

[57] Birdsall C.K. Particle-in-cell charged-particle simulations, plus Monte Carlo collisions with neutral atoms, PIC-MCC *IEEE Transactions on Plasma Science.* 1991;19:6585.

[58] Lawson W.S. Particle simulation of bounded 1D plasma systems *Journal of Computational Physics.* 1989;80:253.

[59] Verboncoeur J.P. Particle simulation of plasmas: review and advances *Plasma Physics and Controlled Fusion.* 2005;47:A231A261.

[60] Lieberman M.A. Model of plasma ion immersion ion implantation *Journal of Applied Physics.* 1989;66:29262929.

[61] Birdsall C.K, Bridges W.B. *Electron Dynamics of Diode Regions.* Academic New York 1966.

[62] Benilov M.S. Boundary conditions for the Child-Langmuir sheath model *IEEE Transactions on Plasma Science.* 2000;28:22072213.

[63] Riemann K.U, Tsendin L. Unipolar ion sheath *Journal of Applied Physics.* 2001;90:54875490.

[64] Meige A, Jarnyk M, et.al . Particel in cell simulation of an electron shock wave in a rapid rise time plasma immersion ion implantaion process *Physics of Plasmas.* 2005;12.

[65] Knuth D.E. *Seminumerical Algorithms.* Addison-Wesley Professional3rd ed. 1997. Specifically Section 3.6.

[66] Boyle P. *Modelling of Dual Frequency Capacitively Coupled Plasma Devices.* PhD thesisSchool of Physical SciencesDublin City University, Dublin 9, Ireland 2004.

[67] Ames W.F. *Numerical Methods for Partial Differential Equations 2nd Ed.* Academic Press 1977.

[68] Meige A. *Numerical Modeling of Low-Pressure Plasmas: Applications to Electric Double Layers.* PhD thesisCentre de Physique des Plasmas et de leurs Applictions de Toulouse (CPAT)Université Paul Sabatier, 118 route de Narbonne, Toulouse Cedex 31062, France 2006.

[69] O'Leary D. Experimental investigation of transport in a xenon plasma using Langmuir probes tech. rep.University College Cork 2006.

[70] Doggett B. *Characterisation of laser produced plasmas.* PhD thesisTrinity College Dublin 2006.